Universität Stuttgart

A Lanczos-filtered Harmonic Balance Method for Aeroelastic Applications of Turbomachinery Resolving Unsteady Turbulence Effects

Von der Fakultät Energie-, Verfahrens- und Biotechnik der Universität Stuttgart zur Erlangung der Würde eines Doktors der Ingenieurwissenschaften (Dr.-Ing.) genehmigte Abhandlung

vorgelegt von

Jan Philipp Heners

aus Achern

Hauptberichter:	Prof. Tekn. Dr. Damian Vogt
Mitberichter:	Prof. Dr.-Ing. Dieter Peitsch

Tag der mündlichen Prüfung: 04.07.2022

Institut für Thermische Strömungsmaschinen und Maschinenlaboratorium der Universität Stuttgart

2022

Declaration of Authorship

I declare that this research effort has been composed by myself and that the work has not been submitted for any other degree or professional qualification. I confirm that the work submitted is my own. The contribution of other authors to this work has been explicitly indicated below. I confirm that appropriate credit has been given within this thesis where reference has been made to the work of others.

The work presented in Sections 2.3, 2.4 and 5.1 was previously presented at the 15th International Symposium on Unsteady Aerodynamics, Aeroacoustics and Aeroelasticity of Turbomachines (ISUAAAT 15) and published in the ASME Journal of Turbomachinery as "*Investigation of the Impact of Unsteady Turbulence Effects on the Aeroelastic Analysis of a Low-Pressure Turbine Rotor Blade*" by **Jan Ph. Heners** (the author), **Prof. Dr. Damian Vogt** (1st supervisor), Dr. Christian Frey, and Dr. Graham Ashcroft. It has therefore been subject to the independent review process of the ASME Journal of Turbomachinery.

The work presented in Chapter 3 was previously published in the Proceedings of the ASME Turbo Expo 2020 as "*Prediction of the Unsteady Transition Behavior in Low Pressure Turbine Flows Using Time and Frequency Domain Methods*" by **Jan Ph. Heners** (the author), Dr. Christoph Müller-Schindewolffs, **Prof.**

Dr. Damian Vogt (1st supervisor), and Frederik Blum. It has therefore been subject to the independent review process of the ASME Turbo Expo.

The work presented in Chapter 4 was previously published in the Proceedings of the 14th European Conference on Turbomachinery Fluid Dynamics & Thermodynamics (ETC 14). In addition to that, an extended version of the conference paper was published in the International Journal of Turbomachinery, Propulsion and Power. Both were published under the title "*Prediction of Transient Pressure Fluctuations within a Low Pressure Turbine Cascade Using a Lanczos-Filtered Harmonic Balance Method*" by **Jan Ph. Heners** (the author), Dr. Stephan Stotz, Annette Krosse, Detlef Korte, Maximilian Beck, and **Prof. Dr. Damian Vogt** (1st supervisor) and have therefore been subject to the independent review process of the European Turbomachinery Society.

The work presented in Setions 6.3 and 6.4 was previously presented at the ASME Turbo Expo 2022 and published in the ASME Journal of Turbomachinery under the title "*Evaluating the Aerodynamic Damping at Shock Wave Boundary Layer Interacting Flow Conditions with Harmonic Balance*" by **Jan Ph. Heners** (the author), Dr. Christian Frey, and Dr. Björn Grüber. It has therefore been subject to the independent review process of the ASME Turbo Expo and the ASME Journal of Turbomachinery.

.....
Stuttgart, 2021-10-01

Abstract

This research thesis discusses the impact of unsteady turbulence effects on the numerical prediction of aerodynamic excitation mechanisms in turbomachinery flows. The limitations of existing solver structures based on a formulation in the frequency domain - the Harmonic Balance method, that is - promises to consider turbulence in an unsteady framework. Existing limitations to this are assessed and a solution approach to alleviate the identified sources of numerical instabilities is identified by the application of a Lanczos-type filter method.

After proper implementation and validation, the Harmonic Balance method enhanced by the filtering is used to evaluate the impact of unsteady turbulence on design tasks of aeroelastic interest. These are given by the prediction of the aerodynamic excitation and the aerodynamic damping, respectively. The impact of unsteady turbulence is investigated and quantified for both subsonic and transonic flow conditions. The evaluation of its quality and quantity is used to assess numerical solution approaches differing in the degree of exploited model order reduction. The assessed methods suffer from an increasing loss of information though benefit from lower requirements with regard to computational effort and run time.

Zusammenfassung

Die vorgelegte Promotionsschrift behandelt die Fragestellung des Einflusses instationärer Turbulenzeffekte auf die Vorhersage der aerodynamischen Anregung von Turbinen- und Verdichterkomponenten. Im Speziellen werden im Zuge der Arbeit zunächst die Ursachen für zu Beginn der Arbeit festgestellte Instabilitäten bei Anwendung des betrachteten numerischen Lösungsverfahren im Frequenzbereich identifiziert und durch Implementierung einer geeigneten Filtermethodik im Quellcode behoben.

Die Anwendung des stabilisierten Lösungsverfahrens in Verbindung mit einer entsprechenden Validierung erlaubt im Anschluss eine Bewertung des Einflusses der genannten instationären Turbulenzeffekte auf die in aeromechanischer Hinsicht relevanten Auslegungsaufgaben der Vorhersage von aerodynamischer Zwangserregung und Dämpfung. Dies wird sowohl für sub-, als auch für transsonische Strömungszustände untersucht und bewertet. Die Bewertung des Einflusses instationärer Turbulenzeffekte in Hinsicht auf Qualität und Quantität wird zur Analyse verschiedener numerischer Lösungsansätze verwendet, die aufgrund eines steigenden Grades von Modell-Ordnungs-Reduktion zunehmend unter Verlust an Information leiden, jedoch durch sinkende Anforderungen an die erforderliche Rechenleistung und Laufzeit profitieren.

Acknowledgements

This research thesis is a result of my work at MTU Aero Engines AG in Munich, Germany. During my research work in the Aerodynamics Department, I found considerable freedom to realise my ideas as well as an environment providing valuable insight in ongoing research and design issues concerning current and future generations of aircraft engines. Without the continuous support and exchange of the entire department, this research would never have achieved the presented level of industrial relevance and impact. Therefore, I would like to express my deepest gratitude to MTU Aero Engines AG and the Aerodynamics Department in particular for giving me the opportunity to realise this research effort.

I also want to express sincere thanks to my research advisor, Prof. Dr. tekn. Damian Vogt for guiding and supervising the presented work. At crucial stages of this research, he supported this effort by pointing out the achievements and, when necessary, hinting on an insufficient state of verification.

As the academic aspect of this work was assured by my supervisor Prof. Vogt from the University of Stuttgart, the same holds for Detlef Korte from MTU Aero Engines AG for what concerns the needs faced in an industrial context. The industrial value of this work as well as its contribution to the community of aeroelasticity in general is dedicated to him as to our continuous and detailed discussions.

A large part of the credit goes to the Numerical Methods Department of the Institute of Jet Propulsion at the German Aerospace Center DLR in Cologne. At DLR Cologne, I found a team that always supported me with their interest in my work, stimulating discussions and, if necessary, the expression of concerns about the progress of my research. In particular, I want to thank Dr. Christian Frey whose impact on this work can not be emphasised enough. Without his guidance, this work would have been lost. The same holds - maybe even without his further notice - for Dr. Jan Backhaus whose comments on this work at an early stage turned out to become a real game changer.

Furthermore, I want to thank a few people who supported this work in a way that must not be forgotten. First, I want to thank the students who accompanied me on my way to this thesis. These are Patrick Shoemaker from NUMECA Ingenieurbüro, Germany, Frederik Blum from Wieland Group, Germany, Nick Wildemans from TU Delft, The Netherlands, and Carlos Hünteler from TU München, Germany. The work and exchange with our students is and will be the main driver for our research.

Even more important than the students are, obviously, the teachers. The teachers who affected me and my research the most are Dr. Anne Gerdes from intersoft AG, Germany and Dr. Lars Radtke from TU Hamburg, Germany. Their patience, tuition and the way to share their knowledge expresses itself in the way I work, think and address problems to the present day.

Finally, every seized opportunity needs a person granting the required trust in the first place. Therefore, I want to close with my final thank to Dr. Karl Engel from MTU Aero Engines AG, Germany, for a lot but the most for giving me the possibility to proof my talent in a field of research I was allowed to enter without any experience.

Contents

Nomenclature

ATF	Altitude Test Facility
ATRD	Advanced Turbine Research Demonstrator
BPF	Blade Passing Frequency
CFD	Computational Fluid Dynamics
CPU	Central Processing Unit
CPUh	CPU hour
DC	Direct Current, Time-Invariant Component of a Fourier Series
DLR	German Aerospace Center
DFT	Discrete Fourier Transform
EO	Engine Order
FFT	Fast Fourier Transform
HB	Harmonic Balance
HPC	High Pressure Compressor
HS	Harmonic Set
IBPA	Inter Blade Phase Angle
iDFT	Inverse Discrete Fourier Transform
iFT	Inverse Fourier Transform
LPT	Low Pressure Turbine
LE	Leading Edge
MUSCL	Monotonic Upwind Scheme for Conservation Laws
ND	Nodal Diameter

NSV	Non-Synchronous Vibration	
PS	Pressure Side	
Q3D	Quasi Three-Dimensional Solution Approach	
RANS	Reynolds-averaged Navier Stokes Equations	
SS	Suction Side	
SWBLI	Shock Wave Boundary Layer Interaction	
TE	Trailing Edge	
TRACE	CFD Solver developed at DLR Cologne, Germany	
URANS	Unsteady Reynolds-averaged Navier Stokes Equations	
VPF	Vane Passing Frequency	
WG	Wake Generator	
WGPF	Wake Generator Passing Frequency	

c	Set of Primal Navier-Stokes Quantities	[-]
CFL	Courant-Friedrich-Lewy number	[-]
d	Set of Quantities required for Turbulence Modeling	[-]
δ	Boundary Layer Thickness	[m]
δ_1	Boundary Layer Displacement Thickness	[m]
$\Delta\eta_{\text{is,Stage2}}$	Deviation of Isentropic Efficiency	[%]
$\mathcal{D}$	Alternative Definition of a Differential Operator	[-]
E	Specific Total Energy of a Fluid	$[\frac{\text{m}^2}{\text{s}^2}]$
f	Fundamental or Base Frequency of a Flow Field	[Hz]
f_g	Specific, Local Generalised Force	$[\frac{\text{N}}{\text{m}^2}]$
F_g	Generalised Force	[N]
Φ	Turbomachinery Flow Coefficient	[-]
g_m	Skewness within a Measured Data Set	[-]
H_{12}	Boundary Layer Shape Factor	[-]
γ	Intermittency of a Transitional Boundary Layer	[-]
γ^*_δ	Intermittency averaged over the Boundary Layer	[-]
$\widehat{I}$	Equation System of the Discretised Flow Problem	[-]
k	Turbulence Kinetic Energy	$[\frac{\text{m}^2}{\text{s}^2}]$
l_U	Turbulence Length Scale	[m]
l_{ax}	Axial Chord Length	[m]
m	Harmonic Index of the HB Method	[-]

M	Truncation Order of the HB Method	[-]
Ma	Mach Number	[-]
$\mathrm{Ma}_{\mathrm{V2,in}}$	Mach Number at First Stator Exit Plane	[-]
μ	Dynamic Viscosity of a Fluid	[Pa·s]
μ_t	Eddy Viscosity of a Fluid	[Pa·s]
μ_2	Second Central Moment or Variance of Data Set	[V^2]
μ_3	Third Central Moment	[V^3]
N	Number of Sampling Points	[-]
p_t	Fluid Stagnation Pressure	[Pa]
q	Set of All considered URANS Quantities	[-]
ρ	Fluid Density	[$\frac{\mathrm{kg}}{\mathrm{m}^3}$]
ρE	Total Energy of a Fluid	[J]
ρu	Fluid Momentum	[N·s]
Π_tot	Overall Total Pressure Ratio	[-]
Ψ_t	Eddy Viscosity Ratio	[-]
$\widehat{R}$	Non-Linear URANS Residual in the Frequency Domain	[-]
R_N^*	Non-Linear URANS Residual at Sampling Point N	[-]
$\mathrm{Re}_{\mathrm{V2,in}}$	Reynolds number at the Second Stator Inlet Plane	[-]
Re_{Θ_t}	Transition Reynolds Number	[-]
Sr	Strouhal Number	[-]
σ	Standard Deviation of a Data Set	[V]
σ_m	Lanczos-σ Factor	[-]
t	Physical Time	[s]
T	Period of one Blade/Vane Passing	[s]
T_t	Total Temperature of a Fluid	[K]
T_U	Turbulence Intensity	[-]
Θ	Amplitude Modulation	[-]
τ	Pseudo Time	[-]
τ_w	Wall Shear Stress	[Pa]
θ	Boundary Layer Momentum Thickness	[m]
u	Fluid Velocity	[$\frac{\mathrm{m}}{\mathrm{s}}$]
ω	Turbulence Dissipation Rate	[s^{-1}]
Ω	Angular Frequency	[s^{-1}]
$\mathcal{O}_M$	Truncation Error of a Fourier Series Expansion	[-]
x	Axial Flow Direction	[m]

Chapter 1

Introduction

This research thesis discusses the prediction of aerodynamic excitation mechanisms in turbomachinery flows by numerical means. The results are of major interest in the context of an aeroelastic design process assessing the behaviour of turbomachinery components with regard to High Cycle Fatigue (HCF).

The demand to realise progressively more agressive blade designs and stage configurations of very tight axial distance enforce an increasing reliability of the aeroelastic evaluation during the design process of next generation aircraft engines. Since in the future, an increasing impact of sustainable energy sources suffering from unfavourable fluctuations in their generated power level is expected, new type industrial steam and gas turbines require in the same way enhanced aeroelastic methods to provide reliable alternatives balancing the supply of electrical power.

The predominant goal of this research is to improve the aeroelastic design process established in an industrial environment by improving the prediction accuracy of aerodynamic forces acting on assessed blade and vane structures. To accomplish this task, taking advantage of model order reduction beyond the existing linear approaches is identified as a promising alternative for future design projects in turbomachinery.

Even though aeromechanics is a multidisciplinary field involving structural

dynamics and aerodynamics, this research effort focuses exclusively on the aerodynamical part.

In the following, a brief introduction in the research field of aeroelasticity is given. Focusing on the aerodynamic component of aeroelasticity, this is followed by an overview of the state of the art in unsteady aerodynamics of turbomachinery flows. Since the extent of employed model order reduction is frequently discussed in this thesis, a brief recapitulation of model order reduction approaches established in this field of research is given as well. Furthermore, the research objectives of this thesis are introduced and the organisation of this dissertation is presented by giving an outline of the various chapters.

1.1. Aeroelasticity in Turbomachinery

To the present day, handling the vibration level in compressors, turbines and turbochargers remains a key challenge determining the commercial success of any turbomachinery design. The PW1100 GTF engine, for instance, one of the latest and most ambitious engine projects, faced severe vibration issues in the first two years after its entry into service [1].

In 2018, aircraft manufacturer *Airbus* decided to stop any orders of the PW1100 engine for its A320neo family due the vibration issues of the engine [2]. Though withdrawn later, the commercial consequences linked to the loss of trust at the customer side are impossible to estimate today. In the following, most A320neo customers choose the competing LEAP engine of manufacturer CFM-International amid the ongoing discussion about the engines long-term reliability.

According to [3], the sources of vibrations affecting components of turbomachinery can be classified in three main categories:

- **Forced Response**: excitation linked to multi-row interactions
- **Flutter**: self-excited vibration induced by an unstable state of aerodynamic equilibrium

- **Acoustic Resonance**: interaction between adjacent blades in phase to the interblade vibration angle

In practice, the first two vibration mechanisms of forced response and flutter are the most common concerns during the aeroelastic design of a turbomachinery [4].

The first aspect of forced response is characteristic for turbomachinery applications since it is based on the relative motion of adjacent stator and rotor rows. Operating an airfoil in turbomachinery leads inherently to time-dependent flow conditions since in general, an airfoil operates in the wake of an adjacent upstream row and in the potential field of adjacent up- and downstream rows.

Consequently, it faces time-varying flow conditions resulting in pressure distributions fluctuating periodically according to the rotational shaft speed. Potential candidates for critical levels of forced response excitation can often be anticipated in advance by relying on a Campbell-diagram [5].

If the the frequency of the present pressure fluctuations coincides with a structural eigenfrequency of the airfoil, even these small pressure perturbations can cause high vibration amplitudes. If the amplitudes become high enough, the structure can sustain this condition only for a very limited number of cycles. As a consequence, HCF-induced cracks appear and force a replacement of the airfoil or - even worse - result in a loss of the blade and a shut-down of the device.

The aeroelastic design quantities to determine critical forced response excitation are given by the aerodynamic excitation as well as the aerodynamic and structural damping. If the sum of the damping exceeds the present excitation, no problems with regard to HCF are expected. If the ratio between these quantities does not exceed a certain threshold, the airfoil is not considered to fail within the targeted maintenance interval.

Another crucial aeroelastic aspect covers self-induced excitations known as flutter. The presence of flutter instability is non-integral and might therefore become harder to determine in advance. In addition to that, flutter modes are

considered to be more critical due to rapidly ascending vibration amplitudes.

Flutter instability emphasises indefinitely small vibrations up to a structural failure of the airfoil due to an amplification of the associated blade forces. Even indefinitely small perturbations of the aerodynamic forces acting on the airfoil trigger a positive response on the perturbation itself. Therefore, the aerodynamic state of equilibrium is an unstable one which means that any change in the state of equilibrium is linked to a release of energy instead of a damping dissipation.

Accordingly, the quantity of interest to determine flutter stability is the present aerodynamic damping in the respective state of aerodynamic equilibrium. If the damping is positive, small perturbations are damped out before causing critical vibration levels and HCF failure. If the damping is negative, energy is released resulting in a self-induced excitation of the airfoil.

The third aspect of the listed aeroelastic key mechanisms is given by the acoustic resonance. Operating an airfoil in the potential field of adjacent blade rows induces acoustic pressure fluctuations that may induce not only forced response but also resonance driven excitation. Based on the cut-off ratio, acoustic pressure waves are either propagating, not-propagating or at the transition between both states [6, 7]. Depending on the propagation properties, acoustic resonances affect only a distinct set of interblade phase angles (IBPA).

If the acoustic pattern of a propagating wave matches the pattern of a travelling wave mode within an adjacent row, the resulting resonance might become critical. In addition to the above stated aeroelastic key quantities, the prediction of the acoustic propagation and the underlying cut-off ratio is of major importance here.

However, all the above stated excitation mechanisms are inherently unsteady. Accurate predicitions of the time-dependent flow behaviour are consequently of highest importance if a reliable level of aeroelastic stability is required during a design. Therefore, the challenges and recent progresses in the research field of unsteady aerodynamics in turbomachinery flows are recapitulated in the following.

1.2. Unsteady Aerodynamics in Turbomachinery

The growing demand in turbomachinery design to benefit from knowledge about the time-dependent flow behaviour leads to an increasing need for fast and efficient solution methods to resolve transient effects in turbomachinery flows. While the demands of aeroelasticity require an unsteady consideration of the flow field inevitably, for other design disciplines relying historically mainly on steady state methods progressively the question arises of how to take advantage of resolving unsteady effects. Promising to increase both the reliability and the quality of the pedicted stage efficiency, the impact of unsteady methods in future aerodynamic design tasks is expected to grow rapidly.

Since both aspects are highly dependent on the presence of turbulent driven flow structures, both can be achieved by taking advantage of an unsteady consideration of the underlying boundary layers. Providing reliable insight on boundary layer flows including their transition has, however, historically always been considered to be of crucial importance for the design of both compressors and low pressure turbines (LPT). The first and less sophisticated approaches to evaluate boundary layer separation were based on semi-empirical design rules as found for instance in [8, 9]. In order to judge the stability of compressor flows, other attempts rely on the relation between the in- and the outflow velocity [10].

While early numerical solution methods considering the impact of the boundary layer were based on combined calls of serial inviscid and boundary layer solvers [11], three-dimensional simulations solving the Reynolds-averaged Navier Stokes (RANS) opened up for taking into account complex flow phenomena such as transition in the design of turbomachinery components.

In both terms, the work presented in [12, 13, 14, 15] marks a milestone by a validation of multistage compressor and LPT simulations against time-resolved measurements of the boundary layer. As [16, 17] stressed the value of even more complex transition models, the application of a multimode model was proposed in [18]. This tranistion model proved to predict tran-

sition mechanisms in steady and unsteady time-domain simulations very accurately which could be confirmed by the research presented in [19]. However, given its limited application to structured grids caused by a dependency on parameters based on boundary-layer integration, the multimode model suffers from painful restrictions if applied to complex geometries, unstructured grids or frequency-domain methods.

At the same time, two equation transition models based on a local formulation of the intermittency γ and the transition Reynolds number Re_{Θ_t} [20, 21] promised to overcome these limitations. The proposed γ-Re_{Θ_t} transition model is not restricted to any limitations with regard to geometries or grid types. The general capabilty of the $\gamma - \mathrm{Re}_{\Theta_t}$ framework in both steady and unsteady RANS applications has been demonstrated in [22].

Additional interface formulations proposed by [23] allow to enhance the modeling of unsteady wake-induced transition mechanisms further improving the $\gamma - \mathrm{Re}_{\Theta_t}$ model for LPT applications. In combination with its prediction based on local model quantities alone, the $\gamma - \mathrm{Re}_{\Theta_t}$ model represents a more appealing way to resolve unsteady transition while relying on frequency-domain methods.

However, providing reliable knowledge about boundary layers and their transition mechanisms over a large range of the operating map remains to be one of the key challenges in the design of turbomachinery. The constraints faced in industrial applications such as the blade count, the mutual interaction of components rotating with non-synchronous shaft speeds or the presence of unexpected unsteady content require in general the simulation of large full-wheel configurations. Therefore, the majority of industrial design standards is to the present day limited to steady solution approaches. By increasingly adding unsteady measures to the well established existing steady processes, upcoming design concepts of turbomachinery are expected to benefit substantially from the enhanced insight provided by the unsteady consideration of the flow behaviour.

1.3. Model Order Reduction in Unsteady Aerodynamics

In addition to an optimal aerodynamic performance of the compressor and turbine components, delivering a design robust to high cycle fatigue is key in a succesful aircraft engine or any complex turbomachinery device. Due to the severe variation in the operating conditions of an aircraft engine, a reliable prediction of its fatigue behaviour requires the evaluation of an arbitrary high number of performance points though.

Furthermore, the evaluation of the aeroelastic key parameters given by aerodynamic damping and aerodynamic excitation requires an unsteady analysis of the flow field inevitably. As stressed already in the previous section, the consideration of unsteady effects in an industrial environment might result in the performance of full-wheel simulations meaning a tremendous numerical effort with regard to time, memory and processing units. Hence, providing reliable information about the aeroelastic behaviour over a vast range of the operating map may become arbitrarily expensive. Recalling these ambivalent constraints, relying on models of reduced order becomes inevitable in an aeroelastic design framework.

The first and most reduced approaches use empirical calibration based on experience from previous designs and overall flow characteristic such as Strouhal number Sr, Reynolds number Re and Mach number Ma. However, benefiting from the exponential growth of available computing power, the impact of numerical simulations rose over the past decades and provided over the time analysis methods of a continuously lowering degree of model order reduction. For instance, [24] and [25] proposed first numerical approaches for the unsteady evaluation of two-dimensional flows in lightly loaded subsonic cascades based on the strip-theory of flat plate models.

In the following, various methods such as the ones proposed by [26] and [27] enabled numerical methods of higher complexity, in particular for what concerns the underlying geometry and the transonic character of the flow field, by taking advantage of a linearised consideration of the flow as a potential field. Though still limited by the assumption of a two-dimensional, inviscid flow described in terms of a system of inertia, these

approaches interpreted the temporal unsteadiness within the flow by means of a linearisation around a reliable solution of the steady flow state. Given the wide-ranging impact of linearised steady-state methods in industrial applications to the present day, this might suggest aeroelasticity has not come far in the past 40 years.

In the following years, the above mentioned limitations of the linearised approaches were alleviated step by step by expanding the theory to linearised solutions of first the Euler-equations [28, 29, 30, 31] and subsequently to the Navier-Stokes equations [32] while finally extending the theory to three-dimensional flows as shown for instance by [32, 33].

As the access to large amounts of computational power became affordable and mainstream in the following, the demand for a non-linear consideration of the unsteady effects driving the aerodynamic excitation increased substantially. The pursued approaches can be separated into two paths accepting differing degrees of resulting model order reduction.

The approach promising to deliver the best results by benefiting from the least degree of model assumptions consists in performing non-linear time-integration simulations relying on an appropriate time-stepping to resolve all unsteady content of interest. First proposed for the application to two-dimensional Euler-methods by [34, 35, 36], the application of non-linear time-integration methods was extended rapidly to three-dimensional Navier-Stokes simulations of multi-row configurations of both subsonic and transonic flows as sketched in the previous section 1.2. Focusing on the demands of aeroelasticity, a review over the progress made in the past two decades by the application of non-linear time-integration methods is given recently by [37]. However, the drawbacks of these costly approaches remain which makes the exploitation of proper model order reduction techniques in the context of non-linear aeroelastic applications still an attractive alternative to the expensive time-stepping methods.

Hence, a second approach focusing the consumed numerical efforts on an explicit choice of unsteady interaction within the flow field was carried out - driven by the demands of aeroelastic and aeroacoustic applications in particular. Since in aeroelasticity the focus is in general exclusively on

the evaluation of the unsteady content emerging at an eigenfrequency of the structure that is already known in advance, generating unsteady information by resolving a continuous bandwidth - as done by relying on a time-integration approach - appears to be inefficient.

Thus, exploiting the highly harmonic character of the unsteadiness in a turbomachinery flow by referring to frequency domain methods as the non-linear-harmonic (NLH) or the Harmonic Balance (HB) method as proposed first by [38, 39, 40, 41] provides an attractive choice to face the requirements concerning both performance and efficiency to predict unsteady phenomena in an industrial design process.

The first NLH approaches applied to turbomachinery flows were proposed by [38] where the flow state is solved for a distinct source of harmonic unsteadiness in combination with its temporal average instead of an expansion or linearisation around its steady state. The coupling of the resolved components is realised via the non-linear stress-terms and allows therefore to take non-linear effects into account. The approach can in general be extended to the governing equations used in the context of one- and two-equation models as often applied in turbulence modeling as well as to a consideration of the mutual coupling of all resolved harmonic content [42].

However, taking advantage of hybrid frequency-time domain methods has proven to provide an efficient alternative if the non-linear coupling terms limit the efficiency of the NLH-method. Based on an evaluation of the non-linear components at discrete sampling points in time and performing mutual Fourier transforms and their inverses, respectively, the Harmonic Balance method as proposed by [39, 40] allows to consider time periodic perturbations in a reliable and economical fashion.

Since the numerical effort increases obviously with the number of sampling points referred to in the time domain, various publications propose an approach based on the superposition of defined sets of differing base frequencies and associated harmonics. While the majority of the proposed approaches [43, 44, 45, 46, 47] rely on an inverse Fourier transform of both the non-linear and the time-linear component - the latter being linked to the temporal derivative of the parabolic flow problem - the HB method discussed

in this work focuses exclusively on a transformation of the non-linear flow residual [41]. As both accuracy and efficiency of frequency domain methods are demonstrated in general by [48], the benefit of a HB method relying on the Harmonic Set (HS) approach with regard to multistage turbomachinery applications is shown in [41, 49, 50, 51, 52, 53, 54, 55].

Despite the promising progress, the proposed HB approaches still suffer from individual limitations, some related to the enforced model order reduction, others caused by the respective approach of implementation. In general, all frequency domain approaches assume the unsteadiness of the evaluated flow field to be of harmonic character by solving for frequencies that have to be known in advance. Though the first assumption of periodic unsteadiness can be justified without any loss of generality for aeroelastic applications, the latter might prove to be a limiting drawback at distinct flow states if unknown, non-synchronous frequency content is interfering with the analysis frequency in a non-neglectable fashion.

Furthermore, the efficiency of HB approaches is in general prone to flows where the interaction of harmonic content of either high multiples or even non-integer multiples of a shared beat frequency has to be taken into account. This kind of flow situation occurs, for instance, if two-shaft configurations of differing rotational shaft speeds are considered or the excitation at low engine orders is of interest. While the first problem of unknown frequency content is linked to the model order reduction approach in general, the second problem can be overcome by an according structure of the underlying solution process and relying on almost periodic Fourier transforms [44, 56] or taking advantage of multidimensional Fourier transforms as proposed recently by [57].

Further limitations might consist in neglecting the mutual back-to-back coupling of the captured harmonics during the solution process which is rather a question of investing the numerical effort as this issue has already been discussed in early publications such as [42]. However, for what concerns the capability of the discussed HB method, its asset towards the demands faced in an aeroelastic context is emphasised by various publications, see for instance [58, 59, 60, 61, 62, 63, 64].

Finally, a key aspect adressed the scope of this work is the limitation of the investigated HB approach if turbulence as well as its transition is considered in an unsteady fashion. If the transport equations employed by the one- and two-equation turbulence models usually used in industrial applications are solved in an unsteady fashion, resulting instabilities tend to affect the numerical solution behaviour in an unfavourable fashion in lots of applications. Therefore, previous studies based on the HB approach often neglect the unsteady turbulence behaviour by relying on a so-called frozen eddy viscosity approach [65].

Amidst the uncertainty with regard to the robustness of the employed turbulence model as well as the reliability of the obtained results for flows where turbulence is expected to have a major impact on the aerodynamic cost quantity, the stability problems faced by engineers prevent HB to become a standard evaluation method in an industrial environment. Accordingly, literature estimating the impact of turbulence and even demonstrating the general capability to reproduce unsteady turbulence effects by relying on a frequency domain based solution process is rare [55, 63, 66, 67].

Regarding the prediction of unsteady boundary layer transition by means of a frequency domain solver, a detailed assessment is given by [66, 67]. In these works, time-resolved measurement data acquired by fast-response static pressure transducers are used to identify the underlying transition modes. In addition, the problems induced by the Gibbs phenomenon if the transport equations linked to turbulence and transition modeling are solved in an unsteady framework are stressed in [67].

The presented work aims at closing this gap by a detailed discussion of the numerical problems causing the observed lack of reliability if turbulence effects are considered in an unsteady fashion. Furthermore, this research effort provides an estimate of its impact on a various number of flow states being representative for common aeroelastic design tasks as faced in an industrial environment.

1.4. Research Objectives

In this work, a state-of-the-art HB solver based on the formulation of [41] is extended to robustly account for the impact of unsteady turbulence. Since the HB method is identified to suffer from numerical instabilities if turbulence is considered in an unsteady fashion, the first step of this work consists in an investigation of these numerical instabilities. Based on the identified error sources, appropriate measures to increase the computational robustness are formulated. The application of a filter method employed during the inverse Fourier transform proves to deliver a promising increase of the robustness of the solver.

The identified filter method is thoroughly implemented in the source code of the applied CFD solver. Once an increased level of robustness is available, the enhanced HB method is validated against time resolved measurement data. The validation is performed in two steps, where the first one evaluates the capability of the HB method to reproduce the unsteady transition of the boundary layer. The second validation step focuses on the prediction of unsteady pressure fluctuations acting on an excited stator vane.

By following a model order reduction approach of the unsteady flow problem, which is the basic idea of any frequency domain solution method, naturally the question arises which unsteady effects are worth being resolved and which can be neglected. Accordingly, this work aims at assessing to what extent results of aeroelastic relevance are affected by an unsteady consideration of turbulence. Therefore, the Lanczos-filtered HB approach is used to predict the aerodynamic excitation and the aerodynamic damping, respectively. Results of differing degrees of resolved unsteadiness are compared. The impact of unsteady turbulence effects on aeroelastic key quantities is discussed and evaluated for both subsonic and transonic flow situations.

The required numerical effort of the assessed solution methods is compared and discussed in relation to the quality of the associated results. Depending on the respective excitation mechanisms of forced response and flutter, the benefit of resolving turbulence effects in an unsteady fashion is discussed

by a comparison to cheaper and less prone approaches being limited to a time-averaged or even frozen-at-steady-state consideration of turbulence.

The thesis is outlined as follows: In chapter 2, the investigated flow solver TRACE is introduced briefly and the theory of the pursued Harmonic Balance approach is presented. The inevitable impact resulting from Gibbs phenomenon is identified as a potential source of numerical instabilities for the applied Harmonic Balance method and the theory of an appropriate counter measure given by the application of a Lanczos-type filter method is discussed.

In chapter 3, the application of the proposed filter method on the model quantities of turbulence is validated against time resolved measurement data of a transitional boundary layer within a two-stage low pressure turbine test facility. The capability of the enhanced HB method to predict the unsteady transition behaviour is discussed by a comparison against the available measurement data and the results provided by a full wheel time-integration solver.

In order to ensure the quality of the modified solution algorithm for aeroelastic applications, the capability of the filtered HB solution method to predict surface pressure fluctuations is assessed in chapter 4 by taking advantage of proper unsteady measurement data recorded at the surface of a stator cascade. Again, the results are benchmarked by a comparison to results generated by an established time-integration solver.

Finally, the Harmonic Balance method modified by the proposed filter approach is used to predict the aerodynamic excitation of modern LPT and compressor configurations in chapter 5. While its application on subsonic flow conditions is discussed for an investigated LPT setup, the behaviour for what concerns transonic flow states is covered by the discussion of a compressor flow. For both applications, the presented results are benchmarked by taking into account equivalent results based on an expensive time-integration method.

The results stated with regard to the aerodynamic excitation are extended to the prediction of the aerodynamic damping in chapter 6. Both subsonic and transonic flow conditions are discussed by the evaluation of differing

throttle conditions of a last stage compressor row. The benefit of the proposed HB method if compared to a linearisation around the steady state flow field is assessed, as well as the differences to a HB approach limited to a time-averaged consideration of turbulence are quantified.

The results of this work are summarised in chapter 7. Based on the results of the presented research, the impact of unsteady turbulence on the aeroelastic design of turbomachinery components is estimated and the benefit of its consideration in an industrial environment is discussed in relation to the additional numerical effort. Finally, the thesis closes with an overview of problems that require further investigation.

Chapter 2

Applied Numerical Methods

In the context of this work, the fluid is treated as an ideal gas of Newtonian character. The flow field is determined by the solution of the compressible unsteady Reynolds-averaged Navier-Stokes (URANS) equations (A.10)-(A.12) yielding a physical state described completely by the fluid density ρ, the fluid momentum ρu and the total energy ρE. The impact of turbulence is considered in accordance with the Wilcox $k-\omega$ two-equation turbulence model [68]. If the transition of the underlying boundary layers from a laminar to a turbulent state is expected to play a substantial role, a proper transition model depending on the respective application is taken into account. The transition models of the respective cases are based either on the solution of additional transport equations in terms of Menter's $\gamma - \mathrm{Re}_{\Theta_t}$ framework [20, 21] or on a strategy related on calibrated correlations [18].

In the following, a brief overview of the employed numerical methods is given. This includes a brief specification of the underlying solver structures, a general description of the Harmonic Balance method referred to in this work and a detailed discussion of the theory of the realised Lanczos-Filter approach.

2.1. Flow Solver TRACE

The unsteady flow solvers applied in the context of this work are part of the CFD code framework TRACE developed at the Institute of Propulsion Technology at the German Aerospace Center DLR in Cologne. TRACE is a hybrid solver for the finite-volume discretisation of the compressible URANS equations on both structured and unstructured grids in the relative frame of reference [69]. It enables a non-linear and unsteady analysis in both time [66, 69, 70, 71] and frequency domain [41, 53, 60, 63, 64, 67, 65] of three-dimensional turbomachinery flows in a parallel fashion taking advantage of hybrid distributed-/shared-memory structures. Inviscid fluxes are evaluated based on second-order accurate Roe upwind spatial discretisation. The upwind states are considered by relating to monotonic upwind schemes for conservation laws (MUSCL) [72]. In order to avoid unphysical oscillations in the presence of shocks, a modified van Albada limiter [73] is applied. The discretisation of viscous flow components is realised via second-order accurate central difference schemes. The impact of turbulence can be considered by a various number of turbulence and transition models integrated in the code [74]. For all unsteady simulations, equivalent boundary conditions are imposed. The boundary conditions are of non-reflecting type as proposed by [75] and based on a formulation in the frequency domain as described in [76, 77].

2.2. The Harmonic Balance Method

In general, the basic idea while taking advantage of a frequency domain approach is to exploit the highly harmonic character of the unsteadiness in a turbomachinery flow by assuming all transient effects to be periodic in time. Obvious choices of dominant harmonic content are frequencies linked to the present vane and blade passing frequencies, respectively. However, harmonic content being non-synchronous to the associated rotational shaft speed - for instance due to a mutual interaction of shock and boundary layer systems - might also be of major relevance from an industrial point of view.

Following the assumption of temporal periodicity, the semi-discrete form of the URANS equations can be stated in the following form

$$\frac{\partial q}{\partial t} + R(q(t)) \;=\; 0 \quad , \tag{2.1}$$

where q denotes the vector of quantities to be solved during the solution process represented by the set of conservative flow variables $c(x,t)$ and variables required in the context of turbulence modeling $d(x,t)$. Furthermore, t denotes the physical time and R the non-parabolic residual of the URANS equations containing all components linked to convection, diffusion and production terms. If the unsteadiness within the flow field appears to be periodic in time at the base frequency $f = \Omega/(2\pi)$, $q(t)$ can be reformulated via a Fourier series by

$$q(x,t) \;=\; \mathrm{Re}\left[\sum_{m=-\infty}^{\infty} \widehat{q}_m(x)\, e^{\mathrm{i}m\Omega t} \right] \quad . \tag{2.2}$$

In the very same way, the non-parabolic - and therefore non-linear - RANS residual $R(q)$ can be formulated as a Fourier series yielding

$$R(q(x,t)) \;=\; \mathrm{Re}\left[\sum_{m=-\infty}^{\infty} \widehat{R}_m(x)\, e^{\mathrm{i}m\Omega t} \right] \quad . \tag{2.3}$$

If the temporal periodicity within the flow field can be described sufficiently by a limited number of harmonics M, it is attractive to reduce $q(x,t)$ and $R(q)$ to a truncated Fourier series and reformulate the complete URANS system (2.1) in the frequency domain as

$$\sum_{m=-M}^{M} \left[\mathrm{i}m\Omega\, \widehat{q}_m(x) + \widehat{R}(q)_m(x) \right] e^{\mathrm{i}m\Omega t} \;=\; 0 \tag{2.4}$$

by focusing on a distinct set of harmonics $m = \{-M, ..., 0, \ldots, M\}$. Since the basis functions $e^{\mathrm{i}m\Omega t}$ are linearly independent, each summand of the

respective harmonics m in eq. (2.4) needs to satisfy the condition

$$\widehat{I}_m \;=\; \mathrm{i}m\Omega\, \widehat{q}_m(x) + \widehat{R}(q)_m(x) \;=\; 0 \tag{2.5}$$

by itself. However, since the residual $R(q)$ of the URANS equations includes all non-linear components of the PDE-system, it suffers in general from non-linear dependencies of the solved variables $q(x,t)$ on the physical state. Thus, the solution of the m-th component of eq. (2.5) requires information being non-linear dependent on all M considered harmonics in q. Accordingly, one of the key challenges while pursuing a non-linear frequency domain approach consists in providing the non-parabolic components of $\widehat{R}(q)_m$ in an efficient manner during the entire solution process.

In the HB method investigated in this research, this is realised by relying on a hybrid frequency-time-domain approach according to Fig. 2.1 as proposed for instance by [40, 41]. Based on the information of $\widehat{q}_m$ for all $m = \{-M, ..., 0, \ldots, M\}$ from a previous iteration step, the flow state is reconstructed in the time domain to a predefined set of N sampling points by application of an inverse discrete Fourier transform (iDFT)

$$q^*(x,t) \;=\; \mathcal{F}^{-1}\{\widehat{q}_m(x)\} \quad , \tag{2.6}$$

where q^* denotes the approximation of the flow field at each of the N sampling points obtained from iDFT. In a subsequent step, the non-linear residual

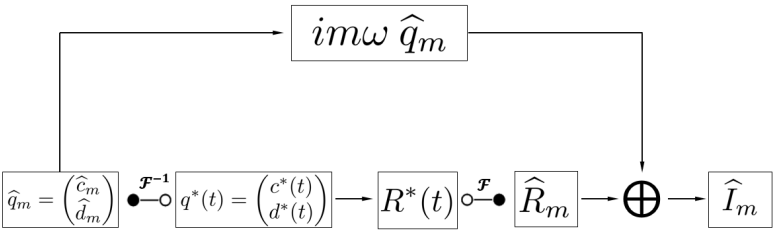

Figure 2.1.: HYBRID FREQUENCY-TIME DOMAIN APPROACH FOR THE ASSEMBLY OF THE PSEUDO-TIME RESIDUAL I_m [40, 53].

R^* is then computed at each of the N sampling points by exploiting the information of the reconstructed flow solution q^*. Since the calculation of R^* is exclusively carried out in the time-domain, standard flux and discretisation schemes available from existing non-linear solver schemes in TRACE can be accessed. The information about the non-linear residual $\widehat{R}(\widehat{q}))_m$ - which is required in the frequency domain - can then be obtained by performing a discrete Fourier transform (DFT) over the residual components R^* available at each of the N sampling points.

$$\widehat{R}(\widehat{q})_m \;=\; \mathcal{F}\big\{R^*(q^*(x,t)\big\} \tag{2.7}$$

According to Fig. 2.1, the equation system $\widehat{I}_m$ is assembled by adding the parabolic contributions linked to the temporal derivative $\partial\widehat{q}_m/\partial t$ by relying on its spectral representation $(im\Omega)\,\widehat{q}_m$ at each harmonic m. The components of $\widehat{I}_m$ in eq. (2.5) may be interpreted as a residual in the sense of a pseudo-time marching solution algorithm. By introducing the associated pseudo-time derivative via

$$\frac{\partial\widehat{q}_m}{\partial\tau}+\widehat{I}_m \;=\; 0 \tag{2.8}$$

the solution to eq. (2.5) can be found by driving eq. (2.8) to a convergent steady-state by relying on common implicit pseudo-time marching algorithms.

2.3. Instabilities due to Gibbs Phenomenon

The basic idea behind the application of a frequency domain based solution algorithm as the HB method is to take advantage of model order reduction by focusing on a limited number of frequencies and associated harmonics. Accordingly, the reconstruction from frequency to time domain required during the solution process displayed in Fig. 2.1 suffers always to a certain extent from the well known Gibbs phenomenon [78]. Variables solved in the context of turbulence modeling such as turbulence kinetic energy k and

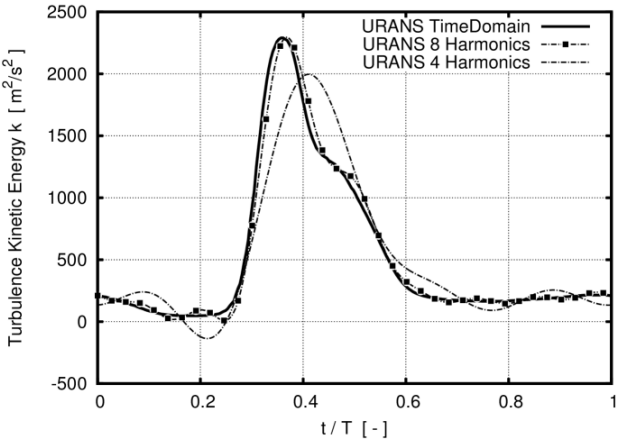

Figure 2.2.: WAKE OF TURBULENCE KINETIC ENERGY k DOWNSTREAM OF A LPT STATOR VANE AND ITS FOURIER DECOMPOSITION [63].

dissipation rate ω are affected by this in the most critical order since the ringing associated to the Gibbs phenomenon causes undershoots in both k and ω potentially leading to negative values in these quantities. This is highlighted by Fig. 2.2 where the turbulence kinetic energy k downstream of a LPT stator vane is plotted over one blade passing period T [63].

The solid line in Fig. 2.2 represents the wake predicted by a URANS-simulation based on a time-marching algorithm performed exclusively in the time domain. Fourier transform and reconstruction of this wake signal by a limited number of harmonics represent the remaining lines in Fig. 2.2. Approximating the wake by focusing on 4 and 8 harmonics only results in the curves displayed by a dash-dotted and a dash-dotted line with solid squares, respectively. The negative impact of ringing becomes obvious by the approximation based on 4 harmonics, in particular in the appearance of the wake at $t/T \sim 0.2$.

The undershoots induced by the Gibbs phenomenon in the presence of high gradients, as for instance close to the increase of turbulence kinetic

energy linked to the passing wake, result in an approximation of k with negative values. The capability to predict the wake's peak and width can be improved by taking into account 8 harmonics as displayed by the dash-dotted line with solid squares. The unfavourable impact of ringing is reduced significantly though still predicting the level of turbulence to appear close to the limits of the valid range of values.

Negative values for both turbulence kinetic energy k and dissipation rate ω are not feasible, neither from a physical nor from a numerical point of view. Hence, a limiter avoiding negative values by prescribing positive values close to zero is applied during the solution process. However, by arguing in terms of the hybrid frequency-time-domain approach as proposed in Fig. 2.1, referring to this limiter induces a significant level of noise being inconsistent to the reference state in the frequency domain. Furthermore, the routines responsible for the treatment of the non-linear components R^* in the time domain behave very sensitive if forced to operate close to the limits of the feasible range of values. Both aspects affect the behaviour of the underlying numerical algorithms in an unphysical fashion and decrease their stability in an unfavourable order. Thus, the unsteadiness in the applied turbulence and transition models are often neglected in previous HB studies by exploiting an approach based on an eddy viscosity that is frozen to its steady state [65].

2.4. The Lanczos-Filter Method

The unfavourable impact of ringing in the presence of high gradients or discontinuities can be alleviated by the application of Lanczos-type filters [79, 80, 81, 82]. While in the work of [81] a similar method is employed for the parabolic components of the flow quantities, this research focuses on a filter application during the calculation of the non-parabolic residual contributions $\widehat{R}$. Due to the stark contrast between low turbulence at freestream conditions and very high levels of turbulence in appearance of the wake, the negative impact induced by the Gibbs phenomenon affects the solution behaviour of the transport equations linked to turbulence in the most critical fashion.

Hence, the application of the proposed filtering method is constrained to the set of turbulence quantities $d = (k, \omega, \gamma, \mathrm{Re}_{\Theta t})$.

The truncation term $\mathcal{O}_M(\Omega t)$ representing the approximation error of a Fourier series truncated at order M is in general defined by

$$\begin{aligned} d_M(\Omega t) &= \underbrace{\sum_{m=-M}^{M} \widehat{d}_m \cdot e^{\mathrm{i}m\Omega t}}_{\widehat{d}_M(\Omega t)} + \underbrace{\sum_{m=M+1}^{\infty} \widehat{d}_m \cdot e^{\mathrm{i}m\Omega t} + \widehat{d}_{-m} \cdot e^{-\mathrm{i}m\Omega t}}_{\mathcal{O}_M(\Omega t)} \\ &= \widehat{d}_M(\Omega t) + \mathcal{O}_M(\Omega t) \quad . \end{aligned} \tag{2.9}$$

In the perspective of signal analysis, the respective components of the truncation error $\mathcal{O}_M(\Omega t)$ defined in eq. (2.9) can be interpreted as high-frequent carrier waves modulated in their amplitude. Both the modulation of the amplitude $\Theta(\Omega t)$ and its associated carrier signal can be isolated by shifting the indices of the truncation error components in eq. (2.9)

$$\begin{aligned} \mathcal{O}_M(\Omega t) &= \left(\sum_{m=0}^{\infty} \widehat{d}_{m+(M+1)} \cdot e^{\mathrm{i}m\Omega t} \right) \cdot e^{\mathrm{i}(M+1)\Omega t} \\ &\quad + \left(\sum_{m=0}^{\infty} \widehat{d}_{-(m+(M+1))} \cdot e^{-\mathrm{i}m\Omega t} \right) \cdot e^{-\mathrm{i}(M+1)\Omega t} \\ &= \Theta_{M}(\Omega t) \cdot e^{\mathrm{i}(M+1)\Omega t} + \Theta_{-M}(\Omega t) \cdot e^{-\mathrm{i}(M+1)\Omega t} \quad . \end{aligned} \tag{2.10}$$

The interpretation of the truncation error as a modulated carrier wave in eq. (2.10) indicates the oscillation of the truncation error $\mathcal{O}_M(\Omega t)$ at its truncation frequency $(M+1) \cdot \Omega$ only.

Analysis of the T-normalised temporal derivative of the truncation error $\mathcal{O}_M(\Omega t)$

$$\frac{\partial \mathcal{O}_M(\Omega t)}{\partial(\Omega t)} = \mathrm{i}(M+1)\cdot\Theta_{M}(\Omega t)\cdot e^{\mathrm{i}(M+1)\Omega t} + \frac{\partial \Theta_{M}(\Omega t)}{\partial(\Omega t)}\cdot e^{\mathrm{i}(M+1)\Omega t} - \mathrm{i}(M+1)\cdot\Theta_{-M}(\Omega t)\cdot e^{-\mathrm{i}(M+1)\Omega t} + \frac{\partial \Theta_{-M}(\Omega t)}{\partial(\Omega t)}\cdot e^{-\mathrm{i}(M+1)\Omega t} \tag{2.11}$$

shows an amplification of its derivative by the truncation order $(M+1)$. Recalling that the number of considered harmonics M is in practice a high integer value, the amplification stated by eq. (2.11) induces a disproportional forcing compared to the truncation error itself.

The disproportional amplification of the truncation error derivative reveals the very nature of Gibbs phenomenon. In the presence of high gradients, as faced for instance during the transition from freestream to wake conditions, both truncated Fourier series $d_M(\Omega t)$ and truncation error $\mathcal{O}_M(\Omega t)$ are facing high gradients as well. According to eq. (2.11), the high gradient of the truncation error in regions of discontinuities or wake transition is then even more amplified. Since high values of the gradient are equivalent to large changes of the quantity itself, the amplification of the truncation error derivative leads to rapid changes in the truncation error.

By definition of eq. (2.9), the truncation error $\mathcal{O}_M(\Omega t)$ is the deviation of the truncated Fourier series $\widehat{d}_M(\Omega t)$ from the quantity to be approximated $d_M(\Omega t)$. Thus, discontinuities or high gradients in $d_M(\Omega t)$ cause locally rapid changes in the deviation of the truncated Fourier series approximation $\widehat{d}_M(\Omega t)$ from the quantity to be approximated $d_M(\Omega t)$, which is the basic appearance of Gibbs phenomenon.

Hence, in order to alleviate the ringing caused by the Gibbs phenomenon, it is mandatory to avoid the amplification of the truncation error derivative. The negative impact of the carrier signal derivative can be alleviated by the

introduction of an alternative differential operator $\mathcal{D}_M$ defined as

$$\mathcal{D}_M\, d(\Omega t) \;:=\; \frac{d\left(\Omega t + \frac{\pi}{M+1}\right) \;-\; d\left(\Omega t - \frac{\pi}{M+1}\right)}{2\,\frac{\pi}{M+1}} \quad . \tag{2.12}$$

From a numerical point of view, application of $\mathcal{D}_M$ is equivalent to an explicit choice of sampling points for the evaluation of the derivative components. In this context, application of $\mathcal{D}_M$ is equivalent to a set of sampling points being naturally in phase with the harmonic associated to the leading truncation order $(M+1)$.

Recalling the modulated formulation of the truncation error $\mathcal{O}_M$ in eq. (2.11) and the trigonometric relationships listed in eq. (A.13), application of the alternative differential operator $\mathcal{D}_M$ yields

$$\begin{aligned}
\mathcal{D}_M\, \mathcal{O}_M(\Omega t) &= \frac{\mathcal{O}_M\left(\Omega t + \frac{\pi}{M+1}\right) - \mathcal{O}_M\left(\Omega t - \frac{\pi}{M+1}\right)}{2\,\frac{\pi}{M+1}} \\
&= \frac{\Theta_M\left(\Omega t + \frac{\pi}{M+1}\right)\cdot e^{\mathrm{i}(M+1)(\Omega t + \frac{\pi}{M+1})} - \Theta_M\left(\Omega t - \frac{\pi}{M+1}\right)\cdot e^{\mathrm{i}(M+1)(\Omega t - \frac{\pi}{M+1})}}{2\,\frac{\pi}{M+1}} \\
&+ \frac{\Theta_{-M}\left(\Omega t + \frac{\pi}{M+1}\right)\cdot e^{-\mathrm{i}(M+1)(\Omega t + \frac{\pi}{M+1})} - \Theta_{-M}\left(\Omega t - \frac{\pi}{M+1}\right)\cdot e^{-\mathrm{i}(M+1)(\Omega t - \frac{\pi}{M+1})}}{2\,\frac{\pi}{M+1}} \\
&= \quad - \;\mathcal{D}_M\Theta_M \cdot e^{\mathrm{i}(M+1)\Omega t} \;-\; \mathcal{D}_M\Theta_{-M} \cdot e^{-\mathrm{i}(M+1)\Omega t} \quad .
\end{aligned} \tag{2.13}$$

As shown in eq. (2.13), exploiting the structure of the differential operator $\mathcal{D}_m$ allows to avoid the undesired amplification of the truncation error $\mathcal{O}_M$.

In practice, the application of the differential operator $\mathcal{D}_M$ to a truncated Fourier series can be achieved by application of a sinc-based low pass filter. Given the definition of the normalised sinc-function in eq. (A.14), the application of the differential operator is for each of the m harmonics equivalent

to

$$\begin{aligned}
\mathcal{D}_M\left\{\widehat{d}_m(\Omega t)\right\} &= \mathcal{D}_M\left\{\widehat{d}_m \cdot e^{\mathrm{i}m\Omega t}\right\} = \widehat{d}_m \cdot \frac{e^{\mathrm{i}m(\Omega t+\frac{\pi}{M+1})} - e^{\mathrm{i}m(\Omega t-\frac{\pi}{M+1})}}{2\,\frac{\pi}{M+1}} \\
&= \widehat{d}_m \cdot \frac{e^{\mathrm{i}m(\Omega t)} \cdot e^{\mathrm{i}m(\frac{\pi}{M+1})} - e^{\mathrm{i}m(\Omega t)} \cdot e^{-\mathrm{i}m(\frac{\pi}{M+1})}}{2\,\frac{\pi}{M+1}} \\
&= \frac{e^{\mathrm{i}m(\frac{\pi}{M+1})} - e^{-\mathrm{i}m(\frac{\pi}{M+1})}}{2\,\frac{\pi}{M+1}} \cdot \widehat{d}_m \cdot e^{\mathrm{i}m(\Omega t)} = \frac{2\mathrm{i}\cdot\sin\left(m\frac{\pi}{M+1}\right)}{2\,\frac{\pi}{M+1}} \cdot \widehat{d}_m \cdot e^{\mathrm{i}m(\Omega t)} \\
&= (\mathrm{i}m)\,\frac{\sin\left(\pi\frac{m}{M+1}\right)}{\pi\frac{m}{M+1}} \cdot \widehat{d}_m \cdot e^{\mathrm{i}m(\Omega t)} = (\mathrm{i}m)\,\mathrm{sinc}\left(\frac{m}{M+1}\right) \cdot \widehat{d}_m \cdot e^{\mathrm{i}m(\Omega t)} \\
&= \frac{\partial}{\partial(\Omega t)} \left\{ \mathrm{sinc}\left(\frac{m}{M+1}\right) \cdot \widehat{d}_m \cdot e^{\mathrm{i}m(\Omega t)} \right\} \quad . \qquad (2.14)
\end{aligned}$$

According to eq. (2.14), the realised Lanczos-filter method affects the IFT by an attenuation of high-frequent oscillations via a multiplication of the Fourier coefficients $\widehat{d}_m$ with the so called Lanczos-σ_m-factors [79, 80]

$$\sigma_m := \mathrm{sinc}\left(\frac{m}{M+1}\right) = \frac{\sin\left(\pi\frac{m}{M+1}\right)}{\pi\frac{m}{M+1}} \qquad (2.15)$$

yielding a modified IFT algorithm $\mathcal{F}^{-1}_{\sigma_m}$ for the turbulence quantities $d(x,t)$ which can be summarised as

$$\mathcal{F}^{-1}_{\sigma_m}\left\{\widehat{d}_m(x)\right\} = \mathcal{F}^{-1}\left\{\sigma_m \cdot \widehat{d}_m(x)\right\} \quad . \qquad (2.16)$$

Therefore, the application of a modified hybrid-frequency-time-domain approach as sketched in Fig. 2.3 is recommended in this work in order to avoid the instabilities observed in the presence of undesired ringing. Instead of reconstructing the turbulence quantities $d^*(t)$ by referring to a conventional IFT as in Fig. 2.1, values for the turbulence variables $d^*_{\sigma_m}(t)$ required in the time domain are generated by taking advantage of the Lanczos-filter method described in eq. (2.16) highlighted by the index σ_m.

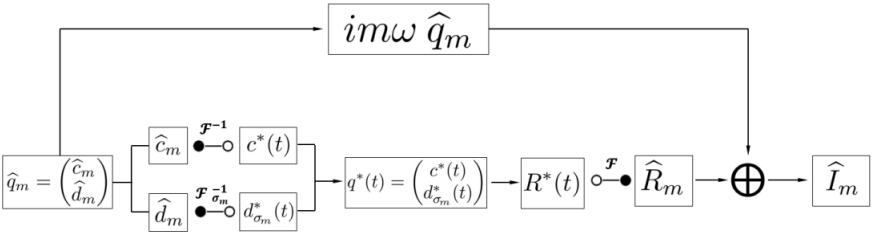

Figure 2.3.: MODIFIED HYBRID FREQUENCY-TIME-DOMAIN APPROACH BASED ON A LANCZOS-FILTERED IFT OF TURBULENCE QUANTITIES $\widehat{d}_m$ [63].

Since the conservative variables $c^*(t)$ are not affected in a critical order as in the case of turbulence quantities, the application of the filter is constrained to $d^*_{\sigma_m}(t)$. The basic idea by following a Fourier series approximation approach is to take advantage of the optimal approximation properties of the Fourier series for 2π-periodic functions. Since the unfiltered Fourier transform takes advantage of orthogonal 2π-periodic eigenfunctions, referring to the unfiltered Fourier expansion yields according to Parseval's theorem [78] the approximation minimising the approximation error of the Fourier series in L_2-norm. In order to maintain this desired benefit of a minimised root mean square error, the proposed filter method is not applied to the conservative flow quantities $c^*(t)$ in this work.

The impact of the realised Lanczos-filter method is highlighted by Fig. 2.4, where the wake introduced in Fig. 2.2 is displayed if the HB approaches proposed by Figs. 2.1 and 2.3 are applied. While following the conventional HB approach sketched in Fig. 2.1, the numerical simulation fails as a result of taking into account the unsteadiness in the applied turbulence model. By reconstructing the time history of the turbulence quantities in a conventional fashion, the unstable cells in the flow field suffer from the ringing induced by the Gibbs phenomenon. Accordingly, Fig. 2.4 shows the wake of the turbulence kinetic energy k obtained from the conventional HB approach for the same, now unstable cell with a solid line.

The oscillations in the solid line in Fig. 2.4 enforce critical values close

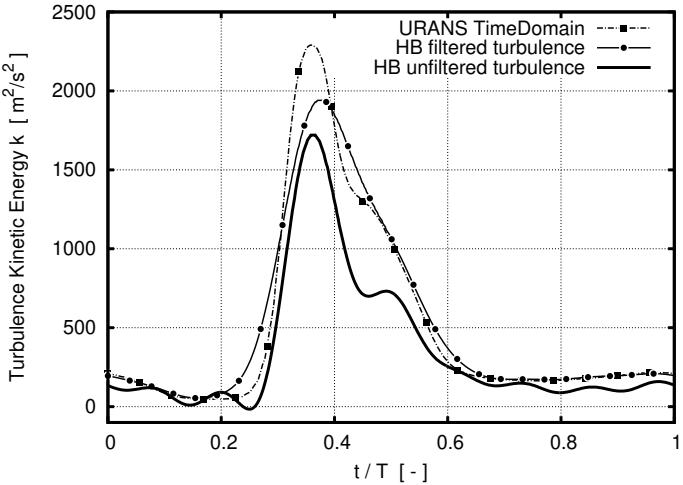

Figure 2.4.: WAKE OF TURBULENCE KINETIC ENERGY k DOWNSTREAM OF A LPT STATOR VANE OBTAINED FROM TIME AND FREQUENCY DOMAIN METHODS [63].

to zero for the turbulence kinetic energy k highlighting the negative impact of ringing while considering unsteady effects in the employed turbulence models. In fact, the turbulence kinetic energy is predicted to be negative in the region of $t/T \sim 0.25$ and a limiter enforcing feasible values close to zero is activated.

The behaviour of the Lanczos-filter method in terms of the pursued hybrid frequency-time-domain approach is compared to the unfiltered HB approach in Fig. 2.4. The same HB configuration is simulated by taking advantage of the described filter method and no problems concerning stability are detected during runtime. For the same cell in the exit plane of the considered stator row, the wake of the turbulence kinetic energy k is plotted in Fig. 2.4 with a solid-dotted line. In order to estimate the unsteady turbulence signals in both quality and quantity, the associated signal obtained from the unsteady solution in the time domain is shown in Fig. 2.4 with a dash-dotted line and solid squares.

The signal obtained from the filtered HB simulation shows no critical undershoots near the wake avoiding the application of a limiter function. The same level of turbulence kinetic energy k in the freestream region can be observed as predicted by the complete URANS benchmark performed in the time domain. Nevertheless, the comparison shown in Fig. 2.4 between the filtered IFT-approach and the result obtained from the time domain solver highlights also the limitations of the employed Lanczos-filter. The filtered signal predicts the wake to be wider and the peak level of the turbulence kinetic energy k in the wake is underestimated compared to the result obtained from the time-marching URANS simulation.

Following the convolution theorem [78] and the characteristic properties of the sinc listed in appendix A.2, the multiplication of the Fourier coefficients with the Lanczos-σ_m-factors in the frequency domain is equivalent to a convolution of the associated signal in the time domain with a rectangular window of the same period length. Therefore, the attenuation of the contributions in the higher harmonics decreases the capability of capturing sharp gradients and peak values as it is the case for various types of smoothing filters in the context of blurring.

As previously stressed in section 1.2, the key expectations in unsteady aerodynamics consist of providing reliable information about the unsteady behaviour of turbulent boundary layers and the underlying transient pressure fluctuations in particular. Hence, naturally the question arises if application of the proposed Lanczos-filter method affects the capability of the HB method to predict the transient behaviour within the boundary layers of excited turbomachinery components in an ineligible fashion. This aspect is addressed in the following chapter in which the focus lies on the unsteady transition behaviour in a LPT test rig operating at low Reynolds numbers. The capability to predict transient pressure fluctuations is addressed in chapter 4.

Chapter 3

Prediction of the Unsteady Transition Behaviour in a Low-Pressure Turbine Test Rig

Following the HB approach modified in this work according to Fig. 2.3, the question remains how taking advantage of the applied Lanczos-filter method affects the capability of the HB solver to predict unsteady turbulence phenomena in a satisfying fashion. Furthermore, by following a model order reduction approach of the unsteady flow problem - which is the basic idea of a frequency domain solution method - naturally the question arises which unsteady effects are worth being resolved and which can be neglected.

This chapter aims at answering both questions by evaluating the HB method's capability to predict unsteady transition mechanisms while the Lanczos-filter method is applied. The application of the Lanczos-filter is restricted to the transport variables linked to turbulence modeling $d(x,t)$. These are given here by turbulence kinetic energy k, turbulence dissipation rate ω as well as intermittency γ and transition Reynolds number Re_{Θ_t}.

Compared to [66], the results are validated by surface thin film measurement data providing time-resolved information about the unsteady transition behaviour. Furthermore, the HB results are benchmarked numerically by a comparison with results based on the application of a time-integration solution method. This finally allows to evaluate at what extent the pursued frequency domain method is able to reproduce unsteady turbulence

effects by taking advantage of the developed Lanczos-filter approach. In the following, the investigated test facility and the employed measurement data are introduced briefly. The applied numerical setups are described for both time and frequency domain approaches and the results of both solution methods are presented. The results are compared to the underlying unsteady measurement data and the capability of the Lanczos-filtered HB solver to reproduce unsteady transition effects within the investigated boundary layer is discussed.

3.1. Low-Pressure Turbine Test Facility

The time-resolved transition measurements of the turbine test rig investigated in this chapter were performed at the *Advanced Turbine Research Demonstrator* (ATRD) located at the Institute of Aircraft Propulsion Systems (ILA) at the University of Stuttgart, Germany. Its integration in the local *Altitude Test Facility* (ATF) allows to provide test conditions being representative of in-flight performance points associated to altitudes particularly met in the operation map of an aircraft engine.

In particular, the experimental setup enables flow conditions preserving the similarity with regard to both Mach and Reynolds number for the investigated rig geometry being representative of a modern low pressure turbine (LPT) design. The operating point evaluated in this work is characterised by the flow conditions at the exit plane of the first stator vane and corresponds to a Reynolds number of $\mathrm{Re}_{\mathrm{V2,in}} = 80{,}000$ and a Mach number of $\mathrm{Ma}_{\mathrm{V2,in}} = 0.65$. The associated pressure ratio over the complete two-stage test rig is given by $\Pi_{\mathrm{tot}} = 1.9$. Detailed information about the ATRD and ATF test facility can be found in previous publications such as [83, 84]. Figure 3.1 shows an overview of the investigated geometry, while the associated blade count is summarised in Tab. 3.1.

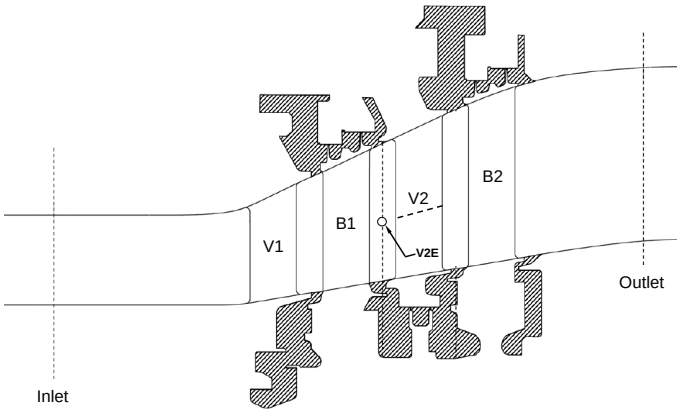

Figure 3.1.: MERIDIONAL VIEW OF THE ATRD-RIG [84]. CAVITIES (SHADED) ARE NOT CONSIDERED IN THE SIMULATIONS.

3.1.1. Mounted Measurement Devices

Time Averaged Pressure Distribution. The time averaged pressure distribution of the second stator vane (V2) is measured by taking advantage of static pressure tappings located in the midspan section of the airfoil. Fourteen tappings are mounted on the suction side and twelve on the pressure side of the airfoil, respectively. The stagnation pressure $p_{\mathrm{t,\,ref}}$ is determined via a kiel head on the leading edge at 50% channel height.

Surface Thin Film Gauges. In order to provide information about the unsteady evolution of the transition behaviour within the investigated LPT rig, a thin film sensor array is installed along the surface of the suction side of a second stage stator vane. The thin film gauges cover a range from 4.2% to 97.9% of the axial chord length l_{ax}. The sensor array is operated in a constant temperature mode providing information about the wall shear stress τ_w by relating the instantaneous anemometer output voltage with a reference voltage recorded under zero-flow conditions. The measurements were conducted in cooperation between ILA and MTU Aero Engines AG.

Table 3.1.: BLADE COUNT OF THE INVESTIGATED LPT-TEST FACILITY.

Blade Row	Number of Blades
Stator 1 (V1)	60
Rotor 1 (B1)	55
Stator 2 (V2)	58
Rotor 2 (B2)	57

Details concerning the instrumentation and the underlying data acquisition can be found in [84].

3.1.2. Measured Quantities

Since the information gained from the installed measurement devices rather give information about the present wall shear stress τ_w, the measurement data need further interpretation in order to work as an indicator for transition. The approach to identify transition based on the available thin film sensor data refers to [13, 14, 84] and is recapitulated briefly in the following.

This is achieved by a discussion of measurement data at the stator midspan for two representative inflow conditions - wake and freestream - characterising the transition modes acting within the investigated suction side's boundary layer. In the case of a wake induced by an upstream rotor blade impinging on the investigated stator vane, a bypass induced transition mode can be observed. If the stator vane operates at conditions in between two wakes, the transition within the measured boundary layer is induced by the presence of a flow separation.

Third Central Moment (Skewness). The skewness g_m is defined according to eq. (A.18) as the third central moment μ_3 normalised with the standard deviation σ. In general, the third moment μ_3 of a data set provides a measure of both quantity and quality of the asymmetry about its mean value. Therefore, a data set with a skewness close to zero marks a symmetric

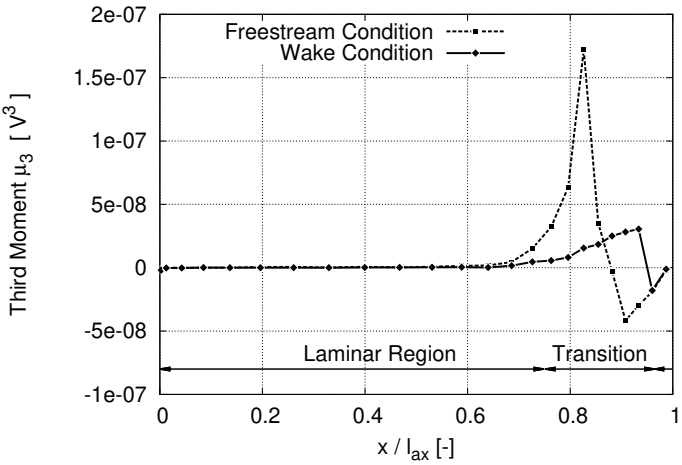

Figure 3.2.: THIRD MOMENT μ_3 OF THIN FILM SENSOR DATA ALONG THE SUCTION SIDE OF THE SECOND STATOR VANE.

deviation around its mean value.

The variation of the third moment μ_3 along the investigated stator suction side can be used in the first place to identify the transition region within the measured boundary layer. The knowledge about the transition behaviour can then be used in a subsequent step to assess values of the associated boundary layer intermittency γ.

In the context of constant temperature anemometry, the measured quantity is the electrical voltage within the underlying fibre probes which is directly linked to the heat flux of the fibres. The presence of turbulence structures within the investigated boundary layer enhances the transport of energy into the flow and therefore leads to an increase of the measured electrical output voltage. In regions of transition, the boundary layer features both laminar and turbulence structures leading to an asymmetric set of measurement data. Taking advantage of this asymmetry within the recorded measurement data allows to identify the transition regime in the investigated boundary layer as described in Fig. 3.2.

Figure 3.2 shows the characteristic trend of the third moment μ_3 within a boundary layer with transition from laminar to turbulent flow while facing freestream conditions with a dashed line. The third moment measured at mid-span is displayed along the axial chord length l_{ax}. Starting at the vane's leading edge at $x/l_{ax} = 0$, the boundary layer shows laminar behaviour with fluctuations normally distributed around the measured mean value.

Thus, the third moment μ_3 is zero in the range between $0 < x/l_{ax} < 0.6$ where the vane faces laminar flow conditions only. The transition process starts after $0.6 < x/l_{ax}$ where increasing values of $\mu_3 > 0$ can be observed due to the rising presence of turbulence structures. The third moment of the measured data set is positive in the first phase of transition since the turbulence structures leading to an increase in the recorded values of electrical output voltage are still outnumbered.

Once the transition is half completed - a condition where the boundary layer appears at as many laminar as turbulent states - the fluctuations in the data set about its mean are normally distributed again. This point is indicated in Fig. 3.2 by a change in the sign of the third moment at $x/l_{ax} \sim 0.88$. In the following, the turbulence structures begin to dominate the boundary layer in the region between $0.88 < x/l_{ax} < 0.95$ leading to negative values in the third moment μ_3. Once the transition is completed and the boundary layer has a completely turbulent character, the fluctuations about its (now higher) mean value are statistically distributed again and the third moment μ_3 is zero. For the transition process in case of freestream conditions - sketched in Fig. 3.2 with a dashed line - this is the case after $0.95 < x/l_{ax}$.

The equivalent measurement data associated to the case of wake inflow conditions is plotted in Fig. 3.2 with a solid line. Compared to the measurement data at freestream conditions, the same behaviour can be observed though indicating a retarded transition process at lower levels of skewness and an equilibrium shifted downstream to $x/l_{ax} \sim 0.92$. The evolution in time of the skewness as shown in Fig. 3.2 is used in the following to assess the capability of the applied numerical flow solver to predict the unsteady transition behaviour of the investigated stator vane.

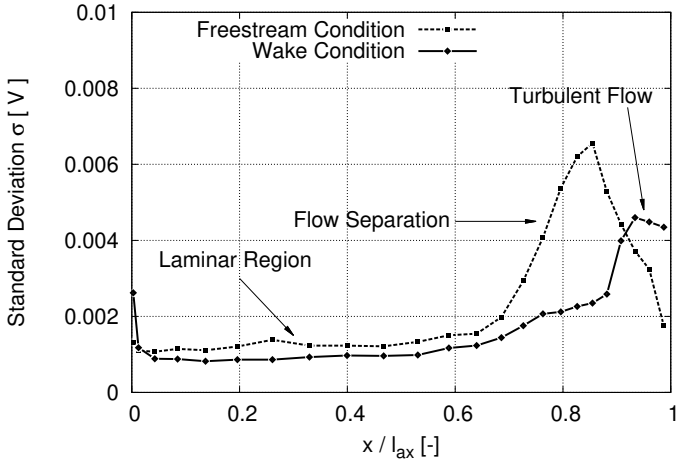

Figure 3.3.: STANDARD DEVIATION σ ALONG THE SUCTION SIDE OF THE SECOND STATOR VANE.

Second Central Moment (Variance/Standard Deviation). A second quantity giving helpful information about the transition behaviour within the investigated boundary layer is the second central moment denoted as variance μ_2 of the recorded data set. The variance is a measure of the statistical dispersion of a quantity about its mean value. Thus, it gives information about how far the elements of a recorded data set are spread out from its mean value. Due to its definition by the square of the standard deviation σ according to eq. (A.17), both quantities can act as a quantitative measure for the fluctuations within the investigated data set.

Since the major difference between a laminar and a turbulent boundary layer is the occurrence of turbulence fluctuations, a substantially higher level of statistical dispersion is expected in the presence of transition. In Fig. 3.3, the trend of the standard deviation σ for the same wake condition as shown in Fig. 3.2 is plotted along the axial chord length l_{ax} with a solid line. In the laminar region from $0 < x/l_{\mathrm{ax}} < 0.7$ a rather constant level of σ and thus in the order of fluctuations within the recorded data set can be noticed. Due to

the increasing presence of turbulence structures in the region of transition between $0.7 < x/l_{ax} < 0.95$, a continuous rise of the standard deviation σ occurs. Once the transition is completed, there are no further substantial changes in the level of standard deviation indicating a higher degree of fluctuations in the turbulent boundary layer.

The dashed line in Fig. 3.3 shows the trend of the standard deviation σ at the freestream conditions introduced in Fig. 3.2. Both bypass and separation induced transition mechanisms are expected to occur during the operation of the test rig. Since it can prove to be difficult to distinguish between the single transition modes by focusing on the skewness behaviour alone, the additional analysis of the standard deviation turns out to be very helpful in order to identify regions of flow separation. As in the case of wake conditions, a laminar onset in the accelerated region of $0 < x/l_{ax} < 0.7$ along the suction side can be noticed. By passing the decelerated region of the vane's suction side up to $x/l_{ax} < 0.85$, a substantial gain in the level of standard deviation within the recorded measurement data can be observed. These values exceed substantially even the level of fluctuation recognised after the completed transition process in the case of wake conditions. This information can be used as an indicator for the presence of separated boundary layer regions since in the presence of a separation bubble very high fluctuations are expected.

3.2. Evaluation Setup

In this section, a brief overview of the assessed numerical configurations is given. This includes a description of the underlying solver structures and a specification of the numerical setups for the unsteady simulations in the time and frequency domain, respectively. In this chapter, for all simulations Wilcox' $k-\omega$ turbulence model [68] in combination with a two equation transition model based on Menters $\gamma-\mathrm{Re}_{\Theta_t}$ framework provided by [20, 21] is applied.

Setup for Unsteady Simulations in the Time Domain. In contrast to steady simulations aiming at an averaged solution of the flow problem, the complete solution of the URANS equations performed in the time domain requires the transport of a wake associated to a blade row into its adjacent downstream row. Furthermore, the dispersion of up- and downstream pressure waves has to be taken into account to resolve all unsteady interactions between the respective blade rows. Therefore, the mutual communication between adjacent blade rows is realised by referring to a zonal interface approach [85] requiring identical pitch sections up- and downstream of the interfaces. Recalling the blade count described above, a full wheel simulation of the complete test rig has to be performed.

The resulting mesh for the unsteady time domain simulations consists of approximately 620 million cells leading to high requirements concerning memory and processing power. For all stator and rotor surfaces, a dimensionless wall distance of $y^+ < 5$ is provided by the mesh. At both inlet and outlet, non-reflecting boundary conditions based on a formulation in the frequency domain [76] are imposed. The simulations are performed by resolving a complete revolution of the rotor shaft with 2048 physical timesteps which enables at least 34 physical timesteps per blade and vane passing, respectively. The underlying time integration method is based on a backward Eulerian scheme of second order [86]. Within each physical timestep a relaxation in pseudo-time related to an implicit Gauss-Seidel method with multiple solver sweeps is applied. In order to provide a periodic state at the end of the simulation, convergence is assessed according to [87]. The simulation is stopped after three complete revolutions of the rotating blade rows while the third is mainly performed to record the data required in the context of the unsteady evaluation of the flow field over a complete revolution.

Harmonic Balance Setup for the Frequency Domain. As in the case of a steady simulation setup, a single passage mesh with periodic boundaries in pitchwise direction can be employed for the unsteady evaluation in the frequency domain. Therefore, the same mesh structures as for the steady

initialisation are exploited leading to a grid consisting of approximately 10 million cells. Again, a dimensionless wall distance of $y^+ < 5$ is not exceeded. At both in- and outlet of the configuration, non-reflecting boundary conditions equivalent to the boundary conditions applied for the time domain solver are prescribed.

The interaction between the respective sources of unsteadiness at differing frequencies and inter blade phase angles (IBPA) is treated by exploiting the harmonic set approach of the applied Harmonic Balance solver [41]. Each unsteady interaction between adjacent blade rows is associated to an explicit combination of a base frequency and IBPA. Since the higher harmonics of these interactions are defined as integral multiples of the respective combinations of base frequency and IBPA, they can be summarised in a so called shared harmonic set [41].

The communication enabling the unsteady interaction between adjacent blade rows can then be realised via a transfer of the harmonic content in each considered harmonic set [77]. The resolved harmonic sets, namely their underlying base frequencies and their associated harmonics are summarised in Tab. 4.1 where BPF_i and VPF_i denote the blade/vane passing frequency of the i-th rotor and stator, respectively. All considered harmonic content is resolved with 6 harmonics and coupled with the time averaged flow field as indicated by the zeroth harmonic entries in Tab. 4.1.

In particular, the unsteadiness in the first stator row resulting from the interaction with the potential field of the downstream rotating blade row at its associated blade passing frequency BPF_1 is taken into account and referred to in the following as HS1.

For the first rotor blade row, the unsteady conditions linked to its operation in the wake of the upstream stator row at VPF_1 are summarised in set HS2 which includes the impact of the stator 1 potential field at the same frequency as well. Furthermore, the transient effects at VPF_2 associated to the potential field of the second stator row are resolved in set HS3. The downstream traveling acoustic modes generated in the first stator row by a scattering of the rotor 1 potential field is considered in an additional set denoted in Tab. 4.1 as HS4.

Table 3.2.: CONSIDERED HARMONIC SETS WITH BASE FREQUENCIES AND NUMBER OF ASSOCIATED HARMONICS.

Set	Blade Row	Base Frequency	# of Harmonics
HS1	Stator 1	BPF_1	0 1 2 3 4 5 6
HS2	Rotor 1	VPF_1	0 1 2 3 4 5 6
HS3	Rotor 1	VPF_2	0 1 2 3 4 5 6
HS4	Rotor 1	$BPF_1 \dashrightarrow VPF_1$	0 1 2 3 4 5 6
HS5	Stator 2	BPF_1	0 1 2 3 4 5 6
HS6	Stator 2	BPF_2	0 1 2 3 4 5 6
HS7	Stator 2	0 (S1 Clocking Mode)	0 1 2 3 4 5 6
HS8	Stator 2	$BPF_1 \dashrightarrow VPF_1 \dashrightarrow BPF_1$	0 1 2 3 4 5 6
HS9	Rotor 2	VPF_2	0 1 2 3 4 5 6

In the same way, the unsteadiness in the second stator row due to both wake and potential field of the upstream rotor 1 blade is provided by HS5 whereas the potential effect of the second rotor blade row located downstream is summarised in HS6. In order to include the impact of clocking between the first and the second stator row, a clocking set HS7 is included in the frequency domain simulations. Since the acoustic modes scattered in the first stator and travelling downstream are expected to be of major importance as indicated by [66, 67], they are resolved in an additional set denoted as HS8 with 6 harmonics as well. Finally, the unsteady interaction between wake and potential field of the second stator row is considered in the second rotor passage with HS9.

In order to avoid the undesired impact of the Gibbs phenomenon on the numerical stability, the Lanczos-filter method as described in section 2.4 is employed for the harmonic content of quantities required in the context of turbulence modeling. These are given by turbulence kinetic energy k, dissipation rate ω, intermittency γ and transition Reynolds number Re_{Θ_t}).

3.3. Unsteady Evolution of Transition and Flow Separation

In order to assess the capability of both time and frequency domain methods to predict the unsteady transition behaviour, results of the underlying intermittency and the shape factor H_{12} are compared to the third moment μ_3 and the standard deviation σ of the available thin film measurement data. Since the intermittency γ varies within the boundary layer with increasing wall distance n, intermittency values γ^*_δ averaged over the boundary layer thickness δ are considered in the following. The assessed values of both averaged intermittency γ^*_δ and shape factor H_{12} are provided by an integration over the boundary layer thickness δ along the normal direction n of the blade contour. The shape factor $H_{12} := \frac{\delta_1}{\theta}$ is evaluated according to its definition via the displacement thickness δ_1 and the momentum thickness θ

$$\delta_1 := \int_0^\delta \left(1 - \frac{\rho u}{\rho_\infty u_\infty}\right) \mathrm{d}n \qquad \theta := \int_0^\delta \frac{\rho u}{\rho_\infty u_\infty}\left(1 - \frac{u}{u_\infty}\right) \mathrm{d}n \tag{3.1}$$

with ρ_∞ and u_∞ denoting the freestream density and the freestream velocity, respectively. Since for the investigated low pressure turbine the transition takes place in regions close to the vane's trailing edge as indicated by Fig. 3.2, the focus is in the following on the results in the region between $0.5 < x/l_{\mathrm{ax}} < 1$.

Prediction of Transition and Flow Separation in the Time Domain

The space-time diagram of the intermittency γ^*_δ obtained from the full-wheel simulation performed in the time domain is shown in Fig. 3.4. The evolution of the intermittency is displayed along $0.5 < x/l_{\mathrm{ax}} < 1$ over three rotor 1 periods at 50% channel height. The dashed line in Fig. 3.4 indicates the analysis line linked to the freestream conditions presented previously in the context of Fig. 3.2.

For freestream conditions, the time domain solver predicts a substantial gain in the intermittency in the region between $0.75 < x/l_{\mathrm{ax}} < 0.85$ until

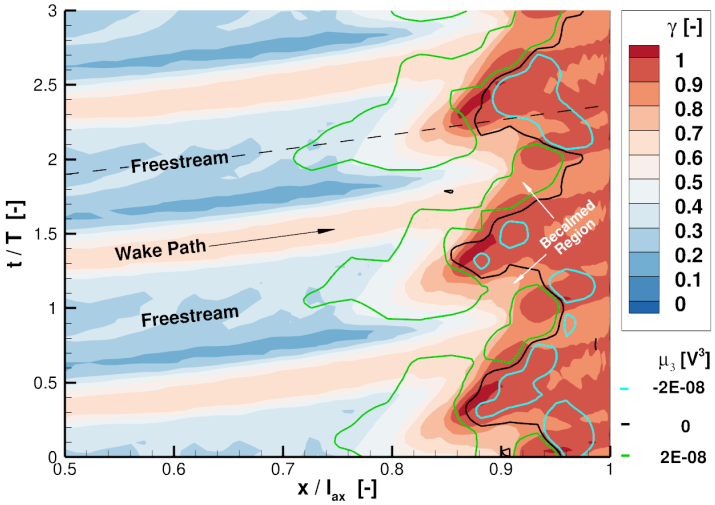

Figure 3.4.: TIME DOMAIN RESULTS OF INTERMITTENCY γ_δ^* AND SKEWNESS OF ASSOCIATED THIN FILM MEASUREMENT.

high intermittency values close to 1 can be observed. In addition to the evolution of the intermittency in Fig. 3.4, the space time diagram of the associated shape factor H_{12} is shown in Fig. 3.5. Again, the dashed and dashed-dotted lines can be matched with the trends of the standard deviation σ shown in Fig. 3.3 for freestream and wake conditions, respectively.

Considering freestream conditions first, the increasing values of intermittency between $0.75 < x/l_{\mathrm{ax}} < 0.85$ can be matched with high values in the shape factor in the order of $H_{12} \sim 4$. The high levels in both intermittency γ_δ^* and shape factor H_{12} in the range of $0.75 < x/l_{\mathrm{ax}} < 0.9$ refer to a separation of the flow in this region. Close to the vane's trailing edge, the decline in the values of the shape factor to $H_{12} \sim 1.8$ indicate a reattachment of the separated flow by means of a then completely turbulent boundary layer. Therefore, the prediction of separation induced transition in combination with turbulent reattachment in the range of $0.75 < x/l_{\mathrm{ax}} < 1$ can be held for the investigated stator 2 in the case of freestream conditions.

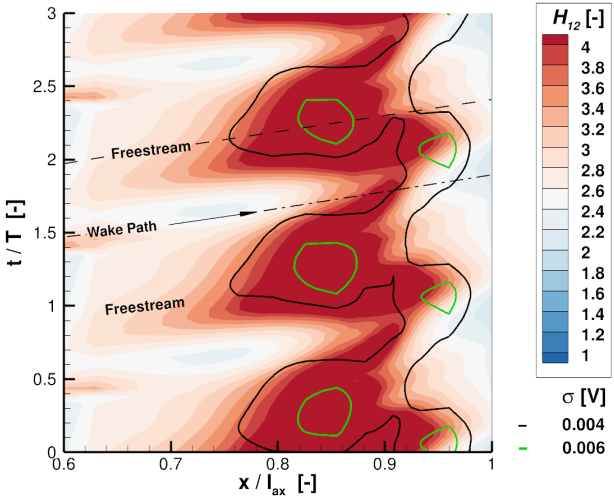

Figure 3.5.: TIME DOMAIN RESULTS OF SHAPE FACTOR H_{12} AND STANDARD DEVIATION OF THIN FILM MEASUREMENT.

Once the vane faces the $j = 1, 2, 3$ respective wakes of the upstream blade row - linked in Fig. 3.4 to an increased entry level of γ^*_δ at $(j-1)+0.2 < (t/T)*j < (j-1)+0.4$ - the freestream transition is suppressed and shifted downstream along the suction side. The associated becalmed regions are expressed in Fig. 3.4 in terms of a decayed increase of the underlying intermittency γ^*_δ in the range of $0.9 < x/l_{\mathrm{ax}}$. As a consequence of the increased turbulence level within the wake, the trend of the associated shape factor H_{12} shows in Fig. 3.5 a reduction of the separation bubble linked to high values of $H_{12} \sim 4$ between $0.85 < x/l_{\mathrm{ax}} < 0.9$ alone. The decrease of the shape factor to $H_{12} \sim 1.8$ in the presence of the respective wakes immediately before and after the separation regime at $0.7 < x/l_{\mathrm{ax}} < 0.75$ and $0.95 < x/l_{\mathrm{ax}}$ hints at a bypass transition mode disrupted by a short region of separation.

The numerical results of the intermittency γ^*_δ in Fig. 3.4 and the shape factor H_{12} in Fig. 3.5 are complemented by the third moment μ_3 and standard

deviation σ of the associated thin film measurement data. The black solid line in Fig. 3.4 refers to the evolution of passing the zero skew marking the point of 50% transition in the provided hot film measurements whereas the green and cyan line are equivalent to regions of predominantly laminar and turbulence structures, respectively.

Comparing the black line of 50% transition with the numerically predicted distribution of intermittency, in particular in the case of freestream conditions a close agreement with the axial position of the increase to high levels of intermittency γ^*_δ can be observed. Since in the context of turbulence modeling the intermittency γ is used to enhance the production of turbulence kinetic energy k, intermittency values close to 1 indicate that the production of turbulence kinetic energy is provided at its full extent. In order to trigger the point of a completed transition, the state of balanced laminar and turbulence conditions is a reasonable point to do so. Nevertheless, in the presence of the becalmed regions induced by the passing wakes from the upstream located rotor blades high values of intermittency γ^*_δ occur somewhat earlier than the measured point of transitional equilibrium. Since this leads potentially to an overestimation of the turbulence kinetic energy k within the wake, the bypass induced transition mechanism might be predicted too early.

The tendencies observed in the intermittency γ^*_δ for both freestream and wake conditions are confirmed by an analysis of the standard deviation σ of the measurement data in Fig. 3.5. The solid lines in Fig. 3.5 referring to an intermediate (black) and a very high level (green) of standard deviation σ show that in the case of freestream conditions the predicted flow separation can be observed as well. Furthermore, its shape and location agree with the standard deviation of the available measurement data. The suppressed becalmed region is qualitatively captured very well too while the transition leading to the reattachment of the flow is predicted earlier by the numerics than in the measurement though. As already observed in the context of the intermittency in Fig. 3.4, the impact of the wake is overpredicted leading to a slightly precipitated transition of the boundary layer in the case of wake conditions.

Prediction of Transition and Flow Separation in the Frequency Domain

In order to evaluate the capability of the applied HB solver taking advantage of the Lanczos-filter method to predict the alternating behaviour of both separation and bypass induced transition, the space-time diagrams for intermittency γ^*_δ and shape factor H_{12} are shown in an analogous fashion in Fig. 3.6 and Fig. 3.7, respectively. Comparing the evolution of the intermittency γ^*_δ in Fig. 3.6 predicted by the HB solver with the associated time domain result shown in Fig. 3.4, a delayed incline in the result generated in the frequency domain can be observed. This is the case for both freestream and wake conditions shifting the region of rising intermittency approximately $\Delta x/l_{\mathrm{ax}} \sim 0.05 = 5\%$ downstream along the stators suction side. Furthermore, the intermittency turns out to appear at a quantitative slightly lower level than observed in the time domain solution. However, the characteristic behaviour in the evolution of the intermittency γ^*_δ due to separation and bypass induced transition mechanisms is reproduced by the applied HB solver.

This is also confirmed by taking into account the skew of the available thin film measurement data. Accordingly, representative levels of the third moment μ_3 are added to Fig. 3.6 in the same manner as previously described in the context of Fig. 3.4. Due to the downstream shift of emerging intermittency regions, the production of turbulence kinetic energy k is now triggered rather at the transitional equilibrium between laminar and turbulence structures marked with the black solid line. While for freestream conditions both states correspond almost completely, higher levels of intermittency γ^*_δ occur in the presence of wake conditions along the entire suction side amid the increased entry level of turbulence kinetic energy k within the rotor wake. Nevertheless, the shape of the becalmed regions is captured qualitatively very well by the applied frequency domain solver when compared to the skew of the underlying measurement data.

The space-time diagram of the associated shape factor H_{12} generated in the frequency domain is shown in Fig. 3.7. In comparison to the time domain results displayed in Fig. 3.5, the HB solver is able to reproduce the

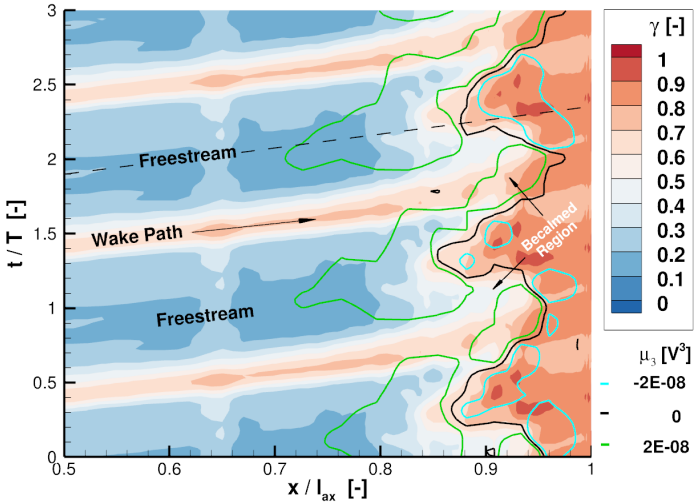

Figure 3.6.: HARMONIC BALANCE RESULTS OF INTERMITTENCY γ^*_δ AND SKEWNESS OF ASSOCIATED THIN FILM MEASUREMENT.

separation bubble with regard to its shape, its location and its suppression when passing the wake induced by the upstream rotor blades.

Major differences to the results provided by the time domain method can be observed locally in the becalmed regions though. While the impact of the separation bubble is alleviated and shifted downstream in the time domain solution, the shape factor H_{12} predicted by the HB method shows a complete interruption of the separated flow region by the wake indicating a rather complete bypass state of transition. The standard deviation σ of the available hot film data, displayed in Fig. 3.5 and Fig. 3.7 by solid lines, confirms the behaviour predicted by the time domain solver, since levels of σ associated to regions of flow separation are still present in the course of the passing wake.

As the time domain solver, the solver employed in the frequency domain overestimates the impact of the wake leading to higher levels of both intermittency γ^*_δ (Fig. 3.6) and shape factor H_{12} (Fig. 3.7). In the case of the applied HB method, this numerical imperfection appears to affect the

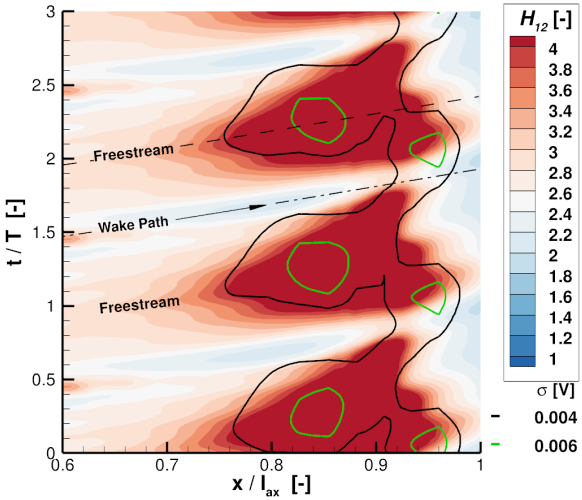

Figure 3.7.: HARMONIC BALANCE RESULTS OF SHAPE FACTOR H_{12} AND STANDARD DEVIATION OF ASSOCIATED THIN FILM MEASUREMENT.

result even stronger if compared to the results provided by the time domain solution process.

By following the HB approach and taking advantage of model order reduction of the flow problem by focusing on a particular choice of considered frequencies, the unsteady character of the flow is assumed to be predominantly periodic. In order to estimate the capability of the pursued approach of model order reduction to reproduce the result provided by the established time domain solution method, the spectral content in both solutions has to be taken into account. The according spectral content of the turbulence kinetic energy k at the entry midspan plane V2E (see Fig. 3.1) of the investigated second stator vane is shown in Fig. 3.8.

The spectrum associated to the complete solution of the URANS equations in the time domain is plotted in red while the reduced spectrum of the HB solution is displayed in black. Obviously, the spectrum of the HB solution shows only harmonic content in circumferential modes that are considered

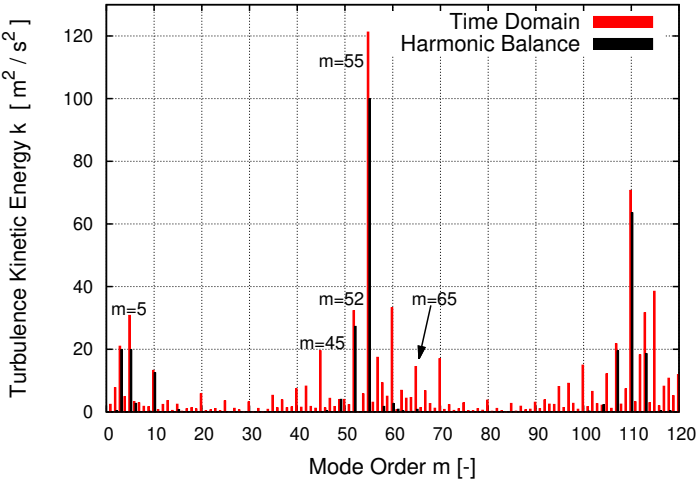

Figure 3.8.: CIRCUMFERENTIAL SPECTRA OF FLUCTUATIONS OF TURBULENCE KINETIC ENERGY k AT 50 % CHANNEL HEIGHT OF THE SECOND STAGE ENTRY.

according to Tab. 4.1. The order of the considered modes is captured well by the frequency domain solver compared to the solution predicted by the time marching solution method. Nevertheless, the HB solver tends to underestimate the fluctuations of the turbulence kinetic energy in the respective analysis plane.

Furthermore, Fig. 3.8 allows to estimate whether and to what extent the underlying assumption of periodic unsteadiness is valid for the investigated LPT rig. The spectrum of the complete URANS solution plotted in red shows as expected the highest fluctuations in the mode order $m = 55$ associated to the wake of the upstream rotor blade. In addition, substantial harmonic content is shown in the circumferential orders referring to acoustic modes of multiple order of 5, namely $m = \{5, 10, 20\}$, $m = \{45\}$, $m = \{60, 65, 70\}$ and $m = \{100, 115\}$.

Recalling the blade count of the respective rows, these modes can be associated to the acoustic interaction between the stator and the rotor of

Table 3.3.: COMPUTATIONAL RESOURCES OF THE SOLUTION METHODS IN TIME AND FREQUENCY DOMAIN.

Solution Method	$\Delta\eta_{\text{is,Stage2}}$	CPU-Time	Wall-Time
Time-Marching	-1.82%	100 000 h	250 h
Harmonic Balance	-1.29%	5000 h	100 h

the first stage traveling downstream in the second stator row. As can be seen in Fig. 3.8, the harmonic content defined in Tab. 4.1 by HS4 and HS8 is not able to represent all of these modes. While the modes associated to the circumferential order $m = \{5, 10, 15\}$ are captured properly, the energy-rich fluctuations of order $m = \{45, 60, 65, 70, 100, 115\}$ are not present at all. Since in the case of the HB method all fluctuations beyond the spectrum in Fig. 3.8 are mixed out during the solution process, this leads to an increased entry level of turbulence intensity within the investigated stator row.

In order to overcome the local deviations between both solution methods in the presence of the passing wake, the missing harmonic content has to be resolved by the HB setup as well. Nevertheless, since the differences in the prediction of the unsteady transition behaviour are rather small and of local nature and since both solvers and the measurement show a periodic alternation between the respective transition modes, the assumption of a predominantly harmonic character of the transition process can still be justified.

In general, judging the practical value of a model order reduction approach requires to relate the quality of the gained results to the invested numerical efforts. Thus, in Tab. 3.3 the benefit to predict the second stage's isentropic efficiency $\eta_{\text{is,Stage2}}$ based on an unsteady assessment of the underlying flow field is related to the numerical resources consumed by the respective solution approach in the time and the frequency domain, respectively. Calculating the difference between the isentropic efficiency based on the solutions of

the steady and unsteady state according to

$$\Delta\eta_{\text{is,Stage2}} := \eta_{\text{is,Stage2,URANS}} - \eta_{\text{is,Stage2,RANS}} \quad , \tag{3.2}$$

the unsteady reference performed in the time domain by a complete solution of the URANS equations predicts the unsteady isentropic efficiency of the second stage to be 1.82 % lower than in the steady state.

In the same way, the solution of the URANS equations by taking advantage of the HB model order reduction approach predicts the unsteady isentropic efficiency of the second stage to be 1.29 % lower than its steady counterpart. Considering the isentropic efficiency to be one of the key parameters assessing the aerodynamic performance of turbomachinery components, exploiting the HB approach based on the setup sketched in Tab. 4.1 allows to close the gap between steady and unsteady evaluation to a substantial though not to its full extent.

However, in addition to the quality of the results the required numerical efforts have to be taken into account to judge the value of a model order reduction approach. These are summarised in Tab. 3.3 by means of invested time and processing power. The unsteady simulation performed in the time domain requires a full-wheel simulation and therefore a tremendous effort with regard to CPU's and RAM. Despite the overall run time of the time domain solver is only about 2.5 times higher, the huge number of employed processing units leads to up to 20 times higher CPU-times. Hence, taking advantage of the applied HB method is obviously an attractive compromise between low numerical costs and acceptable accuracy of the result, given the high numerical requirements summarised in Tab. 3.3.

3.4. Conclusion

The results of unsteady simulations performed in both time and frequency domain are presented with focus on their capability to predict the unsteady transition behaviour of a LPT stator vane. In order to improve the behaviour of the applied Harmonic Balance configuration in terms of stability, a

Lanczos-filter method as proposed in section 2.4 is applied during the iDFT of turbulence variables. Space time diagrams of the investigated stator suction side are discussed with regard to the unsteady evolution of underlying values of intermittency γ and shape factor H_{12}. The numerical results are compared with both the third moment and the standard deviation of available surface thin film data. Both solver methods are able to reproduce the unsteady behaviour of the present transition mechanisms of bypass and separation induced transition suggested by the measurement data. Shape and location of the separation bubble indicated by the hot film data are captured well in both solution methods while local differences in the case of bypass induced transition can be observed.

In this context, the applied time domain solver is in general able to reproduce the transition behaviour very well which is also supported by the measurement data. The unsteady transition behaviour predicted by the Harmonic Balance solver relying on the Lanczos-filter method differs locally overestimating the impact of the passing wake slightly. If an even further agreement between the results predicted in the time and the frequency domain is required, additional harmonic content has to be taken into account in the setup of the frequency domain method.

The spectrum of the solution generated by the time domain solver containing all unsteady effects indicates a far spread harmonic spectrum at the entry of the measured stator row. Therefore, the necessity of including further unsteady interactions between the respective blade rows has to be checked carefully since this happens at the expense of additional numerical effort concerning memory and processing power.

In fact, the presented Harmonic Balance approach already allows to consider a substantial share of the unsteady effects affecting the assessment of the isentropic efficiency of the investigated test rig. Recalling the tremendous benefit concerning invested CPU-time of the simulation performed in the frequency domain, referring to the Harmonic Balance approach yields a suitable compromise between quality of the obtained result and computational efficiency.

Chapter 4

Prediction of the Transient Pressure Fluctuations in a Low-Pressure Turbine Cascade

In the previous chapter, the capability of the HB method to resolve turbulence effects in an unsteady framework is shown if the solution process is modified according to section 2.4. This discussion is expanded in the following chapter on the HB solver's capability to predict unsteady pressure fluctuations. This is achieved by a validation of numerical results against time-resolved measurement data conducted on the stator surface of a LPT cascade. Again, results from a high-resolved time-integration solution process serve as a numerical benchmark. Based on these results, the potential benefit of the developed Lanczos-filter approach with regard to its application in the context of an aeroelastic design process is assessed.

In the following, the investigated LPT cascade facility and the conducted measurement data are introduced briefly. The details of the realised numerical setups are described for both time-integration and frequency domain approaches and the results of the respective solution methods are presented. The results are validated against the available unsteady measurement data and the capability of the Lanczos-filtered HB solver to predict transient pressure fluctuations acting on the excited stator cascade is evaluated.

4.1. Low Pressure Turbine Cascade Test Facility

The test conditions, the realised instrumentation and a detailed discussion of the quality of the exploited measurement data is presented in [88]. However, since the results published by [88] are used as a validation basis here, a brief overview of the underlying test environment is given in the following. The time resolved measurements of the LPT cascade investigated in this work were conducted in the High-speed Cascade Wind Tunnel (HGK) located at the Institute of Jet Propulsion at the Bundeswehr University Munich, Germany. The linear LPT cascade used for validation purposes in this work consists of seven stator vanes. A general overview of the investigated geometry is displayed in Fig. 4.1.

Unsteady inflow conditions being representative of the wakes of an upstream located blade row are induced by the installation of a wake generator as proposed by [89, 90]. The wake generator assembly consists of cylindrical steel bars of 2mm diameter fixed on two moving belts. The belts rotate continuously in a loop with a constant circumferential speed providing a periodic inflow condition at a frequency of $f \sim 500$ Hz. Detailed information concerning the impact of the realised wake generator on the established flow field can be found in [91]. Although there are constraints with regard to limitations in the rotational speed of the applied wake generator assembly, the results based on the investigated device are transferable to engine like Strouhal numbers Sr and flow coefficients Φ, respectively, as stated in [92].

The flow condition at the inlet is determined by a total pressure level of $p_{\mathrm{t,in}} \sim 8$ kPa and an inlet stagnation temperature of $T_{\mathrm{t,in}} \sim 303$ K. The turbulence intensity of the inlet flow field is raised to $T_{U,\mathrm{in}} \sim 0.04$ by the installation of a turbulence grid at the upstream inlet nozzle. The operating point assessed in this work corresponds to an overall Reynolds number of $\mathrm{Re}_{\mathrm{v1}} \sim 60.000$ and a Mach number of $\mathrm{Ma}_{\mathrm{v1}} \sim 0.65$ both being representative of LPT flow conditions.

The experimental data providing the unsteady static surface pressure distribution used for the validation of the respective numerical solution approaches are conducted by mounted fast-response pressure transducers

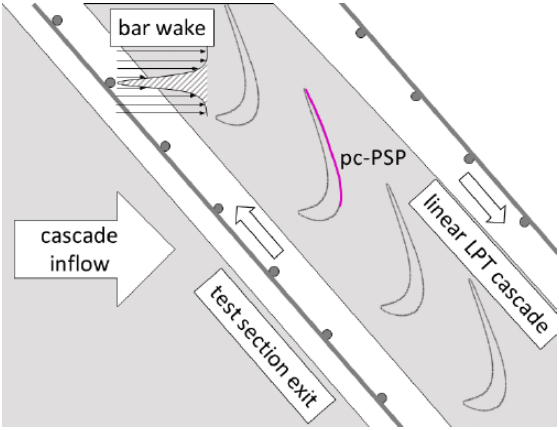

Figure 4.1.: General arrangement at the test section outlet of the considered High-speed Cascade Windtunnel [88].

of type *Kulite* LQ-062 [93]. The sensors are equally spaced over the stator vane surface at 47% relative channel height yielding a uniform pitch of ~ 12 mm. Furthermore, a trigger signal linked to the applied wake generator is recorded allowing for a synchronisation of the temporal position of the exciting wake generator bars and the pressure transducers equipped along the excited stator vane surface. All sensors are calibrated in MTU's certified calibration facility in Munich, Germany.

4.2. Evaluation Setup

In this section, a brief overview of the assessed numerical configurations is given. This includes a description of the underlying solver structures and a specification of the numerical setups for the unsteady simulations in the frequency and the time domain, respectively. The impact of turbulence is considered in accordance with Wilcox' $k-\omega$ two-equation turbulence model [68]. While the flow around the rotating wake generator is considered as fully turbulent, the transition of the boundary layer from a laminar to a turbulent state within the measured stator cascade is taken into account by

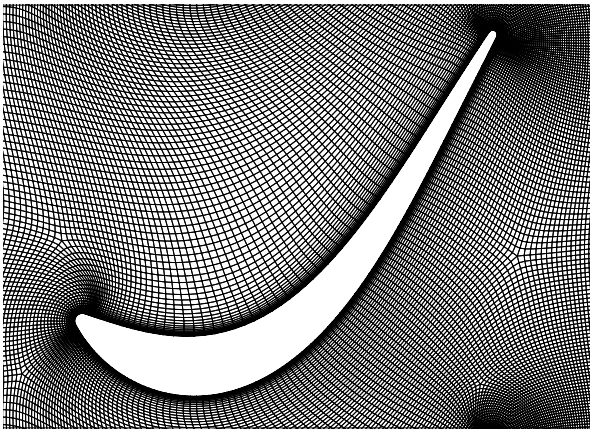

Figure 4.2.: Applied grid topology discretising the measured LPT stator geometry.

exploitation of a correlation based transition model as proposed in [18].

For the measured vane span at 47% radial channel height, the radial flow components are of negligible order providing a two-dimensional flow state. Therefore, the discretised computational domain is reduced to only 5 cells in radial direction with symmetry conditions imposed to the radial boundaries. The resulting quasi three-dimensional (Q3D) mesh consists of approximately 800 000 cells and relies on a block-structured grid topology as it is displayed, for instance, in Fig. 4.2 for the measured LPT stator cascade.

For both time and frequency domain simulations, equivalent boundary conditions are imposed. The boundary conditions are of non-reflecting type as proposed by [75] and based on a formulation in the frequency domain as described in [77]. At the inlet boundary, constant radial profiles with regard to stagnation pressure $p_{\mathrm{t,in}}$, stagnation temperature $T_{\mathrm{t,in}}$ and pitchwise flow angles according to performed inflow measurements are prescribed. Furthermore, constant inlet values for turbulence intensity T_U and length scale l_U are imposed in accordance with the turbulence grid installed at the inflow section. In order to reproduce the measured performance point, a constant static pressure level as met during the test is imposed as outlet boundary condition.

4.2.1. Setup for Unsteady Simulations in the Time Domain

The mutual communication between the adjacent domains of the rotating wake generator and the non-rotating stator vane is realised by exploiting a zonal interface as described in [85]. The simulations are performed by resolving a complete revolution of the rotating wake generator with 256 physical timesteps which enables at least 128 physical timesteps per generator bar and vane passing, respectively. The underlying time integration method is based on a backward Eulerian scheme of second order [86]. Within each physical timestep, a relaxation in pseudo-time related to an implicit Gauss-Seidel method with multiple solver sweeps is applied. In order to provide a periodic state at the end of the simulation, convergence is assessed according to [87]. The simulation is stopped after 20 complete revolutions of the rotating wake generator row whilst the final is mainly performed to record the required data over a complete wake generator revolution.

4.2.2. Setup for Harmonic Balance Simulations in the Frequency Domain

The consideration of the respective sources of unsteadiness at differing frequencies and inter blade phase angles (IBPA) is treated by employing the harmonic set approach of the applied HB solver [41]. Each unsteady interaction between the adjacent computational domains is associated to an explicit combination of a base frequency and IBPA. Since the higher harmonics of these interactions are defined as integral multiples of the respective combinations of base frequency and IBPA, they can be summarised in a so called shared harmonic set as described in [41]. The communication enabling the unsteady interaction between the adjacent domains is then realised via a transfer of the harmonic content in each considered harmonic set. The resolved harmonic sets, namely their underlying base frequencies and their associated harmonics are summarised in Tab. 4.1.

The dominant source of unsteadiness within the measured stator cascade (V1) is induced by its operation in the wake of the upstream located wake generator (WG). The harmonic content linked to the wake generator passing

Table 4.1.: Considered harmonic sets with base frequencies and number of associated harmonics.

Set	Domain	Base Frequency	# of Harmonics
HS1	V1	WGPF	0 1 2 3 4 5 6 7 8 9 10
HS2	WG	VPF_1	0 1 2 3 4

frequency (WGPF) is resolved by taking into account 10 harmonics and represented by a shared harmonic set denoted in the following as HS1. The unsteady interaction between wake generator and potential field of the downstream stator cascade at the passing frequency of V1 (VPF_1) in the rotating frame of reference is provided by HS2 by resolving 4 harmonics. All considered harmonic content is coupled with the time-averaged flow field as indicated by the zeroth harmonic entries in Tab. 4.1.

4.3. Transient Pressure Distribution

The capability to reproduce the unsteady pressure fluctuation acting on the measured stator cascade of the respective numerical solution approaches performed either in the time and the frequency domain is evaluated by a comparison with the available unsteady measurement data. Therefore, the pressure fluctuation amplitude of the respective approaches is plotted in Fig. 4.3 over the axial chord length l_{ax} at the midspan of the investigated stator cascade. The stator's pressure side is displayed from $-1 < x/l_{ax} < 0$ while the results associated to the stator's suction side are plotted in the range between $0 < x/l_{ax} < 1$. Accordingly, the stagnation point and the leading edge of the profile, respectively, is marked by $x/l_{ax} = 0$ while the profile's trailing edge is determined by $|x/l_{ax}| = 1$. In the scope of this work, the focus is on an assessment of the frequency linked to the first harmonic of the wake generator passing frequency alone.

In Fig. 4, the reference relying on the unsteady fast response measurement data is plotted with solid squared symbols while the reference results generated by the established time integration solution method are represented by a dashed line. The results of the Harmonic Balance approach taking advantage of the Lanczos-filter approach as proposed in chapter 2 while resolving turbulence effects in an unsteady fashion are displayed with a solid line. Finally, the results of an Harmonic Balance method neglecting the unsteadiness of the underlying turbulence model by consideration of its temporal average alone are added to Fig. 4.3 by a solid-dotted line. The evaluation of the differences between the respective Harmonic Balance approaches allows to judge the impact of unsteady turbulence on the excitation of the investigated stator cascade as well as it provides an indicator for the potential benefit of the respective approaches with regard to their application in an aeroelastic design framework.

Focusing on the results for the pressure side in the range from $-1 < x/l_{\mathrm{ax}} < 0$ first, a remarkable agreement for both the time integration and the Harmonic Balance method resolving unsteady turbulence compared to the available measurement data can be observed over the complete pressure side. Both methods resolving turbulence in an unsteady fashion are able to reproduce the amplitude of the pressure fluctuation induced by the upstream wake generator in both quality and quantity though differences appear increasingly in regions closer to the trailing edge. However, the prediction of the fluctuation amplitude of both the time and the frequency domain solution approach relying on Lanczos-filtered turbulence match over the complete pressure side. The Harmonic Balance approach limited to the temporal average of the underlying turbulence model shows in return a significant though rather constant offset over the profile's pressure side while still being able to reproduce the qualitative behaviour of the fluctuation amplitude very well.

For what concerns the measured suction side, again the time domain and the frequency domain approach both considering the transient behaviour of turbulence structures agree over a substantial region in between $0 < x/l_{\mathrm{ax}} < 0.75$ where the results are supported by a satisfying agreement

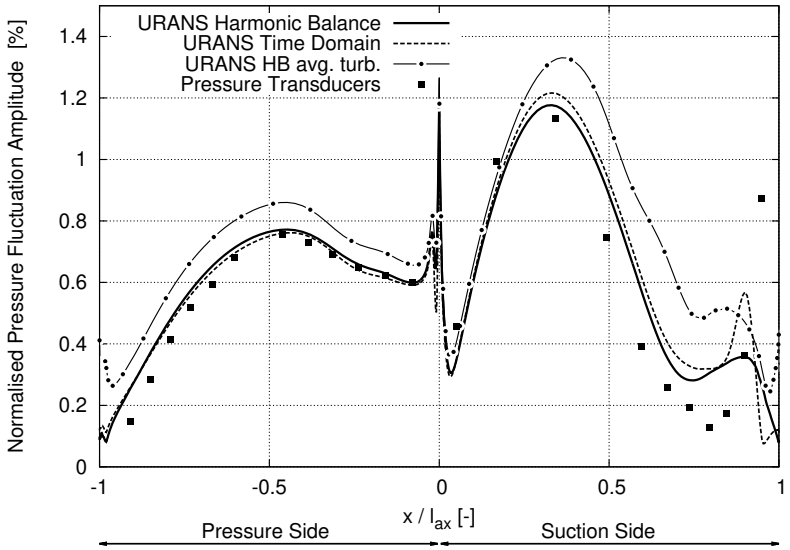

Figure 4.3.: Pressure fluctuation amplitude at WGPF along the axial chord length l_{ax} of the excited LPT cascade.

with the underlying measurement data as well. As it is the case for the pressure side, the Harmonic Balance approach neglecting the impact of unsteady turbulence overestimates the pressure fluctuation amplitude in this part of the suction side while still being able to capture the qualitative behaviour in a suitable manner. Further downstream at $x/l_{\mathrm{ax}} > 0.75$, the deviations of the assessed approaches in both quality and quantity become more apparent. While all numerical approaches overestimate the pressure fluctuation amplitude compared to the measurement data, the results generated by the time integration solver reproduce at least qualitatively the measurement by reproducing a substantial fluctuation peak towards the trailing edge in the region between $0.8 < x/l_{\mathrm{ax}} < 0.9$ as it is indicated by the measurement data. However, both decline of the pressure fluctuation amplitude in the region between $0.6 < x/l_{\mathrm{ax}} < 0.75$ as well as its subsequent rise at $0.75 < x/l_{\mathrm{ax}} < 0.95$ are underestimated by the time integration solution method.

While the tendency of a raise in the predicted pressure fluctuation amplitude can be observed for the results of both investigated Harmonic Balance methods, this behaviour is limited to a very short region in the case of neglected unsteady turbulence. Although the Harmonic Balance method capturing unsteady turbulence predicts this subsequent rise over a wider part of the stator in the region between $0.6 < x/l_{ax} < 0.9$, its peak appears to be of substantially lower order and by a much smaller gradient compared to the transient measurement data and the time domain solution, respectively.

Recalling the sufficient agreement for the pressure side and the upstream part of the suction side, this hints at a differing prediction of the transition from a laminar to a turbulent state of the underlying boundary layer. In order to judge potential differences concerning the predicted transition behaviour, the shape factor H_{12} defined as

$$H_{12} := \frac{\delta_1}{\Theta} = \begin{cases} \sim 1.8 & \text{turbulent boundary layer} \\ \sim 2.6 & \text{laminar boundary layer} \\ > 3.8 & \text{separated boundary layer} \end{cases} \tag{4.1}$$

with displacement thickness δ_1 and momentum thickness Θ is assessed for the respective solution approaches in Fig. 4.4 and Fig. 4.5. In Figs. 4.4 and 4.5, the space-time diagram of the boundary layer's shape factor H_{12} is displayed for two wake generator passings T along the suction side in the range between $0.4 < x/l_{ax} < 1$ for the time integration method and the Lanczos-filtered Harmonic Balance approach, respectively.

The results of the time integration method shown in Fig. 4.4 indicate a transition behaviour alternating between separation induced transition at freestream and bypass induced transition at wake conditions. The flow separation present at freestream condition, marked by high values of the shape factor H_{12} at $0.8 < x/l_{ax} < 0.9$, is completely suppressed in the presence of the passing wake, highlighted by very low levels of H_{12} between $0.4 < x/l_{ax} < 0.6$, leading to a subsequent reattachement due to the increased entry level of turbulence induced by the upstream located wake generator.

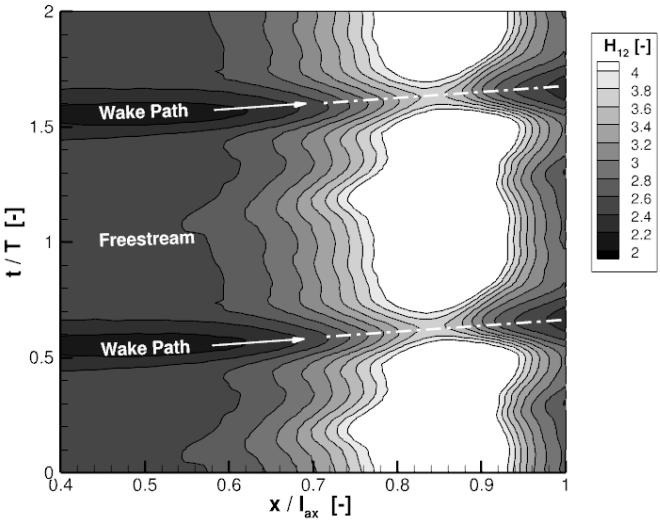

Figure 4.4.: Space-Time diagram of shape factor H_{12} predicted by the time integration method.

The equivalent results based on the results of the Harmonic Balance solver considering the unsteadiness of the applied turbulence model by taking advantage of the Lanczos-filter method are shown in Fig. 4.5. Although the presence of the flow separation is predicted reliably in general, its suppression due to the presence of the induced wake though present is not causing a complete reattachment neither does it affect a region of same order.

In fact, the significant though way underestimated increase of the pressure fluctuation amplitude between $0.7 < x/l_{\mathrm{ax}} < 0.95$ if compared to the available measurement data coincides for both solution methods with the identified region of flow separation in Fig. 4.4 and Fig. 4.5.

Accordingly, the impact of the unsteady transition behaviour dominates in the presence of a separation induced transition the excitation behaviour completely highlighting the importance of high quality transition modeling for this kind of flows. However, all applied numerical methods suffer to a certain extent from an underestimation of the separation induced excitation.

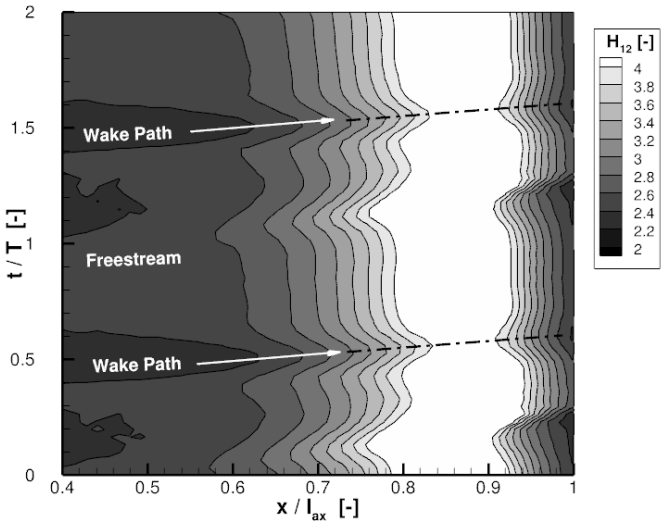

Figure 4.5.: Space-Time diagram of shape factor H_{12} predicted by the Lanczos-filtered HB method.

In terms of forced response driven excitation, the reliable prediction of the pressure fluctuation's phase relation is of same importance as the associated fluctuation amplitude. Therefore, according to the results previously discussed in Fig. 4.3, the associated pressure fluctuation phase relation is plotted in Fig. 4.6. The numerical results for both the pressure and the suction side are synchronised in accordance with the recorded trigger signal linking the start position of the wake generator relative to the respective pressure tappings within the investigated stator cascade.

As already noticed for the fluctuation amplitude, all investigated numerical approaches are able to reproduce the phase relation over vast parts of the pressure side between $-0.75 < x/l_{\mathrm{ax}} < 0$ though the HB approach neglecting unsteady turbulence indicates again a rather constant phase shift of approximately 15°. However, all predictions of the pressure fluctuation phase angle differ increasingly and substantially by proceeding further downstream towards the pressure side's trailing edge at $x/l_{\mathrm{ax}} < -0.75$.

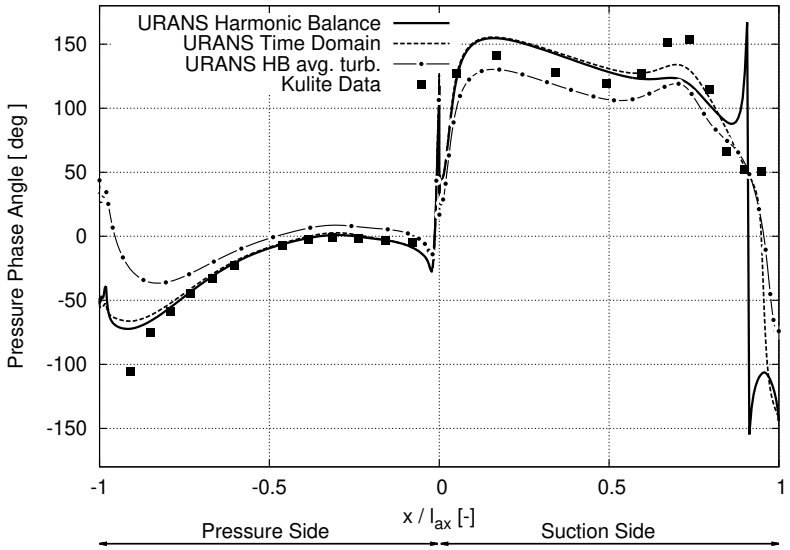

Figure 4.6.: Pressure fluctuation phase angle along the axial chord length l_{ax} of the excited LPT cascade.

Finally, the results of the fluctuation phase angle linked to the suction side of the investigated stator cascade differ quantitatively for all presented solution approaches though the qualitative behaviour is reproduced sufficiently for the front part up to $0 < x/l_{\mathrm{ax}} < 0.6$. Again, the results of the time integration and the HB method resolving the unsteady turbulence behaviour match in this region while the HB solution based on time-averaged turbulence shows an offset in an order of $\sim 30°$. Since the underlying measurement indicates values rather in between, all simulations suffer from a shift in an order of approximately 15° in this region though.

As previously stated, the rear part of the suction side at $x/l_{\mathrm{ax}} > 0.6$ is highly dependent on the presence of the separation behaviour resulting in substantial deviations in this region of the fluctuation phase angle as well. While the time integration method reproduces the best approximation of the underlying phase relation, the HB method neglecting unsteady turbulence

differs massively from the measurement whereas the HB approach considering the turbulence' unsteadiness is not able to reflect the sharp local rise and decrease in the presence of the separation sufficiently. Coming closer to the suction side's trailing edge, the agreement of the predicted phase relations with the available measurement data decreases further which makes a reliable assessment of the results difficult in this region. Large changes in both quality and quantity of the results of the conducted measurement and the simulations can be observed which indicates differences in the spatial and temporal propagation of the present separation bubble.

4.4. Conclusion

The results presented in the previous section show in general a remarkable agreement between the numerical results of all solution approaches and the reference data gained by time-resolved measurements though differences of varying order appear locally. The quality of the discussed numerical solution approaches benefiting from an increasing degree of complexity improves with the rise of resolved unsteadiness.

The simulation results generated by the Harmonic Balance approach neglecting the impact of unsteady turbulence within the flow field shows by far the largest deviations compared to the measurement data over both the pressure and the suction side. Results of substantial better agreement can be obtained by consideration of the unsteadiness within the underlying turbulence model which requires the application of a Lanczos-filter during the pursued Harmonic Balance solution procedure.

Over major parts of the measured stator cascade, this allows not only to close the gap to the time-integration method - representing the solution technique relying on the highest degree of unsteadiness and quality - but also to the available transient measurement data. Therefore, the benefit from resolving the unsteady turbulence behaviour during the Harmonic Balance solution process for what concerns the aeroelastic excitation acting on the measured stator cascade can be validated by both measurement and

numerical means.

However, in the presence of the separation bubble located at the rear part of the investigated suction side, substantial differences appear and indicate an insufficient capturing of the unsteady transition behaviour. While the results of the time-integration method in combination with its qualitative better agreement with the available measurement data indicate a transition behaviour alternating between bypass and separation induced transition modes, the results of both Harmonic Balance approaches are not able to reproduce this behaviour. Since the boundary layer of the investigated suction side is of laminar character before entering its stage of transition, this indicates that the differing treatment of turbulence within the presented Harmonic Balance approaches expresses itself rather in an improved prediction of the exciting wake generator and the transport of its induced wake into the downstream stator cascade passage.

Therefore, the main benefit of considering turbulence in an unsteady fashion results from an improved prediction of the stator cascade's excitation rather than from a superior prediction of the transient behaviour within the underlying boundary layer. At this stage, it is important to note that this observation must not be generalised and can differ for different flow situations and aeroelastic excitation mechanisms.

Nevertheless, this finally raises the question about the Harmonic Balance method's capability to predict the unsteady transition behaviour and to what extent it is affected by the application of the assessed Lanczos-filter approach. In the previous chapter 3, the general capability to predict the unsteady transition if the Lanczos-filter method proposed in chapter 2 is applied has been investigated by comparing time-resolved measurement data conducted by surface thin film gauges within a boundary layer of a 2-stage LPT test facility. The results presented in chapter 3 support the Harmonic Balance' general capability to reflect the unsteady transition behaviour while taking advantage of the Lanczos-filter approach if applied to transport equations linked to turbulence modeling.

However, in contrast to the pure correlation-based transition model [18] applied in this chapter, transition is modeled in chapter 3 by relying on the

solution of two additional transport equations for the intermittency γ and the transition Reynolds number Re_{Θ_t} as it is usually done in the context of Menter's $\gamma - \mathrm{Re}_{\Theta_t}$ framework [20, 21]. It is neither new nor surprising that a hybrid frequency-time domain approach as the applied Harmonic Balance method suffers in particular if transition modeling is considered based on pure correlation alone since its treatment in the frequency domain in an equivalent fashion turns out to be difficult. In fact, the limitation of its application in a frequency domain approach remains to be one of the few constraints to its application. However, since the transition model based on [18] turns out to be the only one being able to predict the presence of the separation bubble, whose presence is supported by the transient measurement data as well, a separated discussion of the differences induced by the application of the Lanczos-filter method and by the differing treatment of the underlying transition model is not possible in this chapter.

Furthermore, the results presented in the previous section stress the need of a reliable prediction of the transient behaviour of the flow separation in the presence of a passing wake and its impact on the pressure fluctuation acting on the investigated stator cascade and therefore on its aeroelastic excitation. Even the time-integration solution method resolving the highest degree of unsteadiness is not completely capable to predict the unsteady pressure fluctuation in the presence of the separation bubble as the available measurement data indicate its impact to be even more distinct and to be located further downstream. Therefore, in order to improve the quality of the numerical predictions discussed in this chapter, it is mandatory to consider the transient transition behaviour in a more reliable fashion than it is possible at this stage. Keeping in mind the remaining differences between the results of the respective solution approaches and the time-resolved measurement data, the deviations induced by referring to the assessed Lanczos-filtered Harmonic Balance solver are, however, not of higher order than the deviations to the measurement data in general.

Chapter 5

Impact of Unsteady Turbulence Effects on the Forced Response Excitation

In the previous chapters, the stability problems of the investigated Harmonic Balance method are discussed and a solution to overcome this problem is formulated. In this context, the undesired impact of Gibbs phenomenon on the treatment of turbulence is identified to be a key challenge and the application of an appropriate Lanczos-filter method on the variables linked to the underlying turbulence model is proposed to overcome this problem. Furthermore, the feasibility of the proposed filter method if applied to turbulence variables is demonstrated by a validation against time-resolved measurement data providing insight into the time-dependent behaviour of boundary layers and pressure fluctuations acting on LPT stator surfaces.

In the following chapter, the Harmonic Balance method enhanced by an increased level of robustness is applied to predict the forced response excitation behaviour under subsonic and transonic flow conditions. Both subsonic and transonic flow situations investigated in the following require the application of the proposed Lanczos-filter method in order to provide stable and converged solutions by the assessed Harmonic Balance method if turbulence is treated in an unsteady fashion. The impact as well as the benefit of taking into account the unsteadiness within the applied turbulence models is discussed and quantified.

5.1. Subsonic Forced Response Excitation

The focus of this section is on an assessment of the impact of unsteady turbulence effects and the application of the filter method proposed in section 2.4 on the prediction of the forced response behaviour of a modern LPT-configuration. This is achieved by an evaluation of the prediction of the unsteady surface pressure distribution as well as the associated generalised force by numerical means. Therefore, simulations being representative of a subsonic in-flight performance-point have been performed while referring to different solution approaches.

The investigated LPT-model consists of the first 1.5 stages with a vane count of 14/70/56 blades for the first vane (V1), blade (B1) and the second vane (V2), respectively. The impact of turbulence is considered by taking advantage of Wilcox' k-ω turbulence model [68] in combination with Menter's two-equation transition model [21] in order to capture the transition from a laminar to a turbulent state properly. All three considered blade rows are discretised by structured multiblock meshes with an average dimensionless wall distance of $y^+ < 1$. The inlet of the considered numerical model is located at $\sim 45\%$ of the first stator chord length upstream of its leading edge whilst the outlet position is located at $\sim 45\%$ of the second stator's chord length downstream of its trailing edge.

5.1.1. Harmonic Balance Setup

For the simulations based on the HB approach, a single passage mesh with periodic boundaries in the pitchwise direction is employed for the considered 1.5 stage LPT configuration. The applied mesh consists of approximately 7 million grid points and is realised by relying on a block structured meshing approach. A slice in the mid-span region of the resulting mesh is shown in Fig. 5.1. At both inlet and outlet, non-reflecting boundary conditions relying on a formulation in the frequency domain based on [75, 76, 94] are applied in order to determine the associated performance point. The setup of considered base frequencies and their higher harmonics is shown

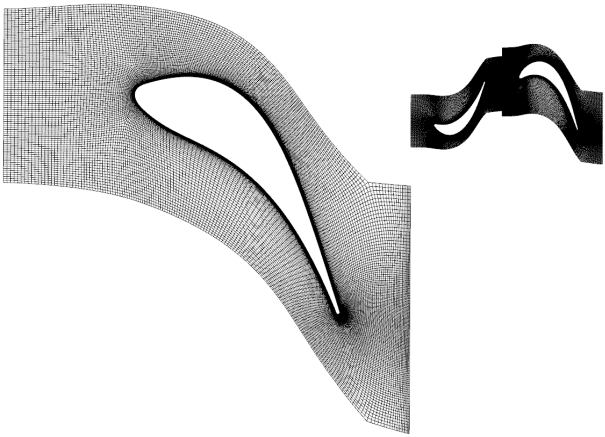

Figure 5.1.: SINGLE PASSAGE MESH OF THE INVESTIGATED LPT CONFIGURATION FOR THE PERFORMED HB SIMULATIONS [63].

in Tab. 5.1 where BPF_i and VPF_i denote the blade/vane passing frequency of the i-th rotor and stator, respectively. The unsteadiness in the first rotor resulting from VPF_1 and VPF_2 is considered by taking into account the first 8 harmonics of the associated base frequencies. The communication between the computational domains of the respective blade rows is realised by exploiting an interface approach allowing for an exchange of the unsteady information in the considered base frequencies and their higher harmonics.

5.1.2. Time-Integration Setup

In contrast to the HB setup described above, the communication between the respective blade rows is realised here via zonal interfaces [85] requiring identical pitch sections up- and downstream of the interfaces. Consequently, multiple passages have to be considered in the mesh of the first rotor blade row and the second stator vane row providing a configuration consisting of five rotor 1 blades and of four stator 2 vanes. The total mesh for the unsteady time domain calculations consists of approximately 22 million grid points and is shown for the mid-span plane in Fig. 5.2.

Table 5.1.: CONSIDERED BASE FREQUENCIES AND NUMBER OF ASSOCIATED HARMONICS FOR THE 1.5 STAGE LPT-MODEL.

Blade Row	Base Frequency	# Harmonics
Vane 1 (V1)	BPF_1	0 1 2
Blade 1 (B1)	VPF_1	0 1 2 3 4 5 6 7 8
Blade 1 (B1)	VPF_2	0 1 2 3 4 5 6 7 8
Vane 2 (V2)	BPF_1	0 1 2 3 4 5 6 7 8
Vane 2 (V2)	0 (clocking mode V1)	0 1 2 3

For both inlet and outlet, boundary conditions equivalent to the frequency domain solver are chosen [76]. Since the prescribed non-reflecting boundary conditions are formulated in the frequency domain, additional transformations between time and frequency domain are necessary during the solution process in the time domain. Since the focus of this work is to evaluate the aeroelastic behaviour of the rotor blade only and since this rotor blade is sufficiently far away from both inlet and outlet, the slight differences in the prescribed boundary conditions are not affecting the unsteady pressure distributions investigated in this work. The simulations are performed by resolving the first stator passing period with 288 physical timesteps. 16 stator 1 periods are considered during the simulation. In order to provide a sufficiently converged state at the end of the simulation, convergence is assessed according to [87].

5.1.3. Impact of the Lanczos-Filter on the Unsteady Solution Behaviour

After having shown the capability of the realised Lanczos-filter to overcome undesired oscillations caused by the Gibbs phenomenon in section 2.4, the impact of its application on the aeroelastic behaviour of the considered LPT-configuration is discussed in the following. Therefore, a stable solution from the HB solver based on conventional, unfiltered IFT is generated for the considered performance point even if the unsteadiness in the underlying turbulence quantities is considered.

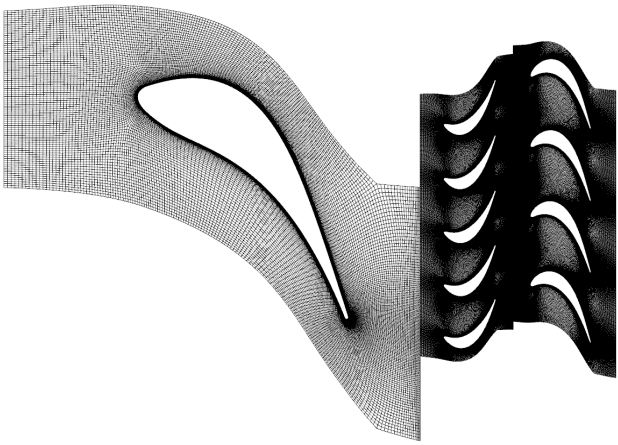

Figure 5.2.: MULTI-PASSAGE MESH OF THE INVESTIGATED LPT CONFIGURATION FOR THE UNSTEADY SIMULATIONS PERFORMED IN THE TIME DOMAIN [63].

In this case, this can be achieved by decreasing the present CFL-number and increasing the number of considered harmonics at a tremendous expense of computational time and by consideration of conditions being representative of an aerodynamic design point. Since in aeroelasticity the performance points of interest can be far away from the convenient conditions in the design point considered here, relying on the conventional IFT can prove to be arbitrarily difficult and expensive.

In order to determine the impact of the applied filter method on the unsteady pressure distributions on the blade surfaces of interest, the generated pressure distributions based on conventional IFT are compared to the Lanczos-filtered IFT approach described in Fig. 2.3. From an aeroelastic point of view, the pressure fluctuation associated to the first harmonic of the VPF_1 - the engine order (EO) linked to the first vane (V1), that is - acting on the blade 1 (B1) surface is of major interest in this case. Both amplitude and phase of the pressure fluctuation in the first harmonic of the V1-EO are calculated for both IFT approaches by taking advantage of the HB method

provided by the flow solver TRACE. In a subsequent step, the differences in the resulting fluctuation amplitudes $\delta_{p'}$ are calculated in a non-dimensional fashion according to

$$\delta_{p'} := \frac{p'_{\mathrm{IFT}} - p'_{\sigma_m}}{p'_{\mathrm{IFT}}} \quad . \tag{5.1}$$

Here, p'_{σ_m} refers to the pressure fluctuation amplitude obtained from the Lanczos-filtered approach while p'_{IFT} refers to the fluctuation amplitude based on the conventional IFT.

The results are displayed in Fig. 5.3 where the left hand side is linked to the suction side and the right hand side is linked to the pressure side, respectively. The trailing edge is headed to the middle of Fig. 5.3 indicated by its abbreviation TE while the location of the leading edges is marked by its abbreviation LE.

Though Fig. 5.3 indicates the mean deviation $\overline{\delta}_{p'}$ over the investigated blade surface to appear in an order of lower than $\overline{\delta}_{p'} < 5\%$, this level is exceeded substantially in specific regions of the blade. This can be observed in particular at the aft regions of the blade on the suction side where the local fluctuation amplitudes p' get close to zero and $\delta_{p'}$ increases up to 20%.

In contrast to its appearance at the suction side, the deviation $\delta_{p'}$ turns out to be in the same order as suggested by the mean difference $\overline{\delta}_{p'}$ over the major part of the blade's pressure side. Exceeding deviations in an order of up to 10% can be observed only locally close to the pressure side's leading edge.

The differences δ_Φ of the associated pressure fluctuation phase angle Φ between the solution based on either the conventional or the filtered solution approach are given by

$$\delta_\Phi := \Phi_{\mathrm{IFT}} - \Phi_{\sigma_m} \tag{5.2}$$

and shown in Fig. 5.4 for the suction side on the left and for the pressure side on the right hand side. As in Fig. 5.3, the largest deviations between the

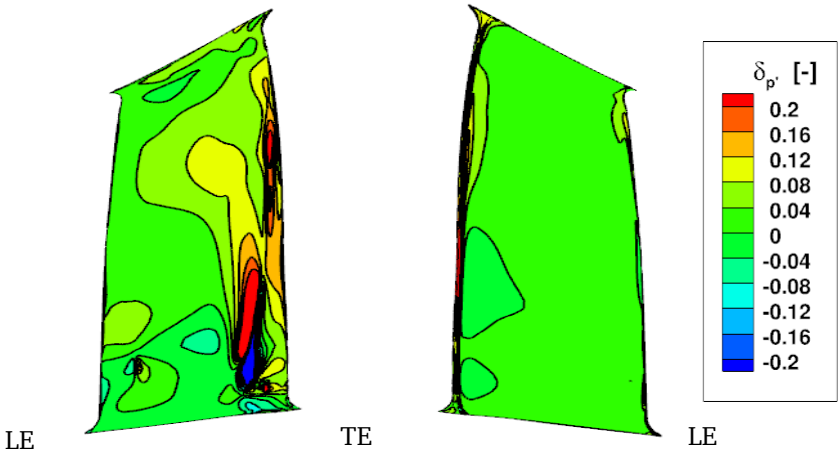

Figure 5.3.: DIFFERENCES OF THE PRESSURE FLUCTUATION AMPLITUDE APPEARING AT THE FIRST HARMONIC OF VPF_1 (SS LEFT, PS RIGHT) [63].

filtered and the conventional IFT-approach can be noticed at the rear parts of the suction side where the boundary layer is facing pressure gradients acting against the main flow direction. The mean deviation of the fluctuation phase angle $\overline{\delta}_\Phi$ over the entire blade surface is approximately $\overline{\delta}_\Phi \sim 0.006$ rad which is equivalent to $\overline{\delta}_\Phi \sim 0.34°$. Again, the deviations observed over the pressure side of the rotor blade are of same order as the mean value over the whole blade surface.

The impact of the local deviations in both amplitude and phase of the considered pressure fluctuations on the global aeroelastic behaviour of the rotor blade can be estimated by referring to an integral measure such as the generalised force F_g acting on the blade. The difference in the generalised force of the filtered approach F_{g,σ_m} and the unfiltered IFT $F_{g,\mathrm{IFT}}$ is given by

$$\delta_{F_g} := \frac{F_{g,\mathrm{IFT}} - F_{g,\sigma_m}}{F_{g,\mathrm{IFT}}} = 0.025 \quad . \tag{5.3}$$

The resulting deviation appears in an order of 2.5% and indicates only small

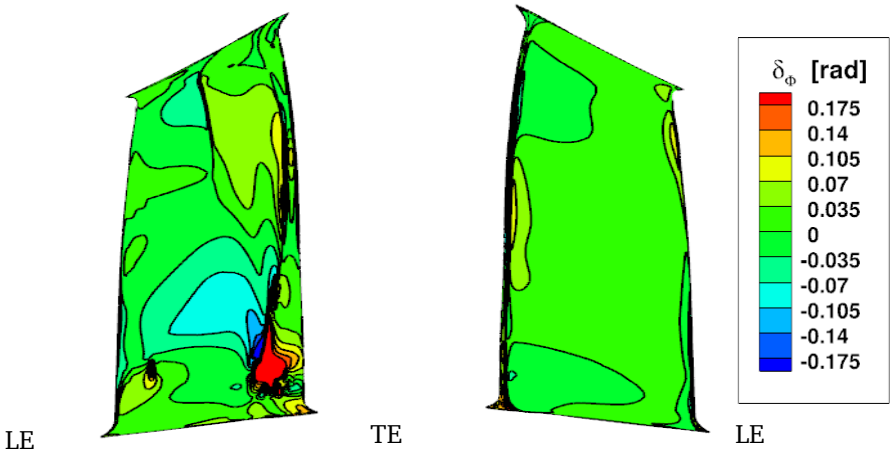

Figure 5.4.: DIFFERENCES OF THE PRESSURE FLUCTUATION PHASE ANGLE AT FIRST HARMONIC OF VPF_1 (SS LEFT, PS RIGHT) [63].

variations induced by the application of the Lanczos-filtered IFT algorithm for what concerns the generalised force F_g. In addition to the results of the underlying unsteady surface pressure distributions shown in Figs. 5.3 and 5.4, the realised filter method is not considered to affect the aeroelastic evaluation process in a critical order since the leading error is not amplified in an unfeasible fashion.

5.1.4. Impact of Unsteady Turbulence on the Aerodynamic Excitation Behaviour at Subsonic Flow Conditions

In the subsequent section, the impact of the unsteadiness within the employed turbulence models on the aeroelastic behaviour of the considered LPT rotor blade is evaluated for the same conditions being representative of an in-flight performance point. Unsteady simulations of the LPT configuration described above are performed in both the frequency and the time domain relying on differing degrees of resolved unsteadiness with regard to the applied turbulence model. In order to estimate the impact of the fluctuating

part of the turbulence quantities, two simulations in the frequency domain are performed.

The first simulation refers to a conventional HB approach considering only the time-average of the turbulence quantities. The second simulation is based on the HB approach resolving the unsteadiness within the applied turbulence model by taking into account the harmonic content of k and ω, as well as of γ and $\mathrm{Re}_{\theta,t}$. For lots of aeroelastic performance points of interest, a robust solution can only be obtained by accepting disproportional numerical efforts if conventional IFT is applied. Hence, the realised Lanczos-filter method described in the previous section is employed if the unsteady turbulence behaviour is considered in the frequency domain simulations.

In addition to the calculations in the frequency domain, a third simulation relying on a non-linear solution process in the time domain is performed including all unsteady effects in both URANS and turbulence equations beyond the considered frequencies in the performed HB simulations. Since this time-integration method contains all unsteady information, it is treated in the context of this section as a benchmark for the respective HB approaches. In order to illustrate the differing treatment of the turbulence quantities during the respective solution approaches, the distribution of the eddy viscosity ratio Ψ_t between the eddy viscosity μ_t and the dynamic viscosity μ_{ref}

$$\Psi_t := \frac{\mu_t}{\mu_{\mathrm{ref}}} \tag{5.4}$$

is compared in Figs. 5.5 - 5.7. The distribution of the eddy viscosity ratio Ψ_t obtained from the complete URANS benchmark is shown in Fig. 5.5 for the midspan plane. The dominant wake of the first stator is convected through the downstream blade rows and shows a satisfying transport over the applied zonal interfaces. The corresponding result obtained from the HB simulation resolving the unsteadiness of the turbulence quantities by exploiting the introduced Lanczos-filter method is shown in Fig. 5.6. Due to the limited number of considered harmonics, the eddy viscosity ratio Ψ_t in the peak of the wake is underestimated. Furthermore, the wake is predicted to be wider compared to the complete URANS simulation as previously indicated by Fig.

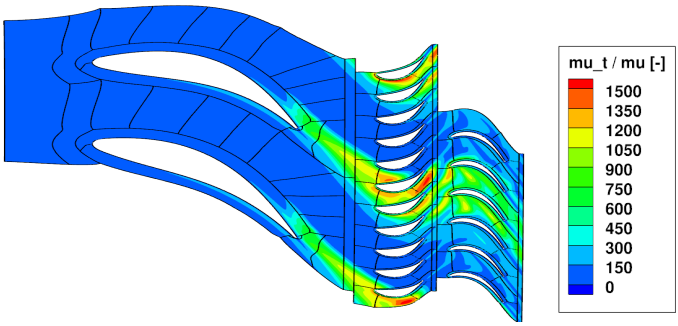

Figure 5.5.: AXIAL PROPAGATION OF THE EDDY VISCOSITY RATIO Ψ_t BASED ON THE TIME-INTEGRATION BENCHMARK [63].

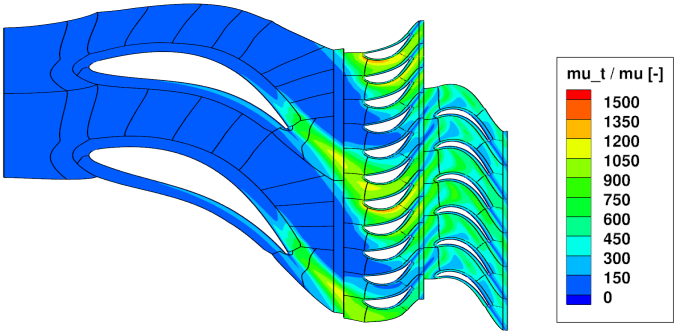

Figure 5.6.: AXIAL PROPAGATION OF THE EDDY VISCOSITY RATIO Ψ_t BASED ON THE LANCZOS-FILTERED HB APPROACH [63].

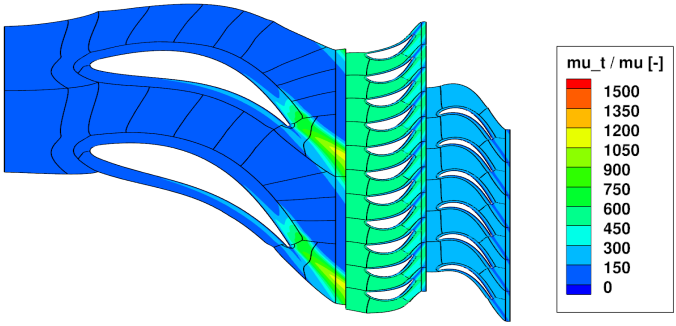

Figure 5.7.: AXIAL PROPAGATION OF THE EDDY VISCOSITY RATIO Ψ_t BASED ON TIME-AVERAGED TURBULENCE [63].

2.4. As a consequence, the eddy viscosity differs significantly in the second stator row from the result of the time domain benchmark since the thicker wake is mixed out differently during its propagation through the first rotor passage.

The limitations of the HB simulation neglecting the unsteady effects in the applied turbulence model become obvious by comparing the treatment of the eddy viscosity shown in Fig. 5.7. Since no harmonics are taken into account in order to resolve the time dependent behaviour of the turbulence quantities, the eddy viscosity is based on averaged quantities only in the downstream rows. Therefore, relying on the proposed Lanczos-filter method is from a physical point of view an attractive alternative to include transient effects in the underlying turbulence models in a robust fashion.

In order to evaluate the impact of neglecting the unsteady turbulence effects during the solution process in the frequency domain, the resulting unsteady pressure distributions and the associated generalised force acting on the considered rotor blade row are investigated in the following. Equivalent to eq. (5.1), the differences

$$\delta_{p',\overline{\mu}_t} := \frac{p'_{\mathrm{URANS}} - p'_{\overline{\mu}_t}}{p'_{\mathrm{URANS,avg.}}} \tag{5.5}$$

between the pressure fluctuation amplitude p'_{URANS} based on the complete URANS-benchmark and the pressure amplitude $p'_{\overline{\mu}_t}$ obtained from the HB approach neglecting unsteady turbulence - both normalised by the mean amplitude of the time-integration method - $p'_{\mathrm{URANS,avg.}}$ are shown in Fig. 5.8.

For both the suction (left) and the pressure side (right) the first harmonic of the VPF_1 is investigated. Analysis of the suction side on the left hand side of Fig. 5.8 reveals major differences in the pressure fluctuation in an order of up to 15% over vast regions of the blade. In particular, the rear and middle parts of the blade show large deviations and indicate a differing behaviour of the fluctuation amplitude in both quality and quantity indicated by the changes in the sign of $\delta_{p',\overline{\mu}_t}$.

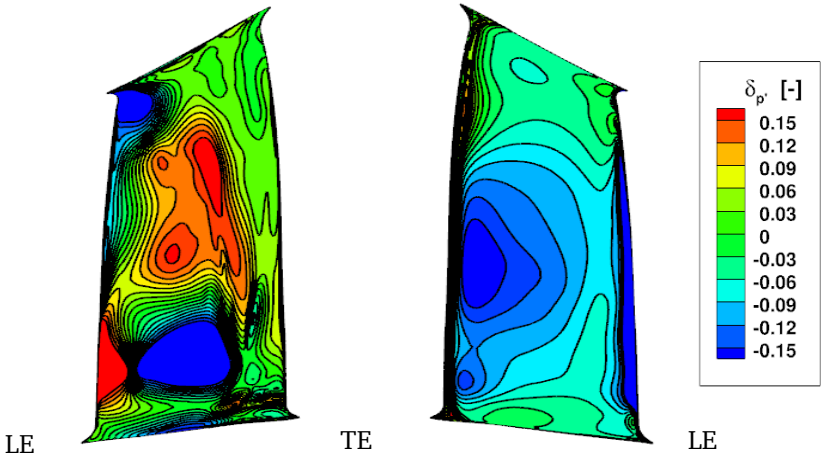

Figure 5.8.: DIFFERENCES OF THE PRESSURE FLUCTUATION AMPLITUDE BETWEEN HB APPROACH NEGLECTING UNSTEADY TURBULENCE AND TIME-DOMAIN BENCHMARK (SS LEFT, PS RIGHT) [63].

In contrast to this, the difference of the fluctuation amplitude $\delta_{p',\overline{\mu}_t}$ on the pressure side - as shown on the right hand side of Fig. 5.8 - shows no changes in the sign over the main part of the blade though major differences over large regions in the same order can be noticed. In particular, the rear mid-span region and regions close to the leading edge of the considered rotor blade show the largest differences between the compared time domain simulation and the HB simulation neglecting the unsteadiness in the applied turbulence model. The deviation

$$\delta_{p',\sigma_m} := \frac{p'_{\text{URANS}} - p'_{\sigma_m}}{p'_{\text{URANS,avg.}}} \tag{5.6}$$

between the pressure fluctuation amplitude p'_{URANS} of the complete URANS-simulation and the associated result of the surface pressure amplitude p'_{σ_m} obtained from the Lanczos-filtered HB approach resolving the unsteadiness in the turbulence quantities is shown in an analogous fashion in Fig. 5.9.

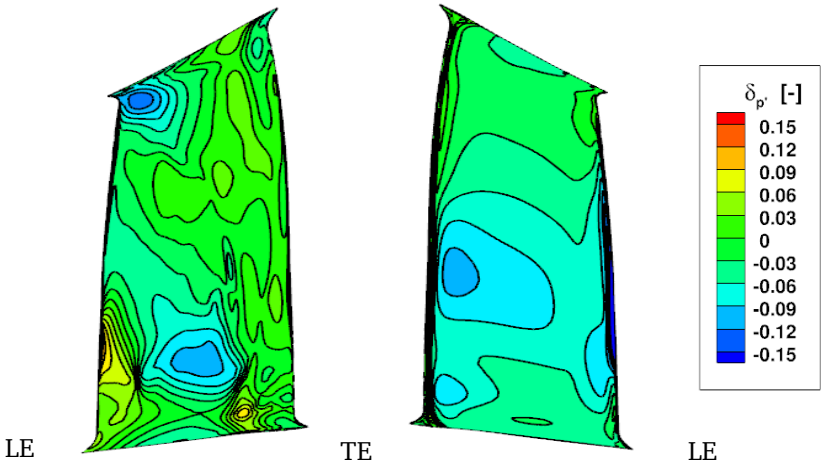

Figure 5.9.: DIFFERENCES OF THE PRESSURE FLUCTUATION AMPLITUDE BETWEEN LANCZOS-FILTERED HB APPROACH AND TIME-DOMAIN BENCHMARK (SS LEFT, PS RIGHT) [63].

Comparing the results from Fig. 5.8 and Fig. 5.9, the deviations with regard to the fluctuation amplitude obtained by consideration of unsteady turbulence in the frequency domain show better agreement with the time domain benchmark in both quality and quantity over large parts of the blade surface. In particular, the regions with major differences in Fig. 5.8 correspond much better in the case of included unsteady turbulence with the URANS benchmark. On both suction and pressure side, the deviations do not exceed an order of 10%. Nevertheless, the behaviour of the fluctuation amplitude still differs compared to the URANS-simulation, in particular on the pressure side though rather locally on the suction side of the blade.

This is confirmed by an evaluation of the pressure fluctuation along the axial chord length l_{ax} of the investigated blade surface at 67% span as shown in Fig. 5.10. In Fig. 5.10, the pressure fluctuation amplitude $p'/p_{t,\mathrm{in}}$ normalised by the inlet total pressure $p_{t,\mathrm{in}}$ is plotted over the relative axial chord length x/l_{ax}. In this context, the solid-dotted line in Fig. 5.10 represents the fluctuation amplitude obtained from the HB approach neglecting un-

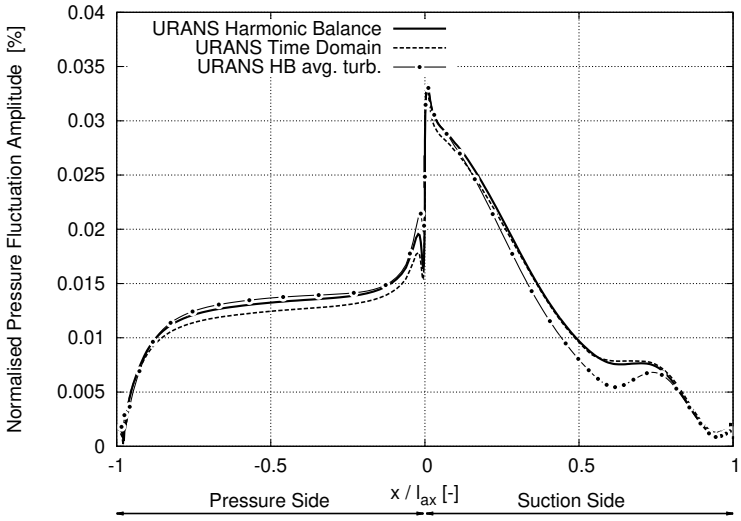

Figure 5.10.: AMPLITUDE OF THE SURFACE PRESSURE FLUCTUATION AT FIRST HARMONIC OF VPF_1 AT 67% SPAN OF B1 [63].

steady turbulence, whereas the HB simulation considering turbulence in an unsteady fashion refers to the solid line and the complete URANS solution to the dashed line, respectively.

Focusing on the suction side plotted in Fig. 5.10 in the range of $x/l_{ax} > 0$, a remarkable agreement between solutions obtained from complete URANS and HB relying on unsteady turbulence can be noticed. Compared to this, the HB approach neglecting the unsteadiness in the applied turbulence model shows differences in both quality and quantity, in particular in the region between $0.25 < x/l_{ax} < 0.75$.

Recalling the results of the pressure side plotted in Fig. 5.10 in the range of $x/l_{ax} < 0$, all solutions show a similar behaviour. However, a constant shift in the fluctuation amplitude obtained from the complete URANS solution can be noticed between $-0.8 < x/l_{ax} < 0$. In the rear part of the pressure side, all results match in a satisfying manner.

From an aeroelastic point of view, the reliable prediction of the associated

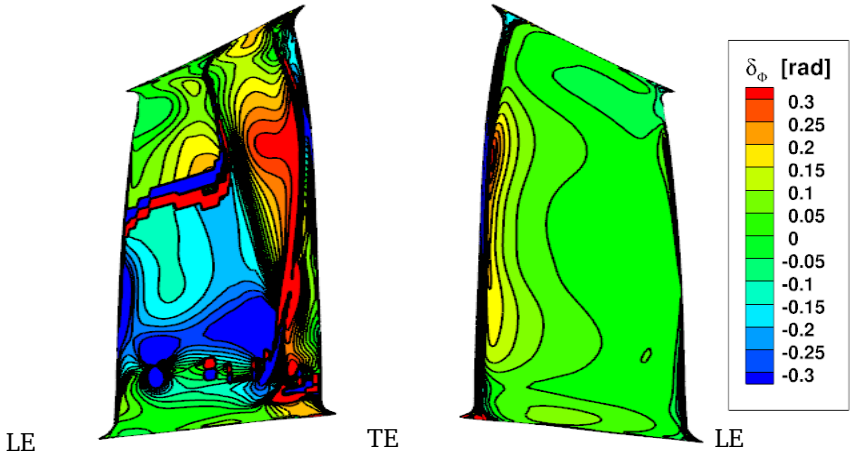

Figure 5.11.: DEVIATION OF THE PRESSURE FLUCTUATION PHASE RELATION BETWEEN HB APPROACH BASED ON AVERAGED TURBULENCE AND TIME-DOMAIN BENCHMARK (SS LEFT, PS RIGHT) [63].

phase angle Φ is of same importance as the exciting pressure amplitude itself. Therefore, the distribution of the associated phase angle Φ is discussed in the following in an analogous fashion in the Figs. 5.11-5.13. According to

$$\delta_{\Phi,\overline{\mu}_t} := \left(\Phi_{\text{URANS}} - \Phi_{\overline{\mu}_t}\right) \tag{5.7}$$

the deviation $\delta_{\Phi,\overline{\mu}_t}$ between the phase relation predicted by the time-integration reference Φ_{URANS} and the HB approach $\Phi_{\overline{\mu}_t}$ solving for the temporal average of turbulence only is shown in Fig. 5.11. Again, the focus is on the pressure fluctuation appearing at the VPF_1 induced by the first stator row.

Major differences in the phase angle Φ can be observed in large regions of the suction side on the left as well as in the rear part of the blade on the pressure side on the right hand side of Fig. 5.11. This confirms the statements previously made in the context of the discussion of the fluctuation amplitude. The deviations are in an order of up to 0.3 rad being equivalent to a shift

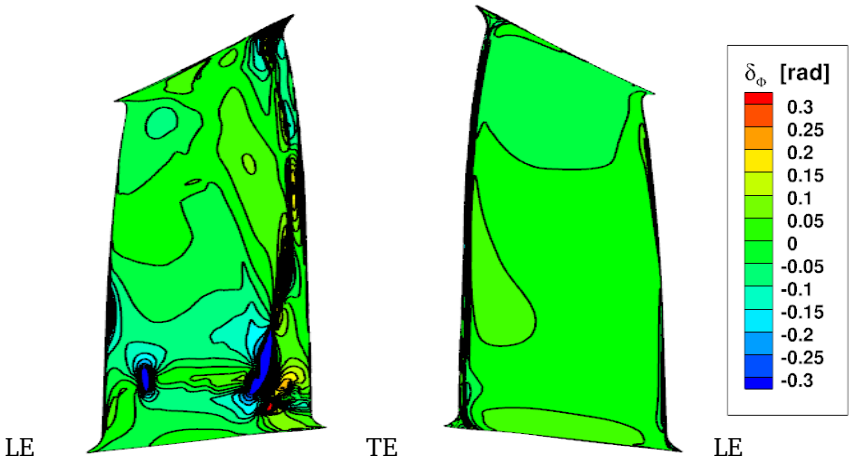

Figure 5.12.: DEVIATION OF THE PRESSURE FLUCTUATION PHASE RELATION BETWEEN LANCZOS-FILTERED HB APPROACH AND TIME-DOMAIN BENCHMARK (SS LEFT, PS RIGHT) [63].

in the phase angle Φ of approximately 18°. Again, several changes in the sign of the phase angle's deviation $\delta_{\Phi,\overline{\mu}_t}$ can be noticed in Fig. 5.11 on the suction side indicating a differing behaviour of the associated phase angle Φ.

Compared to this, the equivalent deviation in the phase angle relation

$$\delta_{\Phi,\sigma_m} := \left(\Phi_{\text{URANS}} - \Phi_{\sigma_m}\right) \tag{5.8}$$

between the URANS benchmark in the time domain Φ_{URANS} and the HB simulation resolving unsteady turbulence effects Φ_{σ_m} is displayed in Fig. 5.12. For both the suction and the pressure side, the phase angle distributions relying on unsteady turbulence show significant better agreement since major differences can be observed only locally.

In regions with rather large differences in Fig. 5.11, the phase angle relation predicted by the HB method based on the consideration of unsteady turbulence shows substantially lower deviations compared to the complete URANS benchmark. Since the changes in the sign of the deviations δ_{Φ,σ_m} are

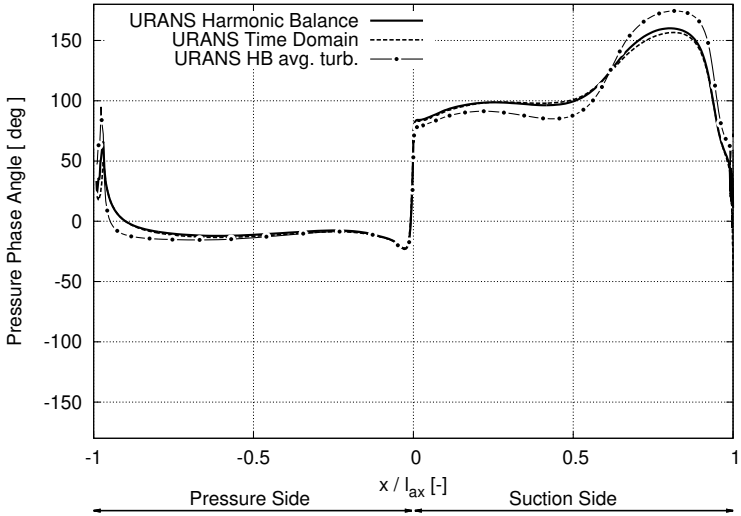

Figure 5.13.: PHASE RELATION OF THE SURFACE PRESSURE FLUCTUATION AT THE FIRST HARMONIC OF VPF_1 AT 67% SPAN [63].

only of local character, the frequency domain solver referring to unsteady turbulence is able to reproduce the phase distribution of the time domain benchmark over almost all parts of both pressure and suction side in a satisfying manner.

This is also supported by the one-dimensional analysis of the pressure phase angle Φ along the relative axial chord length l_{ax} at 67% span as displayed in Fig. 5.13. The solutions taking into account the unsteady behaviour of the employed turbulence models, represented in Fig. 5.13 by the solid line for the frequency domain approach and the dashed line for the time-integration benchmark, match over the whole chord length on both the suction and the pressure side.

In contrast to this, the phase angle predicted by the frequency domain solver neglecting unteady turbulence effects - displayed in Fig. 5.13 by a solid-dotted line - shows major differences compared to the time-integration reference, in particular along the suction side at $x/l_{ax} > 0$ and the rear part

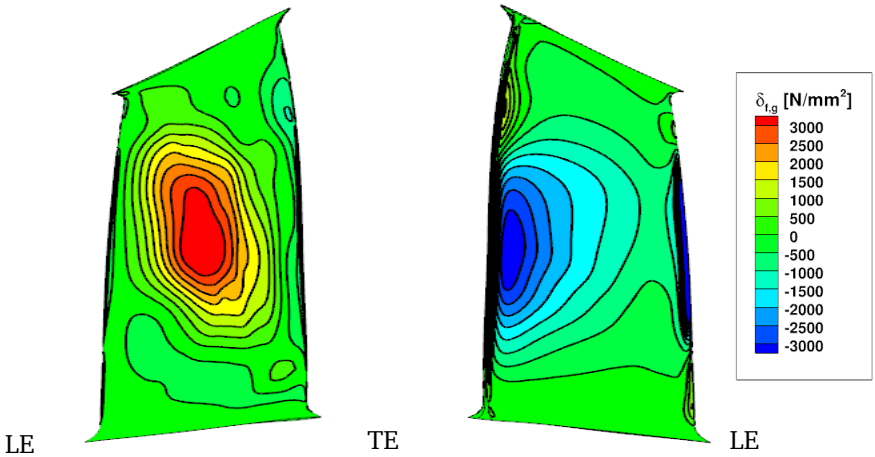

Figure 5.14.: DEVIATION OF THE LOCAL GENERALISED FORCE BETWEEN HB APPROACH NEGLECTING UNSTEADY TURBULENCE AND TIME-DOMAIN BENCHMARK (SS LEFT, PS RIGHT) [63].

of the pressure side at $x/l_{\mathrm{ax}} < -0.75$. Since the differences observed for the phase angle Φ are in an order of up to 20 degree, the differences are not of negligible order and can result in a differing aeroelastic behaviour with regard to both the aerodynamic excitation and the resulting generalised force.

In order to evaluate the impact of the differences in the unsteady pressure distributions on the aeroelastic behaviour of the blade, the deviation between the distributions of the specific, local generalised force f_g according to

$$\delta_{f_g,\overline{\mu}_t} := \left(f_{g,\mathrm{URANS}} - f_{g,\overline{\mu}_t}\right) \tag{5.9}$$

$$\delta_{f_g,\sigma_m} := \left(f_{g,\mathrm{URANS}} - f_{g,\sigma_m}\right) \tag{5.10}$$

are evaluated in Fig. 5.14 for the HB approach neglecting the impact of unsteady turbulence as well as in Fig. 5.15 for the filtered HB method resolving the unsteadiness in the employed turbulence models.

Comparing the deviation of the resulting local generalised force δ_{f_g} be-

tween the time domain benchmark and the respective HB simulations, the impact of neglecting unsteady turbulence effects on the aeroelastic excitation of the blade becomes obvious. Compared to the deviations of the generalised force $\delta_{f_g,\overline{\mu}_t}$ in Fig. 5.14 generated by neglecting unsteady turbulence effects, the differences δ_{f_g,σ_m} plotted in Fig. 5.15 obtained from the simulation considering unsteady turbulence show a behaviour substantially closer to the generalised force of the URANS reference provided in the time domain.

The differences for what concerns the local generalised force noticed for the suction side on the left hand side of Fig. 5.14 can not be observed in the results considering unsteady turbulence effects. Regarding the pressure side shown on the right hand side of Figs. 5.14 and 5.15, the deviations identified in the rear part of the blade and close to the blade's leading edge appear of substantially lower order if the unsteadiness within the underlying turbulence models is taken into account. This can be confirmed by a global analysis of the generalised force F_g according to eqs. (5.11) and (5.12)

$$\delta_{F_g,\overline{\mu}_t} := \frac{\left(F_{g,\mathrm{URANS}} - F_{g,\overline{\mu}_t}\right)}{F_{g,\mathrm{URANS}}} = 0.155 \tag{5.11}$$

$$\delta_{F_g,\sigma_m} := \frac{\left(F_{g,\mathrm{URANS}} - F_{g,\sigma_m}\right)}{F_{g,\mathrm{URANS}}} = 0.06 \tag{5.12}$$

yielding a deviation of the global generalised force F_g in an order of 15.5% if the impact of unsteady turbulence effects is neglected. By consideration of the unsteadiness within the underlying turbulence model by taking advantage of the proposed Lanczos-filter method, the deviation of the predicted generalised force F_g can be reduced in an order of ∼10 % to $\delta_{F_g,\sigma_m} = 0.06$.

However, a fair assessement of the discussed solution approaches requires a discussion of the deviations in relation to the required numerical effort. Therefore, the numerical resources consumed by the respective simulations with regard to requested CPU hours (CPUh) are summarised in Tab. 5.2. Obviously, the benchmark solution performed by the time-integration method relying on the expanded mesh size provides the by far most expansive alternative though it is considered to deliver results of highest quality.

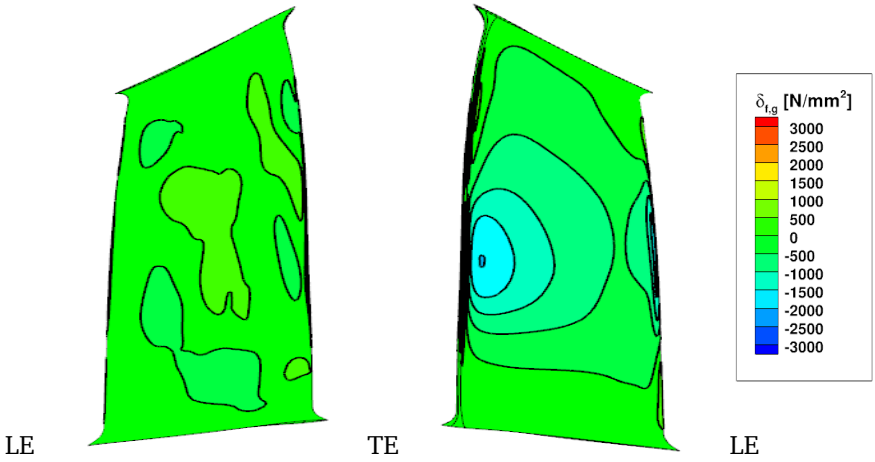

Figure 5.15.: DEVIATION OF THE LOCAL GENERALISED FORCE BETWEEN LANCZOS-FILTERED HB APPROACH AND TIME-DOMAIN BENCHMARK (SS LEFT, PS RIGHT) [63].

Nevertheless, since the numerical effort turns out to be of 24 times higher order compared to the results obtained by the HB approach relying on the Lanczos-filter method, the remaining deviations of ∼5% do not seem to justify its consideration as an industrial standard. Furthermore, it is important to keep in mind that due to the convenient blade count, the painful performance of a full-wheel simulation can be avoided in this case. As stressed previously in Tab. 3.3, relying on a full-wheel approach leads to an additional increase of the required numerical effort up to an order of ∼100 000 [CPUh].

Compared to this tremendous amount of consumed computational power, both HB approaches are deemed a fair alternative to provide the unsteady information at the distinct frequencies of aeroelastic interest. Given the deviations with regard to the global aerodynamic excitation behaviour by eqs. (5.11) and (5.12), taking advantage of the respective HB approaches allows for an efficient and time-saving analysis in an industrial design process. Investing the additional numerical effort required by the HB method resolving

Table 5.2.: REQUIRED NUMERICAL EFFORT OF THE ASSESSED SOLUTION APPROACHES, MEASURED IN REQUIRED CPU HOURS.

URANS Time Domain	URANS HB	URANS HB avg. turb.
12 000 [CPUh]	500 [CPUh]	300 [CPUh]

unsteady turbulence yields a benefit of ∼10% which is considered to be a fair compromise between the computational efficiency and the accuracy of the obtained results.

5.2. Transonic Forced Response Excitation

In addition to the results presented in the previous section 5.1 for subsonic flow conditions, the focus of the following section is on an analogous assessment of forced response excitation under transonic flow conditions. This is achieved by the investigation of a high pressure compressor (HPC) rotor blade being excited in the presence of a wake induced by the upstream stator vane. The conducted evaluation focuses on the involved stator-rotor configuration yielding a two-row model as displayed in Fig. 5.16.

Figure 5.16 highlights the transonic character of the assessed rotor blade by displaying the Mach number distribution in the midspan plane of the annulus. The results based on the time-integration method are displayed on the left while the results based on the Lanczos-filtered HB approach are shown on the right hand side. Since the transonic flow state results in a blockage of the complete rotor passage, both the suction and the pressure side of the considered blade surface are affected by the presence of the transonic shock condition. While the pressure side faces the shock condition close to its leading edge at approximately 20% chord length, the shock appears at the adjacent suction side at the rear part of the blade at ∼90% chord.

As in the previous section, the results of solution methods relying on

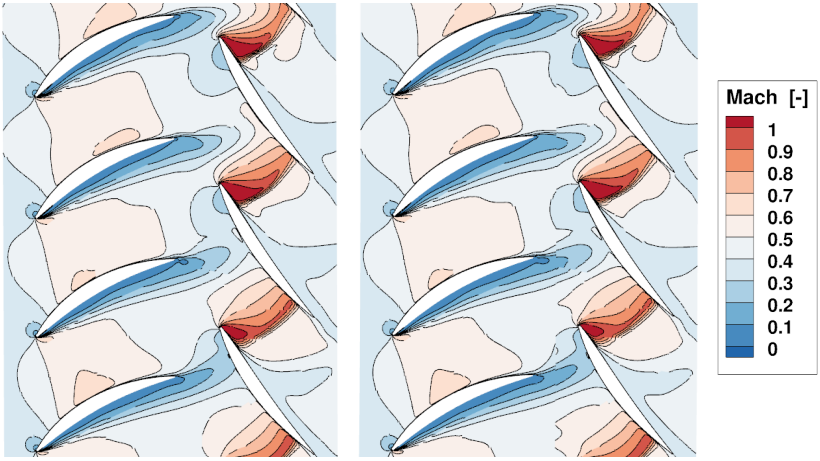

Figure 5.16.: TRANSONIC FLOW CONDITIONS AT ANNULUS MIDSPAN PREDICTED BY THE TIME-INTEGRATION (LEFT) AND THE LANCZOS-FILTERED HB METHOD (RIGHT).

varying degrees of model order reduction for what concerns the resolved unsteadiness are compared in order to evaluate the limitations of the respective approaches. Again, the solution of a time-integration method is used as a benchmark solution deemed to provide results of highest quality by resolving the highest degree of unsteadiness within both the Navier-Stokes as well as the turbulence quantities.

The information provided by the expensive time-stepping method is used to evaluate two Harmonic Balance approaches, one resolving the unsteadiness of the underlying turbulence model by taking advantage of the Lanczos-filter method and one neglecting unsteady turbulence by consideration of its temporal average only. All simulations consider turbulence by relying on Wilcox' k-ω two-equation turbulence model [68]. Due to the high inflow turbulence of the investigated HPC, the flow is considered as fully turbulent and no additional transition model is employed.

The evaluated two-row configuration is discretised by relying on a structured multiblock meshing strategy resulting in the grid structure as displayed

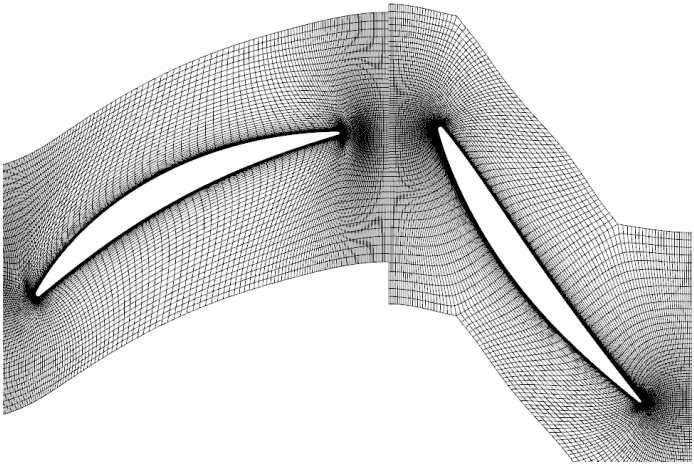

Figure 5.17.: SINGLE PASSAGE MESH OF THE TRANSONIC HPC CONFIGURATION AT 50% RADIAL CHANNEL HEIGHT.

in Fig. 5.17 for both considered rows at 50% radial channel height. The applied mesh consists of approximately 5 million grid points and allows to realise a dimensionless wall distance of $y^+ < 5$ over the surfaces of the considered stator and rotor row. In the following, the setups of the respective solution approaches are recapitulated and the results with regard to the prediction of the resulting aerodynamic excitation are presented in accordance to the course of action followed in the previous section in the case of subsonic forced response excitation.

5.2.1. Time-Integration Setup

The employed time-integration method relies on a solution approach performed exclusively in the time domain and therefore requires the application of a zonal interface realising the communication between the non-rotating stator and the rotating blade row. Since the zonal approach [85] demands identical pitch sections up- and downstream of the interface, a multi-passage mesh has to be applied. The given vane/blade ratio of 54 stator vanes and

Table 5.3.: CONSIDERED BASE FREQUENCIES AND NUMBER OF RESOLVED HARMONICS FOR THE HB HPC SIMULATIONS.

Blade Row	Base Frequency	# Harmonics
Vane 1 (V1)	BPF_1	0 1 2 3
Blade 1 (B1)	VPF_1	0 1 2 3 4

45 rotor blades, respectively, allows here to avoid the performance of a full-wheel simulation by relying on a 40°-model taking into account only 6 stator vanes and 5 rotor blades. However, the required mesh size increases from ∼5 million grid points of the single passage model to ∼35 million grid points.

In order to avoid an undesired interference with reflections induced by the in- and outlet of the considered computational domain, non-reflecting boundary conditions of Giles-type according to [76, 94] are imposed. The time-stepping solution method performs 384 time-steps for the passing of all 5 rotor blades allowing to resolve each passing stator wake by 64 temporal sampling points. According to [87], a sufficiently converged state is provided after having performed 8 revolutions of the 40°-model while the aerodynamic cost quantity to assess convergence is the underlying aerodynamic excitation acting on the rotor blade surface.

5.2.2. Harmonic Balance Setup

In contrast to the time-integration method, the applied HB method allows to take advantage of the single passage mesh as displayed in Fig. 5.17. As for the time-integration benchmark, non-reflecting boundary conditions based on a formulation in the frequency domain are imposed [76]. The considered harmonic content of the respective HB simulations is summarised in Tab. 5.3 by listing the sources of unsteadiness within the associated computational domain and its number of resolved harmonics.

Since the investigated HPC configuration focuses exclusively on the inter-

action of two adjacent rows, the harmonic content to be resolved appears very limited. Accordingly, the main source of unsteadiness within the blade row of aeroelastic interest (B1) is identified by the vane passing frequency (VPF) of the upstream located stator row. The aerodynamic excitation frequency corresponds to the first harmonic of this VPF and is resolved up to its fourth harmonic.

In order to enable the unsteady interaction between both rows, the blade passing frequency (BPF) is resolved in the upstream vane row (V1) by taking into account 3 harmonics. The non-linear coupling between the resolved unsteady effects with the temporal average is realised for all harmonic content as indicated by zero entries in the column of considered harmonics.

In order to estimate the impact of unsteady turbulence on the prediction of the aerodynamic excitation in the blade row operating downstream of the stator vane, two differing HB simulations are performed. The first simulation allows to consider unsteady turbulence effects by solving the transport equations linked to turbulence modeling in an unsteady fashion. A reliable solution behaviour is provided for this case by exploiting the Lanczos-filter method developed in this thesis.

Furthermore, a second HB simulation neglecting the unsteady turbulence behaviour by solving only for the temporal average of turbulence quantities is performed. The differences of the assessed solution approaches becomes more apparent by comparing the axial propagation of turbulence enabled by the respective solution methods.

The differing treatment of variables linked to turbulence modeling is described in Fig. 5.18, where the axial propagation of the eddy viscosity ratio Ψ_t according to eq. (5.4) is plotted in the annulus midspan section of the investigated two-row HPC configuration. The resulting state of turbulence based on the time-integration method is shown on the left hand side of Fig. 5.18, whilst the results of the HB approaches - either considering or neglecting unsteady turbulence - are displayed in the middle and on the right hand side, respectively.

Starting with a uniform inflow of high turbulence intensity, the time-integration method relying on the zonal interface approach allows to trans-

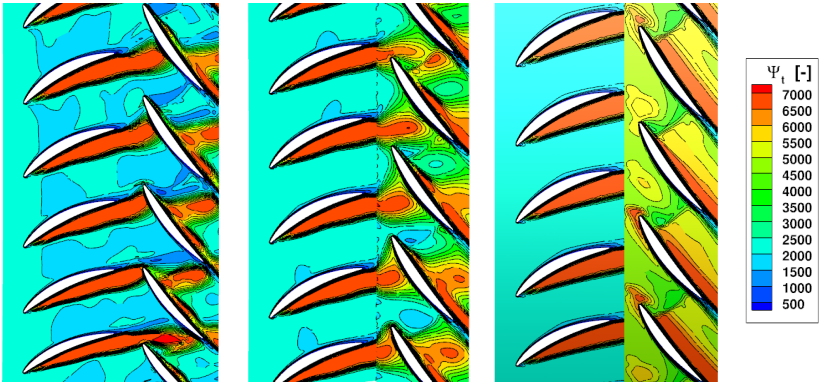

Figure 5.18.: AXIAL PROPAGATION OF THE EDDY VISCOSITY RATIO Ψ_t BASED ON TIME-INTEGRATION (LEFT), LANCZOS-FILTERED HB (MIDDLE) AND HB BASED ON TIME-AVERAGED TURBULENCE (RIGHT).

port the increased level of eddy viscosity induced by the wakes of the upstream stator row into the blade row of aeroelastic interest without any visible loss of information.

The Harmonic Balance method resolving the unsteadiness of the turbulence quantities allows to transport the unsteady turbulence information in the presence of the wake into the downstream blade row by taking into account 4 VPF-harmonics. However, the wake information is predicted to be less distinct due to the limited number of resolved harmonics and the application of the proposed Lanczos-filter method as already discussed in section 2.4. Nevertheless, compared to the HB approach relying on the highest degree of model order reduction by focusing on the temporal average of turbulence only, the turbulent inflow condition for the evaluated rotor geometry is considered of substantially higher quality.

The same holds for what concerns the transport of the turbulence quantities through the rotor passage as highlighted by the large differences in the level of the eddy viscosity ratio Ψ_t downstream of the passage blocking shock. While the HB method solving for unsteady turbulence is able

to reproduce the turbulence behaviour at least qualitatively in accordance with the time-integration benchmark, the turbulent state downstream of the shock condition reveals a substantial mismatch in both quality and quantity if unsteady turbulence is neglected.

5.2.3. Impact of Unsteady Turbulence on the Aerodynamic Excitation Behaviour at Transonic Flow Conditions

In the following, the benefit of the enhanced unsteady treatment of turbulence during the solution process in the frequency domain is discussed by an assessment of the aerodynamic excitation of the HPC rotor row. The unsteady surface pressure fluctuation appearing at the upstream located vane passing frequency is compared for the solution approaches described above. Furthermore, the impact on the prediction of the resulting generalised force is described and the observed differences are related to required numerical effort.

As in the previous section 5.1, the investigation is started by an analysis of the deviations with regard to the predicted pressure fluctuation amplitude between the evaluated HB approaches and the time-integration benchmark. Following eq. (5.5), the differences between the HB approach neglecting the impact of unsteady turbulence effects and the benchmark solution generated in the time domain are displayed in Fig. 5.19. The suction side of the considered HPC rotor is shown on the left and the pressure side on the right hand side of Fig. 5.19. The trailing edge of both the suction and the pressure side is headed towards the middle of Fig. 5.19 as the positions of the leading and the trailing edge are indicated by their respective abbreviations LE and TE, respectively.

According to Fig. 5.19, the leading deviations can be observed in regions dominated by the presence of the shock. Since the shock condition is equivalent to a discontinuity in the associated pressure field, the aerodynamic excitation is highly dependent on the prediction of the shock oscillation at the eigenfrequency of aeroelastic interest. Recalling the time-averaged shock position identified in Fig. 5.16 on the pressure side at approximately 20%

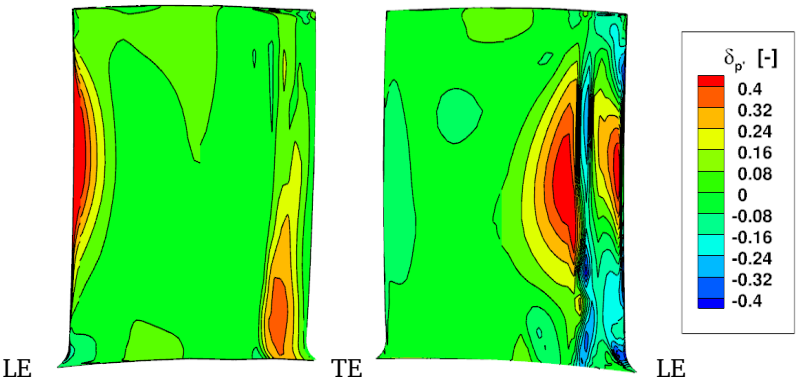

Figure 5.19.: DIFFERENCES OF THE PRESSURE FLUCTUATION AMPLITUDE BETWEEN HB APPROACH NEGLECTING UNSTEADY TURBULENCE AND TIME-DOMAIN BENCHMARK (SS LEFT, PS RIGHT).

chord length, the deviations observed in Fig. 5.19 over the first 30% chord length of the pressure side can be linked to a differing prediction of the shock motion.

The same holds for the deviations observed in Fig. 5.19 over the suction side where major deviations can be observed close to the blade's leading edge and in the last ∼10% chord length close to the trailing edge. As the time-averaged position of the shock on the rotor suction side is identified at approximately 90% chord, the deviations observed in the rear part of the suction side are induced by a differing prediction of the shock movement as well though appearing increasingly towards the rotor hub.

The deviations obtained by an equivalent comparison according to eq. (5.6) between the time-integration benchmark and the HB method resolving unsteady turbulence are shown in Fig. 5.20. The resulting deviations are presented in the same way as previously in Fig. 5.19 displaying the rotor suction side on the left and the pressure side on the right hand side of Fig. 5.20. Focusing on the regions affected by the presence of the shock, the deviations observed in the case of neglected unsteady turbulence are reduced

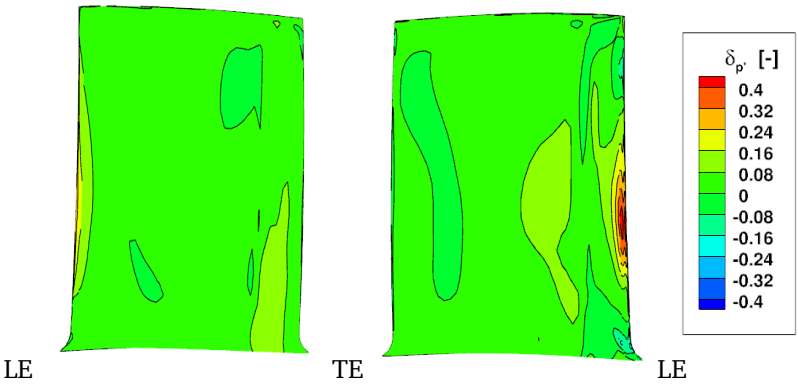

Figure 5.20.: DIFFERENCES OF THE PRESSURE FLUCTUATION AMPLITUDE BETWEEN LANCZOS-FILTERED HB APPROACH AND TIME-DOMAIN BENCHMARK (SS LEFT, PS RIGHT).

substantially if turbulence is considered in an unsteady fashion during the solution process in the frequency domain. Although slight differences can still be noticed in the shock region on both the suction and the pressure side displayed in Fig. 5.20, the prediction of the pressure fluctuation amplitude at the exciting VPF shows significant better agreement with the time-integration benchmark. The highest deviations appear locally close to the pressure side's leading edge in the midspan region indicating remaining local differences in regions of high shock oscillations.

This statement can be confirmed by plotting the results of the pressure fluctuation amplitude obtained by the respective solution approaches over the axial chord length l_{ax} as shown in Fig. 5.21 for the rotor midspan. In Fig. 5.21, the pressure fluctuation is normalised by the total inlet pressure level $p_{t,\mathrm{in}}$ and the pressure side is displayed in the range between $-1 < x/l_{\mathrm{ax}} < 0$ while the suction side is shown at $0 < x/l_{\mathrm{ax}} < 1$.

The results representing the pressure fluctuation amplitude based on the time-integration benchmark are plotted with a dashed line, whereas the solid line corresponds to the solution of the HB approach resolving unsteady turbulence and the solid-dotted line marks the HB result considering the

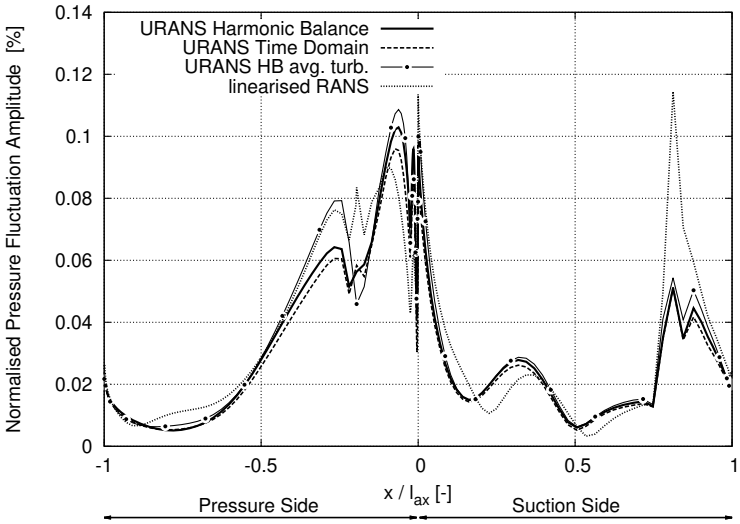

Figure 5.21.: AMPLITUDE OF THE SURFACE PRESSURE FLUCTUATION AT THE INVESTIGATED VPF ALONG 50% ROTOR SPAN.

temporal average of turbulence only.

As expected from the results displayed in Figs. 5.19 and 5.20, the results agree over the major part of both the suction and the pressure side. Significant disagreements can be observed only locally in the presence of the shock in the region between $-0.4 < x/l_{\mathrm{ax}} < -0.1$ and $0.75 < x/l_{\mathrm{ax}} < 0.9$, that is. In both cases, the consideration of unsteady turbulence effects allows to close the gap between the time-integration benchmark and the HB method limited to the temporal average of turbulence almost completely. This is observed in particular in the region of shock oscillation on the rotor pressure side at $-0.4 < x/l_{\mathrm{ax}} < -0.1$ where the highest deviations between the time-stepping method and the HB method reduced to averaged turbulence can be observed.

However, in order to give the quality of the compared HB approaches a context, additional results based on a temporal linearisation around the associated steady RANS state are plotted in Fig. 5.21 with a dotted line. These

results are generated based on a linearisation of both the time-dependent inflow condition as well as the flow state which represents for lots of aeroelastic applications the industrial standard course of action. Though benefiting from low numerical requirements and short runtimes, it relies obviously on a very high degree of simplification and model order reduction. Consequently, the obtained results exceed the deviations of both HB approaches over almost the entire chord length. Focusing on the prediction in the regions close to the shock condition, the linearised approach yields results of poor quality if compared to both assessed HB solution approaches.

In addition to the above stressed deviations with regard to the pressure fluctuation amplitude acting on the investigated rotor surface, the associated phase relation is considered to be of same importance. Therefore, the associated differences in the predicted phase relation are discussed in the following in an analogous manner. Based on eq. (5.7), the resulting differences between the time-integration benchmark and the HB method neglecting unsteady turbulence are displayed in Fig. 5.22. Again, the rotor suction side is displayed on the left and the pressure side on the right hand side, respectively.

In contrast to the results discussed above in the context of the pressure fluctuation amplitude, the deviations with regard to the associated phase relation are not limited to the shock related regions. Although also in the presence of the shock condition deviations up to 15° can be noticed, additional regions highlighting deviations of same order appear on both the suction and the pressure side. This is in particular the case for the front region of the suction side, where major deviations can be observed by evaluating regions closer to the hub and the tip of the rotor blade. Furthermore, an additional spot of differing phase relation can be noticed on the rotor pressure side while passing ∼75% of the chord from the leading to the trailing edge.

The differences observed upstream of the shock position at the rotor suction side hint at a differing propagation of the pressure fluctuation caused by a differing treatment of the turbulence behaviour within the exciting stator wake and the rotor boundary layer. Recalling the differences with regard to the axial propagation of the eddy viscosity ratio Ψ_t as shown in Fig.

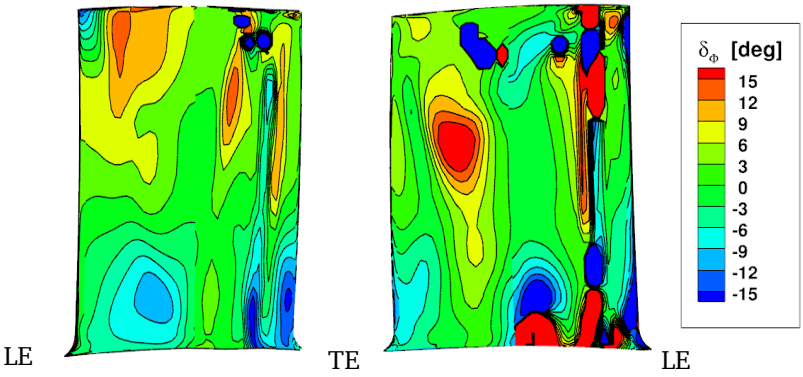

Figure 5.22.: DIFFERENCES OF THE PRESSURE FLUCTUATION PHASE RELATION BETWEEN HB APPROACH NEGLECTING UNSTEADY TURBULENCE AND TIME-DOMAIN BENCHMARK (SS LEFT, PS RIGHT).

5.18, the front part of the rotor suction side is affected by this in particular.

The observed deviations with regard to the pressure fluctuation phase relation can be alleviated significantly by taking into account the unsteadiness within the employed turbulence model as demonstrated by Fig. 5.20. While slight deviations of lower order appear locally in the regions affected by the shock condition, the differences observed over the remaining rotor surface if unsteady turbulence is neglected fade out and a substantial better agreement with the performed time-integration benchmark is achieved for both the suction and pressure side. Since the prediction of the pressure phase angle improves in particular also for the regions up- and downstream of the shock, the benefit in considering turbulence in an unsteady fashion consists not only in an improved prediction of the shock oscillation but also in an enhanced prediction of the fluctuation's propagation.

In order to provide an additional estimator on the quality of the predicted pressure fluctuation phase angle Φ, the results of the respective solution approaches are plotted in Fig. 5.24 along the axial chord length l_{ax} at the rotor midspan. In Fig. 5.24, the pressure side is displayed in the range

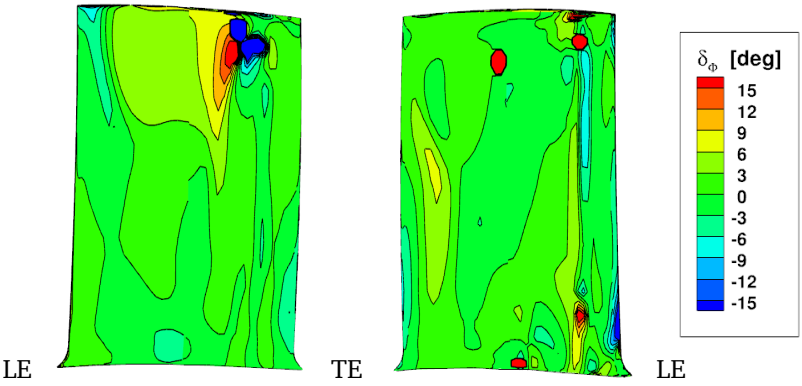

Figure 5.23.: DIFFERENCES OF THE PRESSURE FLUCTUATION PHASE RELATION BETWEEN LANCZOS-FILTERED HB APPROACH AND TIME-DOMAIN BENCHMARK (SS LEFT, PS RIGHT).

between $-1 < x/l_{ax} < 0$ and the suction side between $0 < x/l_{ax} < 1$. The fluctuation phase angle predicted by the time-integration reference is plotted with a dashed line, while the results of the Harmonic Balance method either resolving or neglecting unsteady turbulence are displayed by the solid and the solid-dotted line, respectively.

The overall agreement of both HB appraoches with the time domain benchmark is remarkable though the HB method reduced to the temporal average of tubulence reveals deviations on the pressure side in the range between $-0.75 < x/l_{ax} < -0.55$. However, recalling the deviations shown in Fig. 5.22, the impact of neglecting unsteady turbulence effects turns out to be of lowest order at the rotor midspan. As indicated by Figs. 5.22 and 5.23, taking into account unsteady turbulence allows to overcome the observed deviations if only the temporal average of turbulence is taken into account during the solution process in the frequency domain.

In addition to the discussed solution approaches performed in the time and frequency domain, again the result generated by a temporal linearisation around the steady RANS state is displayed in Fig. 5.24 with a dotted line. Although in general capable of reproducing the qualitative behaviour of the

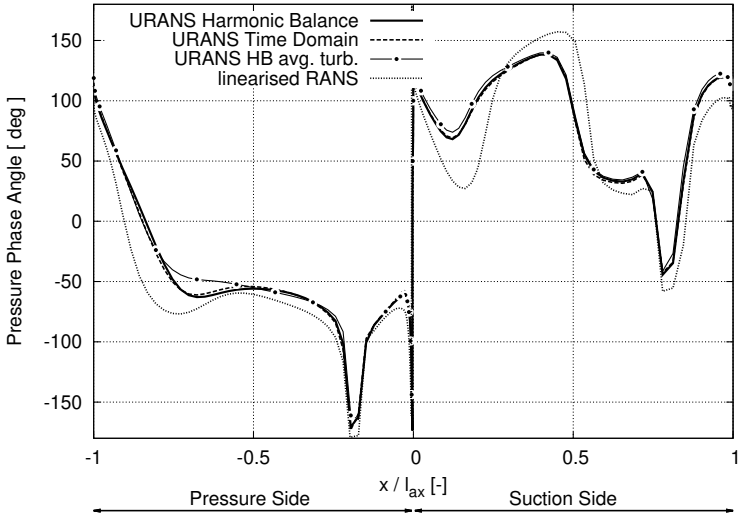

Figure 5.24.: PHASE RELATION OF THE SURFACE PRESSURE FLUCTUATION AT THE INVESTIGATED VPF ALONG 50% ROTOR SPAN.

pressure fluctuation phase angle Φ, the phase relation predicted by pure linearisation shows quantitative deviations of up to $30° - 50°$ over a large range of the investigated chord length. Accordingly, even relying on the reduced HB method neglecting unsteady turbulence allows to provide results of substantial higher quality than achieved by the linearised approach as frequently used as standard method in industrial applications.

While the pressure fluctuation acting on the assessed rotor surface describes the behaviour of the aerodynamic excitation itself, the evaluation of the associated generalised force provides further insight on the resulting aeroelastic behaviour by embedding the excitation in the context of the underlying blade motion. Hence, the deviations with regard to the local, specific generalised force f_g between the time-integration benchmark and the HB method considering the temporal average of turbulence only are displayed in Fig. 5.25. The displayed deviations are calculated according to eq. (5.9) and shown for the suction side on the left and for the pressure side

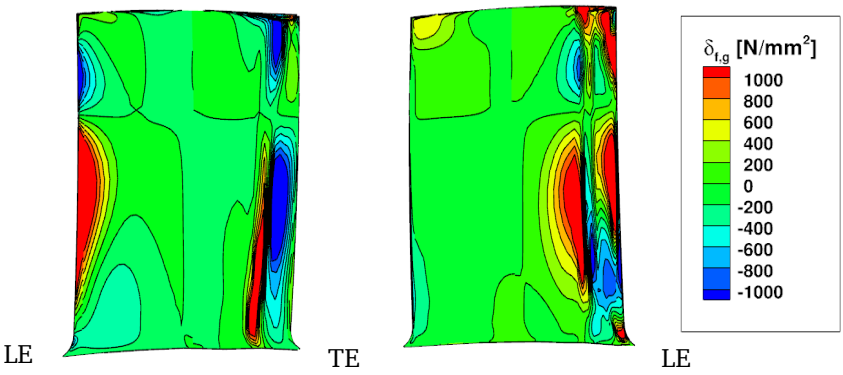

Figure 5.25.: DIFFERENCES OF THE SPECIFIC GENERALISED FORCE BETWEEN HB APPROACH NEGLECTING UNSTEADY TURBULENCE AND TIME-DOMAIN BENCHMARK (SS LEFT, PS RIGHT).

on the right hand side of Fig. 5.25. The trailing edge of both the suction and the pressure side is heading towards the middle of Fig. 5.25 and the position of leading and trailing edge is indicated by their abbreviations LE and TE.

Recalling the deviations with regard to the surface pressure fluctuation amplitude from Fig. 5.19, the regions of differing generalised force contributions correspond to regions with high deviations of the fluctuation amplitude. For the rotor pressure side, that is the region affected by the presence of the shock from the rotor leading edge up to ∼40% of the chord. For what concerns the rotor suction side, the region in the vicinity of the leading edge as well as the region of shock interference in the final ∼20% of the chord reveal substantial deviations between both approaches.

Due to the underlying blade motion, deviations close to the tip of the rotor suction side appear with an opposite sign if compared to deviations around the rotor's midspan. For the region at ∼75% span of the suction side, no significant differences in the local generalised force can be observed while at the same time substantial differences with regard to the predicted pressure fluctuation amplitude can be identified in Fig. 5.19. Since the

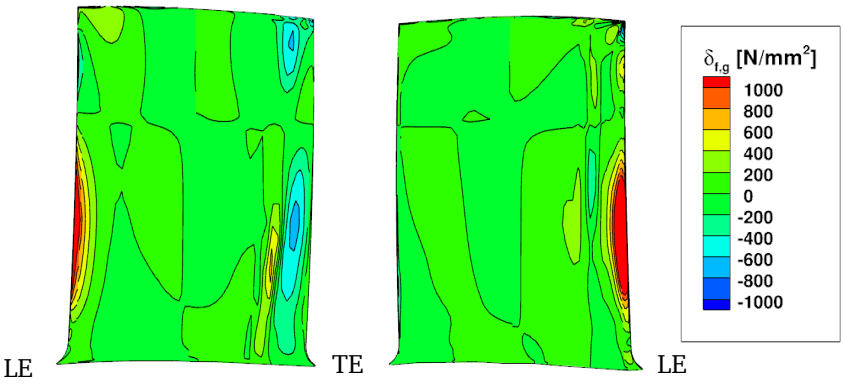

Figure 5.26.: DIFFERENCES OF THE SPECIFIC GENERALISED FORCE BETWEEN LANCZOS-FILTERED HB APPROACH AND TIME-DOMAIN BENCHMARK (SS LEFT, PS RIGHT).

assessed eigenmode does not contribute to the blade's motion at this span, the deviations of the predicted excitation hardly affect the resulting generalised force.

The same holds for the resulting differences at the rotor pressure side in the presence of the shock condition. Due to the high blade motion in the tip region, substantial differences with regard to the specific generalised force can be noticed while the deviations of the associated pressure fluctuation amplitude appear to be rather low there. At ∼75% span, no substantial differences between the compared approaches are highlighted while closer to the blade's midspan, the observed deviations change their sign which is again linked to assessed eigenmode.

In order to estimate the benefit of taking into account the unsteadiness within the applied turbulence model, an equivalent analysis of the deviations between the time-integration benchmark and the HB method resolving unsteady turbulence effects are displayed in Fig. 5.26. The deviation with regard to the local specific generalised force f_g is calculated as proposed by eq. (5.10) and is displayed in accordance with the results presented in Fig. 5.25.

Table 5.4.: COMPUTATIONAL RESOURCES REQUIRED BY THE INVESTIGATED SOLUTION METHODS FOR THE PREDICTION OF TRANSONIC FORCED RESPONSE EXCITATION.

Solution Method	$\delta_{F,g}$	CPU-Time
URANS Time-Domain	-	16 000 [CPUh]
URANS Harmonic Balance	0.33%	500 [CPUh]
URANS HB avg. Turb.	5.47%	400 [CPUh]
linearised RANS	14.89%	25 [CPUh]

As expected from the improved quality of the predicted surface pressure fluctuation noticed above, the deviations between time-integration benchmark and the Harmonic Balance method can be reduced significantly if the evaluation of the generalised force is based on the additional consideration of turbulence in an unsteady fashion. The reduced appearance of deviations with regard to the resulting specific generalised force demonstrates an improved agreement between both approaches taking into account unsteady turbulence effects, either by the time or the frequency domain method.

Remaining differences can be observed close to the leading edge of the blade as well as in the shock region on the rotor pressure side. However, for both regions the deviation turns out to be of lower order indicating an enhanced prediction of the aerodynamic excitation behaviour if the impact of turbulence is considered by exploiting the proposed Lanczos-filter method.

Finally, its impact on the global aeroelastic excitation behaviour is evaluated by listing the integral values of the resulting generalised force F_g in Tab. 5.4 as proposed by eqs. (5.11) and (5.12). By taking into account the unsteady behaviour of turbulence in the assessed Harmonic Balance method, the deviation in the magnitude of the predicted global generalised force can be reduced from 5.47% to 0.33%. However, for both approaches it has to be kept in mind that an integral analysis of a quantity allows local deviations of

differing sign to balance each other. Consequently, the value of the compared global values of the resulting generalised force F_g has to be enjoyed carefully for both evaluated HB approaches though they confirm the results discussed on the discrete level in Figs. 5.19 - 5.26.

Furthermore, both HB approaches allow to provide an enhanced prediction of the global aeroelastic excitation behaviour compared to a solution method based on a pure temporal linearisation around the steady RANS state as this approach predicts the generalised Force F_g to differ in an order of ∼15%. This confirms the improved solution quality in general if a Harmonic Balance method is chosen instead of the established linearised method.

Consequently, the question of the numerical effort associated to the respective solution methods arises at this stage. Hence, the numerical resources measured in consumed CPU hours are listed in Tab. 5.4. Obviously, the tremendous numerical effort required by the time-integration method makes it an unattractive choice if a high number of performance points has to evaluated. Again it has to be kept in mind, that a less convenient blade count leads to a further increase in the required computational resources.

By relying on the investigated HB method, the consumed CPU hours can be reduced significantly by a factor of ∼30. Given the comparable amount of required computational resources and the enhanced quality of the obtained results, considering the impact of unsteady turbulence effects during the solution process of the Harmonic Balance method provides a suitable and attractive compromise between an acceptable numerical effort while delivering at the same time a reliable prediction of the aeroelastic excitation behaviour.

Obviously, the less time consuming alternative consists in the temporal linearisation around the associated steady flow state allowing for an additional speed-up of factor ∼20. Assuming the scenario of a massive number of performance points needing to be evaluated, a meaningful course of action might consist in performing predominantly linearised calculations and confirming the results of the most critical performance points by relying on the enhanced HB method resolving the unsteady behaviour of turbulence.

5.3. Conclusion

In the course of this chapter, the impact of neglecting unsteady turbulence effects while following a frequency domain based model order reduction approach is assessed and evaluated for forced response applications. Allowing for an efficient and robust consideration of unsteady turbulence effects in the frequency domain, the Lanczos-filter method proposed in chapter 2 is used to investigate how a consideration of the unsteadiness in the underlying turbulence models affects the aerodynamic forced response behaviour. First, the impact of the filter application is assessed numerically in section 5.1.3 confirming the filter to affect the solution behaviour in a negligible order while at the same time providing an enhanced level of robustness for forced response applications. Consequently, it is applied in the following to investigate both subsonic and transonic flow conditions by the analysis of either a subsonic LPT or a transonic HPC configuration.

For both applications, unsteady pressure distributions relying on differing levels of resolved unsteadiness are compared in order to assess the feasibility of the respective degree of model reduction. A Harmonic Balance approach neglecting unsteady turbulence effects while at the same time benefiting from lower numerical requirements by preventing the solution of additional transport equations shows rather large differences in both amplitude and phase of the unsteady pressure fluctuations. Since the differences in the resulting unsteady pressure distributions are not of negligible order for what concerns the resulting generalised force, the model reduction relying on an averaged consideration of turbulence is not necessarily considered as a favourable approach.

Better agreement can be obtained by resolving the unsteadiness in the employed turbulence models during the pursued Harmonic Balance approach. The additional numerical effort caused by the solution of additional transport equations associated with the employed turbulence model yields a suitable compromise between computational efficiency and physical capability of the investigated frequency domain approach.

Chapter 6

Impact of Unsteady Turbulence Effects on the Prediction of Flutter

In the following chapter, the investigations discussed in chapter 5 with regard to forced response excitation are expanded to the evaluation of the aerodynamic damping. Since from an aerodynamic point of view, the flutter stability of an airfoil is assessed predominantly by calculating the aerodynamic damping, this is considered to be equivalent to the flutter evaluation in the following. In order to quantify the impact of considering turbulence in an unsteady fashion in the context of flutter evaluation, the results of three differing solution approaches are compared.

The first approach relies on a temporal linearisation around the flow field generated by a steady solution of the associated performance point. The second approach corresponds to a Harmonic Balance simulation solving for the average of the applied turbulence model only. Finally, results of the Harmonic Balance solver resolving the unsteadiness of the underlying turbulence model are compared to the remaining solution approaches.

Due to the increasing level of resolved unsteadiness within the respective solution approaches, it is possible to assess the impact of the respective degrees of model order reduction. The properties of the investigated approaches with regard to computational stability, run time and quality of the obtained results are discussed for sub- and transonic flutter tasks.

6.1. Flutter Evaluation Setup

The investigated configurations focus exclusively on the evaluation of the flutter instability of a compressor stator vane. In general, the assessment of the flutter behaviour follows the course of action recommended by the AGARD manual on aeroelasticity in axial turbomachinery [5].

Accordingly, the configuration is reduced to a single passage model where periodic boundary conditions are imposed in the circumferential direction. The resulting mesh at the investigated vane's midspan is displayed in Fig. 6.1. In contrast to the configurations discussed in the context of forced response, flutter is evaluated on a mesh deforming periodically according to the eigenmode of interest. In fact, the periodic deformation of the geometry, and therefore of the underlying mesh, is the dominant source of unsteadiness in the pursued flutter evaluation approach. Hence, both the mesh and the surface of the analysed stator vane displayed in Fig. 6.1 are oscillating with the evaluated flutter frequency and therefore not fixed in space and time.

At the in- and outlet of the flow field, radial profiles invariant in time are imposed by taking advantage of non-reflecting boundary conditions as described in [75, 76, 94]. While at the outlet only a radial profile of the static pressure is prescribed, radial profiles of the total temperature $T_{t,\mathrm{in}}$, the stagnation pressure $p_{t,\mathrm{in}}$ and the pitchwise flow angles are imposed as inflow boundary condition. Variation of the static outflow pressure allows to reproduce different performance points of the underlying compressor head curve. In the following, the flutter behaviour at performance points of subsonic and transonic flow states are assessed by throttling the outflow condition.

In order to determine proper inflow conditions for the quantities required in the context of turbulence modeling, radial profiles of turbulence intensity $\mathrm{Tu}_{\mathrm{in}}$ and turbulence length scale $l_{\mathrm{Tu,\,in}}$ are imposed at the inlet. Due to the high inflow turbulence conditions met within the investigated HPC, the flow can be considered as fully turbulent. The impact of turbulence is considered by application of Wilcox' $k-\omega$ two-equation model [68].

Based on the respective solution approaches, the unsteadiness of the

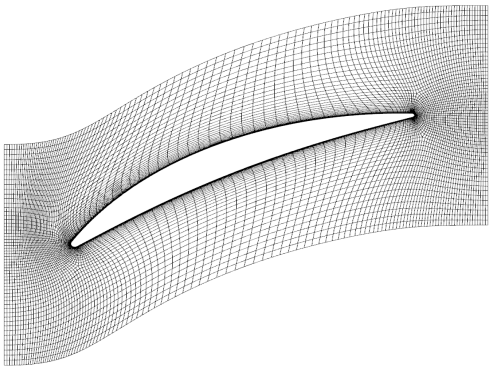

Figure 6.1.: SINGLE PASSAGE GRID TOPOLOGY OF THE EVALUATED HPC STATOR AT THE VANE'S MIDSPAN.

applied turbulence model is treated by varying degrees of model order reduction. The assessed solution approaches as well as their substantial characteristics and advantages are discussed in the following.

Linearised Flutter Evaluation

This way to evaluate the flutter stability has been established as a common standard for a long time [5, 95, 96, 97, 98, 99, 100]. After performing a steady RANS simulation determining the respective performance point, a temporal linearisation around the steady flow field is conducted according to the flutter motion of interest.

In many cases, turbulence is treated in these linearised approaches as to be frozen at its steady state. This means that the underlying turbulence model is not linearised and no update of the steady state eddy viscosity is taken into account. The linearised approach assessed in this work relies on this frozen eddy viscosity approach as well and provides therefore the highest degree of model order reduction for what concerns the handling of turbulence.

The benefits of this approach result in a very fast and time efficient method

to predict flutter, in particular if a high number of performance points has to be evaluated. Therefore, its application is obviously a very attractive choice for industrial applications and design tasks.

However, the major limitation of this approach consists of neglecting the difference between temporal average and the steady state of the evaluated flow field. If the differences between steady state and temporal average increase substantially - for instance due to a shift in the axial position of a passage blocking shock - the induced error caused by the linearisation around the wrong flow state can exceed the acceptable threshold and lead to solutions of completely differing behaviour.

Compared to this, neglecting any higher order turbulence effects beyond its steady state approximation appears to be rather consequent and not to increase the leading error. The impact of the respective constraints and to what extent the induced errors can be justified if applied to the prediction of flutter is quantified in the following.

Flutter Evaluation based on the Harmonic Balance Method

Two different Harmonic Balance configurations are assessed in the scope of this chapter. As in the previous chapters, the results of a Harmonic Balance approach considering only the temporal average of turbulence are compared to results resolving the unsteadiness within the employed turbulence model.

The resolved harmonic content of the discussed HB simulations is summarised in Tab. 6.1. For all Harmonic Balance simulations presented in this chapter, four harmonics of the investigated flutter motion are resolved. The coupling of the resolved harmonic content with the temporal average of the flow field - the zero harmonic or the DC component, that is - is enabled in all performed HB simulations. The associated Inter Blade Phase Angle varies dependent on the evaluated nodal diameter, denoted in Tab. 6.1 by ND. Due to the angle conventions of the underlying flow solver TRACE, positive nodal diameters correspond to flow patterns propagating in negative circumferential direction.

Table 6.1.: CONSIDERED HARMONIC CONTENT OF THE CONDUCTED HB FLUTTER SIMULATIONS.

Base Frequency	# Harmonics	IBPA
Flutter - 446 [Hz]	0 1 2 3 4	$-\frac{2\pi \cdot \mathrm{ND}}{N_{\mathrm{Vanes}}}$

Compared to the linearised approach introduced above, both HB approaches allow for an expansion around the temporal average instead of the steady flow state. This allows in particular to consider a shift of the evaluated performance point in the presence of the resolved transient effects. Furthermore, both HB approaches take 4 harmonics of the assessed flutter frequency into account enabling the consideration of non-linear contributions up to the chosen truncation order. Therefore, both approaches can be considered to be of higher accuracy than the linearised method described above.

In addition to that, one of the investigated HB methods resolves the unsteadiness of the employed turbulence model. Comparing the results of the respective solution methods allows to quantify the impact of unsteady turbulence on the prediction of flutter as well as to estimate the error induced by the approach based on pure linearisation and its associated limitations.

6.2. Subsonic Flutter Excitation

In order to provide subsonic flow conditions, the outflow pressure is throttled to a performance point of decelerated flow conditions while at the same time being sufficiently far away from the limits of the underlying compressor map.

The aeroelastic behaviour with regard to flutter instability is evaluated for a varying number of nodal diameters (ND) of the analysed eigenmode. The result of the predicted aerodynamic damping can be plotted over the

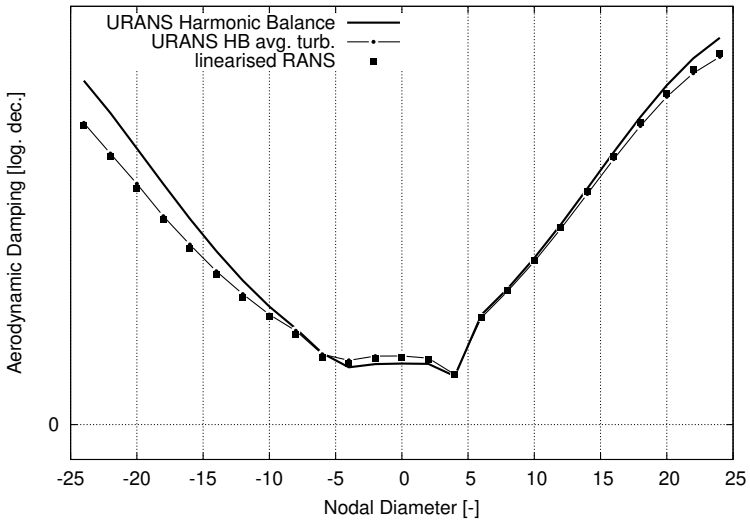

Figure 6.2.: PREDICTION OF THE SUBSONIC FLUTTER BEHAVIOUR OVER THE CONSIDERED RANGE OF NODAL DIAMETERS.

analysed nodal diameters resulting in a flutter curve as displayed in Fig. 6.2. Starting at a nodal diameter of zero - representing a deformation of all vanes in phase with the assessed stator row - each second nodal diameter of positive and negative sign is evaluated. The results referring to the solution approach of temporal linearisation around the steady RANS state are plotted with solid squares. The aerodynamic damping generated by the complete Harmonic Balance approach is plotted with a solid line whilst the HB results neglecting the impact of unsteady turbulence correspond to the solid line being additionally marked with dots.

Over the complete range of assessed nodal diameters, all approaches predict the flutter behaviour to be of equivalent quality. While for nodal diameters of low absolute value, the results shown in Fig. 6.2 agree also quantitatively very well, growing differences between the respective solution approaches can be observed if the absolute value of the evaluated nodal diameter increases. While both approaches neglecting the impact of any

Table 6.2.: AVERAGED NUMERICAL EFFORT OF THE ASSESSED SOLUTION APPROACHES, MEASURED IN REQUIRED CPU HOURS.

linearised RANS	URANS HB avg. turb.	URANS HB
6 [CPUh]	200 [CPUh]	300 [CPUh]

unsteady turbulence effects on the aerodynamic damping match well over the complete flutter curve, the HB approach considering unsteady turbulence differs increasingly for the nodal diameters of high absolute value in an order of up to 10%.

The results presented in Fig. 6.2 indicate that the limitations of the linearised approach - given by the linearisation around the steady state and neglecting any changes of the underlying eddy viscosity - are not of same importance if applied to the subsonic evaluation of flutter. This statement is based on the observations described above indicating the neglection of unsteady turbulence effects to be the leading error and underlining the predominantly linear character of subsonic flutter in general.

The numerical efforts required by the respective solution approaches are summarised in Tab. 6.2. The numerical effort is measured here by the averaged CPU hours (CPUh) needed for the evaluation of one nodal diameter. Recalling the rather low deviations of the flutter curves displayed in Fig. 6.2, the application of the linearised approach can be justified in favour of its low numerical efforts with regard to computational time and efficiency. However, if the assessed geometry is operating close to the limit of flutter stability, the results of the linearised approach should be confirmed by a HB approach benefiting from an unsteady consideration of turbulence given the observed impact on the aerodynamic damping in an order of 10%.

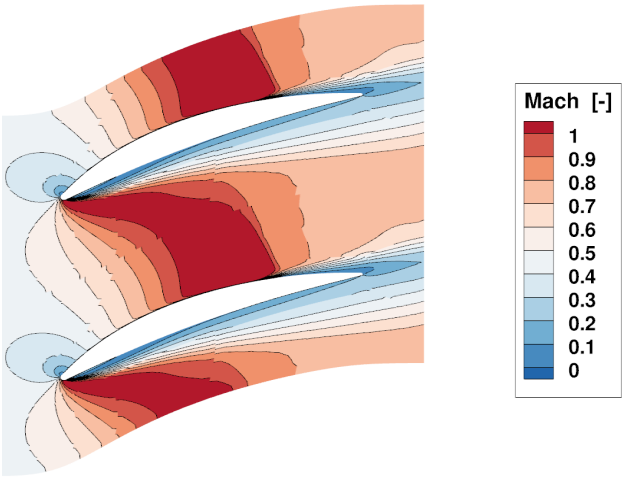

Figure 6.3.: TIME AVERAGED FLOW FIELD AT STATOR MIDSPAN UNDER TRANSONIC FLOW CONDITIONS AT ND+20.

6.3. Transsonic Flutter Excitation

The outflow pressure of the considered stator configuration is reduced resulting in a transonic flow state. The time averaged flow field predicted by the Harmonic Balance approach resolving unsteady turbulence is shown Fig. 6.3, where the Mach number Ma is plotted in the assessed stator's midspan section for the nodal diameter of ND = +20. The flow state is dominated by the presence of a shock blocking the stator passage completely over the entire channel height. Again, a steady simulation is performed first which is used as a basis for the linearised flutter approach. For all considered nodal diameters of the flutter curve, the linearised approach provides sufficiently converged results of the evaluated aerodynamic damping.

As previously in the context of subsonic flutter evaluation, two Harmonic Balance approaches - one neglecting and one resolving the unsteady impact of turbulence - are applied in order to predict the behaviour of flutter in the presence of transonic flow conditions.

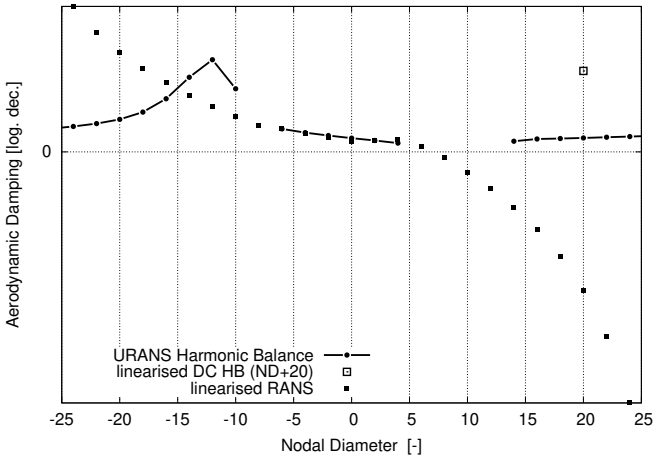

Figure 6.4.: PREDICTION OF THE TRANSONIC FLUTTER BEHAVIOUR OVER THE CONSIDERED RANGE OF NODAL DIAMETERS.

However, if the HB approach neglecting unsteady turbulence is applied to the investigated transonic flow situation, for the majority of the assessed nodal diameters no convergent result of the aerodynamic damping can be obtained. Therefore, the results of this approach are not discussed in the remainder of this section though it is kept in mind, that this approach suffers potentially from substantial limitations for what concerns transonic flutter evaluation. The reason for this unsatisfying behaviour will become more apparent in the context of section 6.4 and will be subject of further discussions there.

Focusing on the Harmonic Balance approach resolving the unsteadiness of turbulence however allows to provide converged results of the aerodynamic damping for almost all nodal diameters of the flutter curve. Exceptions are the nodal diameters of ND = -8 and between $6 \leq \text{ND} \leq 12$, where the performed simulations do not yield suitable results constraining a meaningful evaluation of the flutter stability there. The physical mechanisms acting on both the flow field and the assessed stator vane at these nodal diameters are

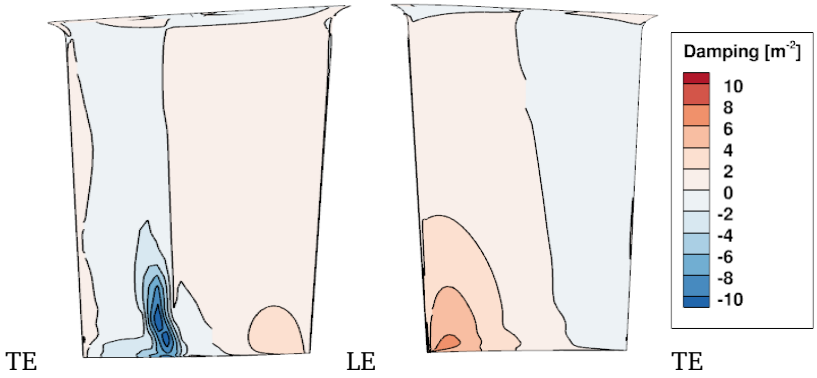

Figure 6.5.: SPECIFIC LOCAL DAMPING OF TRANSONIC FLUTTER CALCULATION AT ND+20, BASED ON URANS HARMONIC BALANCE (SS LEFT, PS RIGHT).

discussed in section 6.4.

The flutter curves based on the available results are displayed in Fig. 6.4 where the predicted aerodynamic damping values are plotted for the assessed nodal diameters. The results obtained from the solution approach relying on a linearisation around the steady RANS state are marked by solid squares and differ substantially in both quality and quantity over major regions of the flutter curve. Only for the nodal diameters of low order in the range between $-6 \leq \mathrm{ND} \leq 4$ both solution approaches predict corresponding values of the aerodynamic damping.

Increasing the nodal diameter further than $\mathrm{ND} > 6$, the linearised approach indicates an increasing presence of flutter instability which can not be supported if compared to the results of the HB approach considering unsteady turbulence. In contrast to the results generated by the linearisation around the steady RANS state, the simulations relying on the complete HB approach predict the assessed vane geometry to be damped over all nodal diameters where converged results are available.

The substantial deviations between the assessed numerical approaches indicate a substantial differing excitation behaviour which can not be observed

in the subsonic case. Hence, the impact of the shock on the aerodynamic damping is displayed for both the HB and the linearised approach for the nodal diameter of ND = +20 in the Figs. 6.5 and 6.6, respectively.

The specific, local aerodynamic damping predicted by the Harmonic Balance solver is shown in Fig. 6.5 where the suction side is displayed on the left and the pressure side on the right hand side. The position of the stator leading edge is indicated by its abbreviation LE as well as its trailing edge is highlighted by TE. Blue regions correspond to negative values - and therefore undamped areas - whilst aerodynamically damped regions are marked red.

For both the suction and the pressure side, the oscillation of the shock can be identified as the main driver affecting the damping behaviour. Recalling the position of the shock shown in Fig. 6.3 at approximately 60% axial chord length on the stator suction side and close to the leading edge at the pressure side, respectively, the distribution of the peaks in the local damping of Fig. 6.5 agrees with the regions of expected shock interaction.

According to Fig. 6.5, the shock oscillation acts as a damping effect at the leading edge of the pressure side over the complete stator span, in particular close to the stator hub gap at the vane's toe. The same holds for the rear part of the suction side, where in particular close to the hub gap the shock oscillation tends increasingly to excite the vane as highlighted by the blue spot in Fig. 6.5.

The equivalent results of the specific local aerodynamic damping associated to nodal diameter ND = +20 predicted by the approach based on a linearisation around the steady RANS state are displayed in Fig. 6.6. In both quality and quantity, substantial differences can be observed which is not surprising given the deviations of the flutter curves plotted in Fig. 6.4 for the respective nodal diameter.

Obviously, the exciting impact of the shock oscillation at the suction side appears in Fig. 6.6 more distinct if compared to the HB result of Fig. 6.5. This can be observed with regard to both the order as well as the local radial and axial dimension of the region being affected by the presence of the shock. Furthermore, the damping behaviour on the stator pressure side is predicted fundamentally different given the majority of the pressure side to

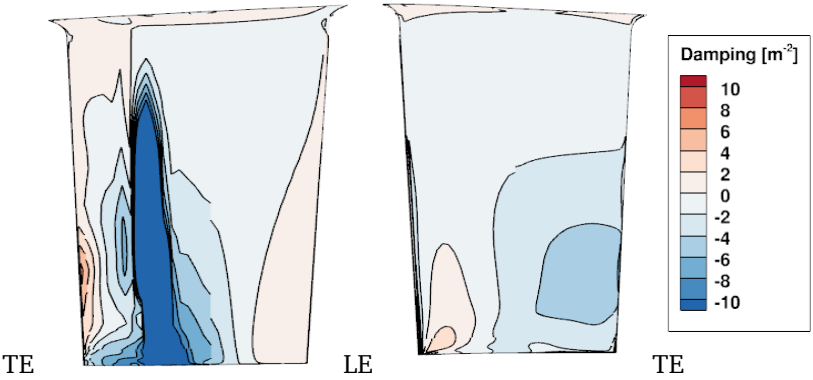

Figure 6.6.: SPECIFIC LOCAL DAMPING OF TRANSONIC FLUTTER CALCULATION AT ND+20, BASED ON LINEARISATION AROUND THE STEADY RANS STATE (SS LEFT, PS RIGHT).

be predicted as being self excited. The damped region at the pressure side's leading edge close to the hub gap is present though it appears substantially smaller and of lower order.

As in the case of subsonic flutter, the question of the leading limitation causing the deviations observed in the flutter curve of Fig. 6.4 arises. Recapitulating the three limitations of the linearised approach compared to the Harmonic Balance method, the impact of the linearisation around the imperfect steady state, the impact of non-linear effects and, finally, the impact of neglecting the unsteadiness within the employed turbulence model has to be assessed.

In order to estimate the impact of differing expansion points between both approaches, the deviations between the profile pressure distribution resulting from the steady RANS state and the temporal average of the Harmonic Balance simulation are displayed in Fig. 6.7 at the stator midspan. The presented profile pressure distribution is normalised by the leading edge's stagnation pressure and is plotted with solid squares for the steady RANS state whilst the result of the complete HB approach is displayed with a solid line. Substantial deviations appear in the rear part of the stator suction side

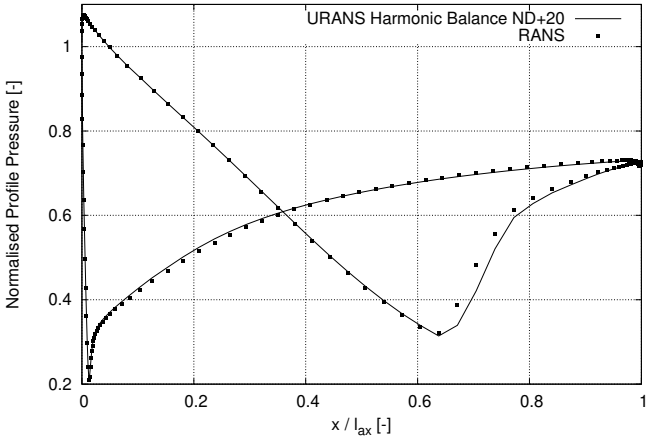

Figure 6.7.: NORMALISED TEMPORAL AVERAGE AND STEADY PROFILE PRESSURE AT THE ASSESSED STATOR VANE'S MIDSPAN.

at $0.65 < x/l_{ax}$ as a result of a differing prediction of the axial shock position. As a result of the discussion of the Figs. 6.5 and 6.6, the presence of the shock acts as the dominating driver for what concerns the global behaviour of flutter.

Therefore, linearisation around an incomplete shock position is expected to affect the results in an unfavourable fashion though its impact remains to be estimated. This can be achieved by an additional simulation based on a linearisation around the temporal average of the flow state predicted by the complete HB approach which is done for the nodal diameter of ND = +20.

The resulting aerodynamic damping is marked in the flutter curves of Fig. 6.4 with a blanked square and shows a substantial differing prediction of flutter stability if compared to the linearisation around the steady RANS state. The result of the global aerodynamic damping in Fig. 6.4 indicates large differences in both quantity and - given the assessed stator to be predicted as globally damped - quality as well.

This is also supported by an analysis of the specific, local aerodynamic

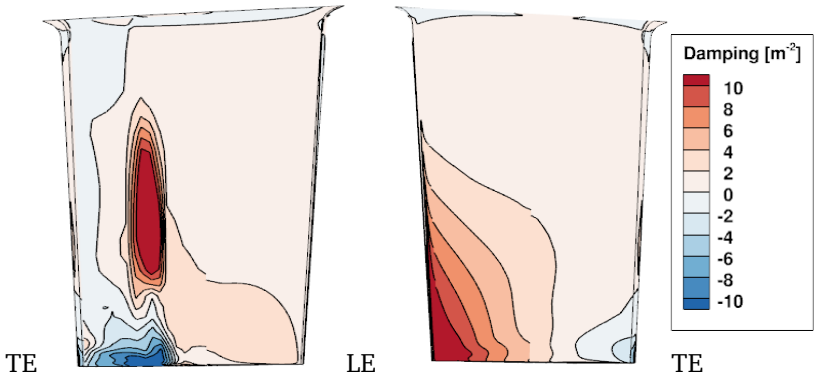

Figure 6.8.: SPECIFIC LOCAL DAMPING OF TRANSONIC FLUTTER CALCULATION AT ND+20, BASED ON LINEARISATION AROUND THE DC OF HARMONIC BALANCE (SS LEFT, PS RIGHT).

damping as displayed in Fig. 6.8. As expected, the shock dominates the damping behaviour completely. While at the suction side close to the stator's hub gap both linearised approaches agree, the simulation linearising around the temporal average of the HB simulation predicts the shock to affect the geometry in a damping manner over substantial parts of the suction side around its midspan region.

Comparing the aerodynamic damping between both linearised approaches on the pressure side, further disagreement can be observed. The linearisation around the temporal average of the HB solution instead of the steady RANS state predicts the shock close to the leading edge to be dominantly damping which holds for vast regions of the complete pressure side.

However, if compared to the results obtained from the non-linear HB approach resolving in addition turbulence in an unsteady fashion, substantial deviations in both quality and quantity can be observed as well. Therefore, despite indicating an improved prediction of the global flutter behaviour as shown in Fig. 6.4, linearisation around an expansion state of higher quality does not allow to close the gap alone though affecting the result essentially.

In order to estimate the impact of the remaining limitations of the lin-

Table 6.3.: AVERAGED NUMERICAL EFFORT OF THE ASSESSED SOLUTION APPROACHES, MEASURED IN REQUIRED CPU HOURS.

linearised RANS	URANS HB avg. turb.	URANS HB
6 [CPUh]	-	360 [CPUh]

earised approach - being the missing consideration of non-linear effects as well as of effects linked to unsteady turbulence - the information of the failed Harmonic Balance approach is missing. As stated at the beginning of this section, the HB approach based on the consideration of non-linear effects by resolving the higher harmonics of the flutter frequency but neglecting the unsteadiness of turbulence by consideration of its temporal average alone suffers from unstable convergence behaviour over the majority of the investigated range of nodal diameters.

However, the observed instability of this solution approach in combination with the tremendous sensitivity to the underlying state of expansion hints that all of the discussed constraints of the linear approach have to be considered sufficiently when applied to the assessed transonic flutter setting.

Although the consumed numerical efforts of the analysed solution methods listed in Tab. 6.3 might still promise the linear method to be the most favourable choice in an industrial design context, the application of this approach has to be checked carefully amid the concerns raised by the results presented in this section. Obviously, there is no gain in saving computational efforts by producing results of poor accuracy and reliability.

Furthermore, even by relying on the lowest degree of model order reduction and referring to the Harmonic Balance approach resolving unsteady turbulence, there are still parts of the flutter curve presented in Fig. 6.4 that can not be assessed by the proposed solution method. The physical effects interfering at these flutter conditions and what is necessary to overcome the observed problems at the respective nodal diameters is discussed in the following.

6.4. Evaluation of Flutter in the Presence of Non-Synchronous Flow Instabilities

The focus of this section is on the analysis of the nodal diameters missing in the transonic flutter curve as introduced in Fig. 6.4. These are the nodal diameters at ND = -8 and in the range between $6 \leq \text{ND} \leq 12$. The mechanism affecting the convergence of these nodal diameters is identified by a discussion of the convergence history and an unsteady analysis of the flow situation relying on a time-integration method. Finally, an approach to overcome the observed difficulties to obtain a reliable prediction of the flutter stability of the missing nodal diameters is proposed and the results are presented.

As previously stated in the context of section 6.3, for certain nodal diameters it is impossible to generate sufficiently converged information for what concerns the aerodynamic damping. Focusing, for instance, on the nodal diameter of ND = +8, the convergence history of the aerodynamic damping shows an oscillating behaviour with non-decaying amplitude as displayed in Fig. 6.9.

As discussed by [58, 101], an oscillating convergence behaviour of a complex fluctuation quantity as shown in Fig. 6.9 hints at the disordered sampling of present frequency content during the solution process in the frequency domain. This is supported by an analysis of the phase angle relation associated to the aerodynamic damping which is plotted in Fig. 6.10 over the performed iteration steps. After the first stage of initialisation during the first 2000 iteration steps, the simulation reaches a state of constant phase shift highlighted by the linear trend of constant derivative for the remaining iteration steps displayed in Fig. 6.10.

Recapitulating the results of [58, 101] - also summarised in the appendix A.4 - the constant phase shift highlighted by Fig. 6.10 can be primarily identified via eq. (A.22) with the presence of frequency content interfering with the harmonic content resolved by the applied flutter setting.

Consequently, the question of the interfering physical mechanism and its dominating frequency arises at this stage since the presence of the assessed

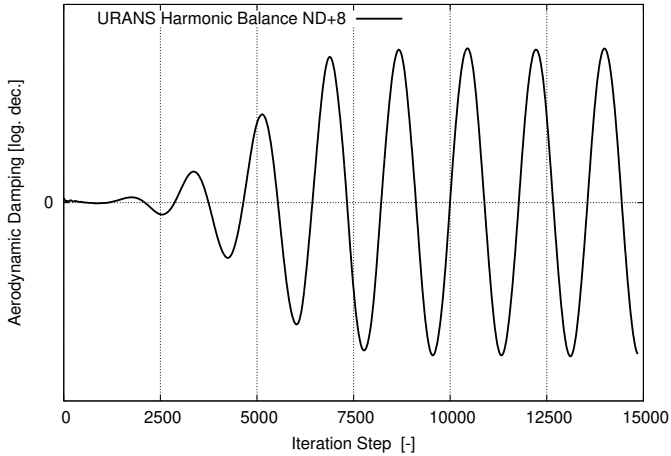

Figure 6.9.: CONVERGENCE HISTORY OF HB SIMULATION AT ND+8 WHILE RESOLVING UNSTEADY TURBULENCE.

flutter frequency itself is imposed in a non-negotiable fashion by the deformation of the underlying mesh. Therefore, an unsteady simulation based on an undeformed full-wheel mesh of the investigated stator row is performed while still prescribing time-invariant boundary conditions at the in- and the outlet of the computational domain. Since neither the boundary condition nor a deformation of the mesh force any transient response within the flow field, any observed unsteadiness can be considered as being self-induced and non-synchronous to the given rotational shaft speed.

The URANS problem is solved by relying on a time-integration method benefiting from a continuous resolution of the sampled bandwidth that is defined by the size of the applied time-stepping. A bandwidth of up to 30 [kHz] is resolved and tracked by an appropriate choice of point probes within the flow field. Turbulence is considered according to the performed flutter simulations employing Wilcox' k-ω two-equation model [68] and treating the flow as fully turbulent.

The result of the static pressure recorded by a point probe located at the

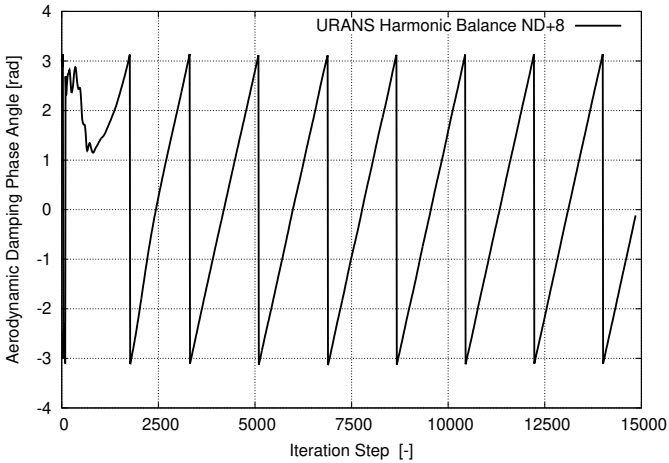

Figure 6.10.: CONVERGENCE HISTORY OF THE AERODYNAMIC DAMPING'S PHASE ANGLE AT ND+8.

stator midspan in the vicinity of the passage blocking shock at $\sim$ 70% chord length is displayed in Fig. 6.11. The fluctuation present in the point probe of interest is analysed by means of temporal fourier analysis and the results of the performed fast fourier transform (FFT) are plotted in Fig. 6.11 in the range of up to 3 [kHz]. The pressure fluctuations are normalised by the fluctuations observed at the flutter frequency of the converged evaluation of nodal diameter ND = +20.

The evaluation of the unsteadiness within the signal of the recorded point probe indicates distinct harmonic content at a frequency of 669.74 [Hz] and its associated higher harmonics. Furthermore, comparing the order of the detected pressure fluctuation to the fluctuations observed at the flutter frequency of nodal diameter ND = +20, the detected non-synchronous content appears to induce a fluctuation in an order of up to 14-times higher.

Recalling the assessed flutter frequency listed in Tab. 6.1, the second harmonic of the identified non-synchronous vibration (NSV) at 1339.47 [Hz] coincides with the third flutter harmonic confirming the observations held

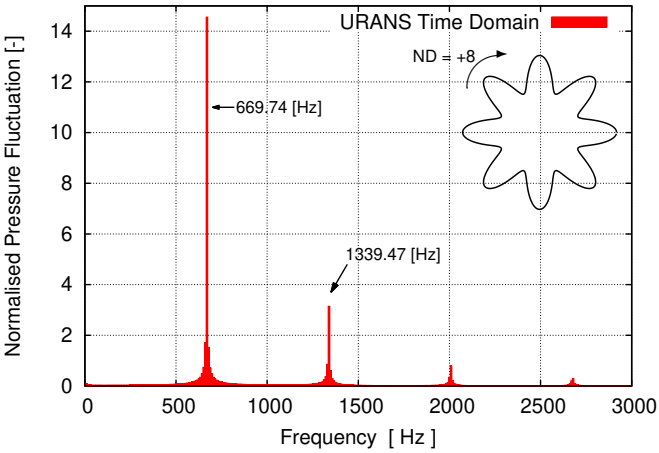

Figure 6.11.: FAST FOURIER TRANSFORM OF STATIC PRESSURE AT A RECORDED POINT PROBE UNDER STEADY BOUNDARY CONDITIONS AND UNDEFORMED MESH.

in the context of the Figs. 6.9 and 6.10 of poorly captured frequency content interfering with the assessed harmonics linked to the motion of flutter.

Circumferential analysis of the recorded data reveals a flow pattern established at the circumferential order of 8 traveling in negative circumferential direction. Recalling the notation of nodal diameter and IBPA from section 6.1, a propagation in negative circumferential direction corresponds to a positive nodal diameter in the flutter curve of Fig. 6.4. Hence, the detected flow instability can be linked with regard to its circumferential order, as well as its direction of circumferential propagation to the nodal diameter of ND = +8 of the flutter curve shown in Fig. 6.4.

The impact of the non-synchronous flow instability observed in Fig. 6.11 appears in a most distinct fashion in regions where the flow state is dominated by the transition from supersonic to subsonic flow conditions. The driving physical mechanism can be identified by an interaction between the passage blocking shock and a flow separation within the underlying boundary layer as displayed in Fig. 6.12. Focusing on the region on the stator suction

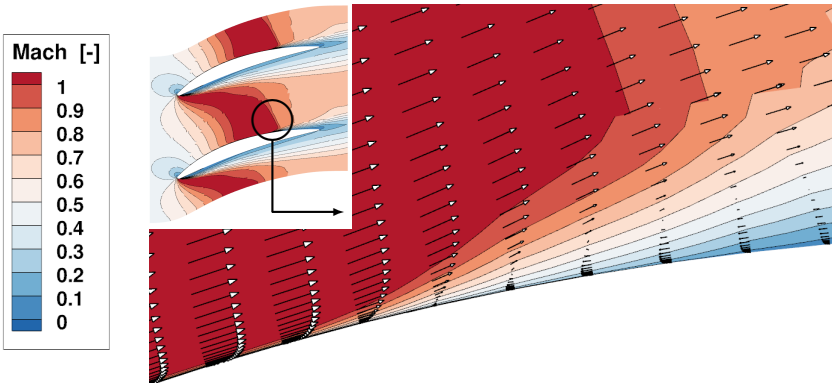

Figure 6.12.: LOCAL FLOW SEPARATION AT THE STATOR SUCTION SIDE IN THE PRESENCE OF THE PASSAGE BLOCKING SHOCK.

side where the flow is decelerated to a subsonic state, Fig. 6.12 highlights the shock position by a contour plot of the present Mach number which is superposed by the associated streamlines of the flow velocity that are tracked by properly scaled vectors.

At the supersonic region upstream of the shock position, the velocity profiles displayed in Fig. 6.12 are represented by the expected shape of a developed near wall viscous boundary layer. Due to the pressure gradient induced by the shock linked transition from super- to subsonic flow conditions that is acting against the main flow direction, the near wall boundary layer profiles increasingly suffer from the associated loss of momentum.

As a consequence, the separation of the boundary layer sets in once the axial position of the shock is surpassed causing a backflow regime within the boundary layer immediately adjacent to the shock condition in the main flow. The resulting flow separation leads to a local expansion of the boundary layer downstream of the shock as indicated in Fig. 6.12 by the increasing presence of low Mach conditions close to the wall.

The mutual interaction between the shock induced expansion of the boundary layer - throttling the capacity of the passage by reducing its cross-section available to the main flow - and the resulting instability forcing the shock to

Table 6.4.: SETTING PROPOSED FOR THE MISSING HB FLUTTER SIMULATIONS WHILE RESOLVING THE IDENTIFIED NSV CONTENT.

ND	Base Frequency	# Harmonics	IBPA
$+6 \leq \mathrm{ND} \leq +12$	$1/2 \cdot$ Flutter	0 1 2 3 4 5 6 7 8	$1/2 \cdot \left(\frac{2\pi \cdot \mathrm{ND}}{N_{\mathrm{Vanes}}} \right)$
ND = -8	$1/2 \cdot$ Flutter	0 1 2 3 4 5 6 7 8	0

alternate up- and downstream without finding a steady state of equilibrium is commonly denoted as shock wave boundary layer interaction (SWBLI).

The unsteadiness arising from SWBLI is still subject to ongoing research to the present day [102, 103, 104]. However, the dominating frequency identified in Fig. 6.11 is in accordance with the findings of [105, 106] and recently held by [107]. At this stage, the question arises of how to take advantage of the identified non-synchronous frequency content and finally enabling reliable results for what concerns the prediction of the aerodynamic damping for the nodal diameters missing in Fig. 6.4.

Since the FFT performed in Fig. 6.11 indicates the SWBLI frequency to appear at a factor of 1.5 of the assessed flutter frequency, an evaluation coupling the unsteadiness induced by both physical effects is proposed in Tab. 6.4. The base frequency of the shared harmonic set is chosen as half of the flutter frequency resolving the flutter frequency as the second and the identified SWBLI frequency as the third harmonic respectively. Their shared frequency ends up at the sixth harmonic of the common set and allows - in combination with the enabled coupling via the DC component - to consider the interference between both sources of unsteadiness by relying on the harmonic set approach pursued in this work.

However, recalling the previously stated observation of a propagation in negative circumferential direction of the non-synchronous flow instability, the solution approach proposed in Tab. 6.4 promises to deliver reliable

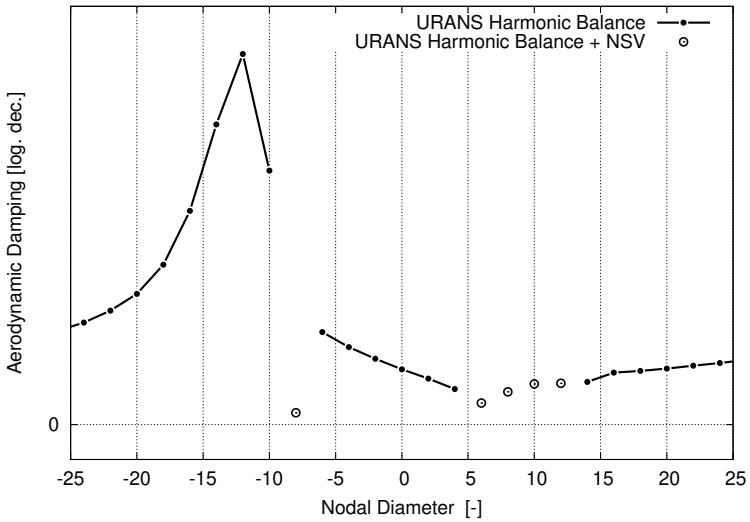

Figure 6.13.: PREDICTION OF TRANSONIC FLUTTER IN THE PRESENCE OF NON-SYNCHRONOUS FLOW INSTABILITIES.

results only for the positive nodal diameters in the range between $+6 \leq$ ND $\leq +12$. Therefore, for the missing nodal diameter of ND = -8, the approach to evaluate flutter based on a single passage mesh as shown in Fig. 6.1 is rejected and a multi-passage setting of vanishing impact of the employed IBPA approach is chosen. Obviously, this happens at the tremendous expense of the required computational effort and leads to a painful increase of the accounted run time.

All HB simulations consider turbulence in an unsteady fashion. Boundary conditions and mesh deformation are chosen in accordance with the simulations performed in the scope of section 6.3. The performed simulations converge while it has to be noticed that all simulations resolving the NSV in combination to the assessed flutter frequency suffer from a remaining oscillation of up to 5% around a converging mean value. The remaining oscillations though not amplified but constant around an invariant value hint at an improved but still imperfect consideration of the captured SWBLI

interference. However, recalling the challenging mechanisms superposed by the evaluated approaches, a remaining uncertainty in an order of lower than 5% is accepted at this stage.

The results of the respective approaches enabling the consideration of both flutter and NSV content are plotted in Fig. 6.13 by blanked dots. In addition to that, the flutter curve as introduced in the previous section 6.3 based on the HB simulations not explicitly resolving the content linked to SWBLI is added by a solid line.

The resulting aerodynamic damping for the nodal diameters in the range between $+6 \leq \mathrm{ND} \leq +12$ closes the gap in the region of missing nodal diameters by a continuous extension of the NSV unaffected flutter curve. The results generated by the superposition of the identified NSV are of same order as the adjacent nodal diameters of $\mathrm{ND} = +4$ and $\mathrm{ND} = +14$ and indicate flutter stability by positive values of the assessed aerodynamic damping.

The aerodynamic damping at the negative nodal diameter of $\mathrm{ND} = -8$ predicts flutter stability as well by indicating a positive damping of same order as observed for the NSV affected nodal diameters in the range between $+6 \leq \mathrm{ND} \leq +12$. However, compared to the adjacent nodal diameters of the flutter curve at $\mathrm{ND} = -10$ and $\mathrm{ND} = -6$, a substantial gap can be observed highlighting the impact of the interference with the identified SWBLI for this nodal diameter. In the presence of the SWBLI propagating at the same nodal diameter - though in reverse circumferential direction - the available aerodynamic damping is reduced substantially. The results shown in Fig. 6.13 indicate that adjacent nodal diameters are not affected if the direction of the circumferential propagation is opposite. However, this has to be confirmed by according multi-passage flutter simulations of the respective nodal diameters of $\mathrm{ND} = -10$ and $\mathrm{ND} = -6$ which is ongoing research.

The gap in the flutter curve in the range between $+6 \leq \mathrm{ND} \leq +12$ closed by the consideration of the identified NSV indicates a lock-in of the SWBLI to adjacent nodal diameters of flutter if their circumferential propagation coincides. Accordingly, a wider range of the flutter curve is affected which is expressed by lower values of the predicted aerodynamic damping. In order to

Table 6.5.: AVERAGED NUMERICAL EFFORT OF THE TRANSONIC SOLUTION APPROACHES, MEASURED IN REQUIRED CPU HOURS.

URANS HB	URANS HB + NSV	URANS HB + NSV (multi passage)
360 [CPUh]	1100 [CPUh]	15 000 [CPUh]

confirm the indicated lock-in behaviour, the flutter curve stressed above needs to be supported by results of according time-integration simulations serving as numerical benchmark references. This requires a large number of unsteady full-wheel simulations performed in the time domain taking into account the mesh deformation of the associated nodal diameters. Nevertheless, the HB results presented in this section would benefit from the additional numerical validation based on the results of a flutter curve generated by full-wheel time domain simulations which is still ongoing research as well.

Comparing the numerical effort of the respective solution approaches displayed in Fig. 6.13, the required CPU hours are listed in Tab. 6.5. Obviously, the cheapest approach is the HB method resolving only 4 harmonics of the flutter deformation as initially proposed in section 6.1. By increasing the resolved harmonic content to 8 harmonics of half the flutter frequency and superposing the NSV content, the numerical effort appears to be three times higher. The additional numerical effort is linked to the increased number of harmonics and a higher number of required iterations to reach a satisfying level of convergence.

Finally, the approach employed in order to evaluate the nodal diameter of ND = -8 by relying on a multi passage configuration requires computational efforts overshooting any order that can be justified for the application in an industrial environment. Even for the single passage approach applied to the nodal diameters at $+6 \leq ND \leq +12$, the industrial benefit remains questionable since the NSV frequency has to be known in advance and in general, it can not be expected to appear at the convenient ratio to the

assessed harmonic content as observed in this chapter.

However, the capability to reproduce the interaction between several sources of flow instability by relying on a frequency domain method can be demonstrated though requires further validation. Furthermore, a clear indicator of unresolved harmonic content interfering with the considered frequencies during the solution process can be given by the analysis discussed in Fig. 6.10 and the work of [58]. If the present frequency content can be identified and considered during the solution process properly, results can be generated suffering from an uncertainty in an order of lower than 5%. In order to achieve this, the reliable consideration of unsteady turbulence effects is mandatory and must not be neglected.

6.5. Conclusion

In the scope of this chapter, the impact of unsteady turbulence effects is discussed for both subsonic and transonic flutter by numerical means. A compressor stator vane is investigated under subsonic and transonic flow conditions and its flutter stability is evaluated based on the prediction of the associated aerodynamic damping.

In the case of subsonic flutter, the impact of unsteady turbulence effects is found to be of negligible order, in particular if related to the required numerical effort compared to a conventional linearised approach. In contrast to this, the results discussed in section 6.3 question the application of the established linearised approach to transonic flows in general. For this kind of flow situation, the incomplete expansion around the steady RANS state as well as the lack of a time-linearised turbulence model limit the quality of this approach in an unacceptable order if applied to the investigated transonic flow situation.

For what concerns transonic flutter, the consideration of turbulence in an unsteady and non-linear fashion is identified as key. Consideration of the unteadiness within the employed turbulence model does not only allow to provide results of higher quality, it is identified in the investigated case to be

the main driver allowing to resolve the unsteady effects being necessary to provide results of sufficient quality and numerical stability.

Furthermore, the capability of the discussed Harmonic Balance approach to reproduce the interaction of flutter and SWBLI induced flow instabilities is discussed if turbulence is considered in an unsteady fashion. The results are supported by results of a time-integration method performed on an undeformed mesh though the observed lock-in behaviour needs additional validation which is ongoing research. An appropriate indicator for the presence of relevant unresolved harmonic content affecting the convergence behaviour is proposed and a general concept to handle interfering non-synchronous flow instabilities is formulated though its benefit in practice if applied in an industrial environment remains to be proved at this stage.

Chapter 7

Conclusion and Perspectives for Future Work

7.1. Conclusion

The main goal of the presented research effort is to provide an enhanced level of robustness for a Harmonic Balance solver if turbulence is taken into account in an unsteady fashion. As a result of the conducted studies, a leading source reducing the computational robustness is identified by the Gibbs phenomenon. Undershoots linked to the Gibbs induced ringing result in unfeasible levels of turbulence quantities. The turbulence kinetic energy k and dissipation rate ω, for instance, are locally predicted to become negative.

The application of a limiter imposing very low non-negative turbulence levels instead is in most cases not capable of catching this deficit. In addition to that, relying on a hard-coded limiter functionality is inconsistent to the underlying physics and there is no way to control or even estimate the induced error.

An elegant alternative to overcome these instabilities is found in this work by a reformulation of the truncated inverse Fourier transform. The reformulated problem is equivalent to a convolution of the time-signal with a rect-based filter kernel and therefore coincides with the application of a sinc-based filter in the frequency domain. The filter has been implemented in the source code of the flow solver TRACE and its impact on the solution

behaviour has been investigated. The application of this Lanczos-type filter method on turbulence quantities is found to increase both the numerical robustness and stability while avoiding an increase of the overall runtime.

However, the application of the Lanczos-filter method requires the consideration of at least two harmonics of the underlying base frequency. By resolving exclusively the frequency of aeromechanic interest - which is equivalent to a bandpass filter eliminating any remaining unsteadiness in the first place - there is no spectrum left for an additional Lanczos-filtering. Taking into account a minimum of three higher harmonics of the frequency of aeroelastic interest is recommended. If only one harmonic can be taken into account, approaches based on a logarithmic formulation of the turbulence dissipation rate ω, as proposed for instance by [108, 109], may help.

As a consequence of Parseval's theorem, any filter-induced deviation from the representation of the Fourier-series increases the global error of the solution. As to what extent the error induced by a filtering of turbulence can be accepted has to be checked for the respective application. Therefore, a major objective of this research consists in a thorough validation of the developed Lanczos-filtered HB method. This is achieved by relying on measurement data as well as on high-resolved numerical simulations.

The validation assesses first the capability of the Lanczos-filtered HB method to predict the unsteady transition behaviour. This is demonstrated for a modern LPT stator surface equipped with a thin film constant temperature anemometer. The HB solver relying on the Lanczos-filtered turbulence model is able to reproduce the alternating transition behaviour according to the measurement. However, the same level of accuracy as it is provided by the results of the numerical benchmark relying on a high-resolved time-integration method can not be achieved. Analysis of the underlying frequency spectra show that there is a massive bandwidth of frequencies affecting the unsteady transition within the LPT rig. Consequently, a frequency domain solver can not be expected to perform as competitive as a time-integration method if very detailed knowledge of the unsteady boundary layer behaviour is required.

A second validation step focuses on the prediction of the aerodynamic excitation by the Lanczos-filtered HB method. This is achieved by comparing the results to pressure fluctuations measured by fast response pressure transducers mounted within a LPT cascade. The application of the implemented Lanczos-filter allows to improve the simulation quality significantly by taking into account the behaviour of unsteady turbulence. This is supported by numerical results of a HB method solving only for the temporal average of turbulence and a high-resolved time integration benchmark.

However, in regions where the appearance of pressure fluctuations is dominated by the unsteady behaviour of boundary layer transition, the Lanczos-filtered HB method is locally not capable of providing predicitions of same quality as can be obtained by the time-integration benchmark. This is linked to an insufficient capturing of the alternating transition mechanisms acting within the boundary layer of the measured LPT cascade. Nevertheless it should be kept in mind, that - if compared to the deviations to the measurement data - the differences between the HB and time-integration method are not of major order there.

Relying on the provided validation of the filter, a second major research objective is the assessment of the impact of unsteady turbulence on the prediction of aeroelastic key quantities. For this purpose, numerical studies predicting the aerodynamic forced response excitation and the aerodynamic damping are carried out. Both aspects are investigated for sub- and transonic flows.

The following numerical methods are discussed to achieve this task: a time-linearised method, a Harmonic Balance method relying on a Lanczos-filtered model of unsteady turbulence, a Harmonic Balance method considering only an update of the temporal average of turbulence and a method relying on a highly resolved time-integration scheme.

The time-linearised method provides fast information of the flow field at the frequency of interest at low computational costs. Therefore, it represents the industrial standard for lots of aeroelastic design tasks. However, it suffers from the following drawbacks: no update of the temporal mean compared to

the steady RANS state, limitation to single-row-single-passage configurations, no consideration of nonlinear effects and no update of the eddy viscosity which is kept frozen at its steady state.

The Harmonic Balance method resolving the unsteadiness of turbulence by relying on the proposed Lanczos-filter method promises to reduce all of the mentioned limitations of the time-linearised method. However, this happens at the expense of additional computational efforts. Therefore, as to what extent the Lanczos-filtered Harmonic Balance method is able to provide predictions of higher quality when compared to the time-linearised standard is assessed for the respective aeromechanic tasks.

The Harmonic Balance method updating only the temporal average of turbulence allows to estimate the impact of the unsteadiness of turbulence on the results of aeromechanic interest. For this research, this is the main intention of this approach.

Finally, the predictions generated by the time-integration method serve as a numerical benchmark for the above mentioned solution methods. It is by far the most costly method but delivers the results of highest quality due to its highly and continuously resolved frequency spectrum. The high computational costs make it an unattractive choice as industrial standard given the massive number of aeromechanic evaluations that have to performed in industrial design.

Comparing the results of the respective methods allows to provide an estimator of the limitations of each approach as well as to assess for which aeroelastic design task resolving unsteady turbulence matters.

Focusing on the prediction of the aerodynamic excitation first, results for both subsonic and transonic flows are discussed by evaluating the forced response excitation of modern LPT and HPC rotor blades. In both cases, the Lanczos-filtered HB approach reduces substantially the gap between the time-integration benchmark and the HB method based on time-averaged turbulence. The accuracy of the predicted generalised force improves in an order of $\sim$10% for the subsonic case and of $\sim$5% for the transonic case, respectively. The highest deviations can be observed for the time-linearised approach, in particular in the shock-dominated regions of the HPC blade.

Furthermore, the prediction of the aerodynamic damping for flutter applications is investigated for a modern HPC stator vane. By evaluating different throttle conditions at the same rotational shaft speed, both subsonic and transonic flow states can be assessed. Again, the results obtained from solution approaches relying on a varying degree of resolved turbulence are compared. In addition to the HB approaches either resolving or averaging unsteady turbulence, results based on temporal linearisation around the steady RANS state are discussed.

In the case of subsonic flutter, the linearised approach benefiting from lowest numerical requirements and run times is able to reproduce the subsonic flutter behaviour in an equivalent manner to the HB method based on averaged turbulence. Solving the turbulence equations in an unsteady framework during the HB approach is considered here to deliver results of highest quality and reveals deviations in an order of $\sim$10%.

Focusing on the prediction of transonic flutter, the linearised as well as the HB method averaging unsteady turbulence fail. At the investigated throttle condition, the presence of turbulence driven flow instabilities interfering at the considered flutter frequency requires the consideration of turbulence in an unsteady fashion.

In this research, the results of one LPT and two HPC configurations are discussed in terms of an aeroelastic design process. Since a major bottleneck in aeroelastic design consists in the massive number of performance points that have to be assessed, the results of this work have to be discussed without any claim of completeness. The results demonstrate rather a potential benefit than a guaranteed one. More experience with the developed method is required before a generalisation of the found benefits can be stated.

Nevertheless, this thesis recommends to change the standard course of action for the evaluation of the aerodynamic damping at transonic flow conditions, in particular for the evaluation of flutter. For these flows and design tasks, the consideration of the impact of unsteady turbulence is found to be mandatory.

From an industrial point of view, the research objective of highest interest may consist in a discussion of a potential enhancement of the established aeroelastic design process. Apart from offering substantial benefits when applied to transonic flows, not only the quality but also the associated computational effort has to be taken into account to address this objective.

Compared to the so far established methods based on temporal linearisation around the single-row-single-passage RANS state, the HB method offers various advantages with the consideration of unsteady turbulence being only one important to name. Additional assets are given for instance by the capability to consider the interaction with adjacent stages and passages - in particular if acoustically driven - as well as to consider an update of the temporal mean and the impact of nonlinear effects. The ability to include all these additional excitation mechanisms and high-order contributions comes at a price. The required computational effort of the HB method appears to be in an order of ∼100 times of the established linearised methods. As a result of the chapters 5 and 6, this effort needs to be invested at least to obtain results of higher quality if compared to aeroelastic predictions in the past. However, the cheap access to computing power nowadays justifies to do so.

Compared to expensive simulations based on the time-integration method, relying on the HB method allows to reduce both overall run-time and required CPU-hours substantially. The amount of accessed CPU-hours appears to be ∼100 times lower for the HB simulations given the fact that real engine configurations often force simulations of the full annulus if performed in the time domain alone. Given the speed-up by a factor of ∼100 while providing results of comparable accuracy, relying on the HB method and resolving the unsteadiness by applying a Lanczos-filtered turbulence model provides a suitable compromise between numerical efficiency and results of high quality.

7.2. Perspectives for Future Work

The presented thesis relies on a Lanczos-filtered turbulence model in order to alleviate the negative impact of the Gibbs phenomenon on the computational robustness of the flow solver. However, other numerical means promising an increased level of numerical robustness consist in logarithmic formulations of the turbulence dissipation rate ω, as proposed for instance by [108, 109].

The logarithmic reformulation of the transport equation of the turbulence dissipation rate ω avoids negative undershoots for this quantity. Potential undershoots of the turbulence kinetic energy k remain, however, unaffected by this approach. If the same order of robustness can be achieved for turbomachinery flows by this model has therefore to be assessed carefully.

While in general the capability to reproduce the unsteady transition behaviour has been shown in chapter 3, the results presented in chapter 4 indicate severe limitations in the prediction of the transition point if a correlation based transition model as [18] is used. However, the transition model proposed by [18] provides to the present day for many LPT applications the only choice reflecting the respective transition modes at all. In order to further improve the capability of the assessed HB solver to predict the aerodynamic excitation, the correlation-based transition model has to be refitted to frequency domain applications. In particular, the information about the unsteady transition has to be communicated to subsequent iteration steps in order to improve the convergence quality.

For what concerns the prediction of flutter, the results presented in 6.4 raise the question of how reliable the appearance of non-synchronous flow instabilites can be reproduced in general. The presented results for the interaction with SWBLI-driven flow instabilities have to be confirmed for other NSV mechanisms. However, the results stress that turbulence driven non-synchronous flow instabilities are highly sensitive to an accurate consideration of turbulence and demand turbulence to be considered in an unsteady fashion.

Next steps consist therefore in a deeper analysis of the HB solver's capability to predict non-synchronous flow instabilities. The indicated lock-in

behaviour needs additional validation by according time-integration simulations. In addition to that, the impact of non-linear effects on the transonic NSV-interference is not sufficiently discussed. Recent studies [110] report the potential of linearised methods for NSV-applications. For the assessed SWBLI-instability, the evaluation of a setup based on a linearised turbulence model promises to yield a first hint in that regard.

A linearised consideration of the turbulence model will however cause new problems. The Lanczos-filter method discussed in this work is not meaningful to applications that are truncated after the leading beat frequency. This may require alternative stabilisation measures for the turbulence model if the above mentioned logarithmic formulations fail as well.

In any case, by increasing the impact of unsteady turbulence effects, the question about the reliability of the employed turbulence models arises inevitably at this stage. Since the needs met in the context of an industrial design framework require the application of RANS-models in a non-negotiable fashion, and since the capability of these models to reproduce the chaotic behaviour of turbulence is limited to the present day, a final solution to these challenges in the future remains open.

Accordingly, it has to be checked carefully if the application of the employed RANS-models is feasible for these kinds of flows. Only by experiments and reliable measurements it is possible to assess the validity extent of the turbulence models and, if necessary, how the RANS-models can be calibrated properly.

Bibliography

[1] FlightGlobal, 2018. "A320neo operators affected by PW1100G vibration issue". In https://www.flightglobal.com/engines/a320neo-operators-affected-by-pw1100g-vibration-issue/129485.article. visited 2021.07.13.

[2] Aviationweek, 2018. "Airbus Stops Taking PW1100G Engines". In https://aviationweek.com/air-transport/airbus-stops-taking-pw1100g-engines. visited 2021-07-13.

[3] Marshall, J., and Imregun, M., 1996. "A review of aeroelasticity methods with emphasis on turbomachinery applications". *Journal of Fluids and Structures,* ***10***(3), pp. 237–267.

[4] Srinivasan, A. V., 1997. "Flutter and Resonant Vibration Characteristics of Engine Blades". *Journal of Engineering for Gas Turbines and Power,* ***119***(4), pp. 742–775.

[5] Platzer, M.F. and Carta, F.O., 1987. "AGARD Manual on Aeroelasticity in Axial-flow Turbomachines: Structural dynamics and aeroelasticity". In AGARD Manual on Aeroelasticity in Axial-flow Turbomachines. North Atlantic Treaty Organization, Advisory Group for Aerospace Research and Development.

[6] Tyler, J., and Sofrin, T., 1962. *Axial Flow Compressor Noise Studies*. SAE technical paper series. SAE International.

[7] Whitehead, D., 1973. "The effect of compressibility on unstalled torsion flutter". *University of Cambridge Engineering Department, Cambridge, UK*. CUED/A-Turbo/TR-51-1973.

[8] Lieblein, S., Schwenk, F., and Broderick, R., 1953. "Diffusion Factor for Estimating Losses and Limiting Blade Loading in Axial-Flow-Compressor Blade Elements". *NACA Research Memorandum*. E53D01.

[9] Koch, C., and Smith, L., 1976. "Loss Sources and Magnitudes in Axial Compressors". *ASME J. Eng. Power,* ***98***, pp. 611–424.

[10] De Haller, P., 1953. "Das Verhalten von Tragflügelgittern in Axialverdichtern und im Windkanal". *Brennstoff-Wärme-Kraft (BWK),* ***5***(333), p. 24.

[11] Meauze, G., 1989. "Overview of Blading Design Methods". In AGARD Lecture Series. No. 167.

[12] Halstead, D., Wisler, D., Okiishi, T., Walker, G., Hodson, H., and Shin, H., 1997. "Boundary Layer Development in Axial Compressors and Turbines: Part 1 of 4 - Composite Picture". *ASME J. Turbomach.,* ***119***(1), pp. 114–127.

[13] Halstead, D., Wisler, D., Okiishi, T., Walker, G., Hodson, H., and Shin, H., 1997. "Boundary Layer Development in Axial Compressors and Turbines: Part 2 of 4 - Compressors". *ASME J. Turbomach.,* ***119***(3), pp. 426–444.

[14] Halstead, D., Wisler, D., Okiishi, T., Walker, G., Hodson, H., and Shin, H., 1997. "Boundary Layer Development in Axial Compressors and Turbines: Part 3 of 4 - LP Turbines". *ASME J. Turbomach.,* ***119***(2), pp. 225–237.

[15] Halstead, D., Wisler, D., Okiishi, T., Walker, G., Hodson, H., and Shin, H., 1997. "Boundary Layer Development in Axial Compressors and Turbines: Part 4 of 4 - Computations and Analyses". *ASME J. Turbomach.,* ***119***(1), pp. 128–139.

[16] Praisner, T., and Clark, J., 2007. “Predicting Transition in Turbomachinery - Part I: A Review and New Model Development”. *ASME J. Turbomach.,* ***129***(1), pp. 1–13.

[17] Praisner, T., Grover, E., Rice, M., and Clark, J., 2007. “Predicting Transition in Turbomachinery - Part II: Model Validation and Benchmarking”. *ASME J. Turbomach.,* ***129***(1), pp. 14–22.

[18] Kozulovic, D., Röber, T., and Nürnberger, D., 2007. “Application of a multimode transition model to turbomachinery flows”. In Proceedings of Seventh European Turbomachinery Conference, pp. 1369–1378.

[19] Biester, M. H.-O., Henke, M., Gündogdu, Y., Engel, K., and Seume, J., 2012. “Unsteady Wake-Blade Interaction: A Correlation between Surface-Pressure Fluctuations and Loss Generation”. In Proceedings of ASME Turbo Expo 2012. GT2012-69616.

[20] Menter, F., Langtry, R., Likki, S., Suzen, Y., Huang, P., and Voelker, S., 2004. “A Correlation-Based Transition Model Using Local Variables - Part 1: Model Formulation”. In Proceedings of ASME Turbo Expo 2004. GT2004-53452.

[21] Langtry, R., and Menter, F., 2009. “Correlation-Based Transition Modeling for Unstructured Parallelized Computational Fluid Dynamics Codes”. *AIAA Journal,* ***47***(12), pp. 2894–2906.

[22] Langtry, R., 2006. “A correlation-based transition model using local variables for unstructured parallelized CFD codes”. PhD Thesis, University of Stuttgart, Stuttgart, Germany.

[23] Müller, C., Herbst, F., Fiala, A., Zscherp, C., Kügeler, E., and Seume, J., 2015. “Parameter Study for an Improved Prediction of Wake-Induced Transition in Low-Pressure Turbines”. In Proceedings of 11th Int. Gas Turbine Congress (IGTC), Tokyo. IGTC2015-0043.

[24] Whitehead, D., 1960. “Force and moment coefficients for vibrating aerofoils in cascade”. *H.M. Stationery Office*. ARC-22133.

[25] Smith, S., 1973. “Discrete frequency sound generation in axial flow turbomachines”. *Aeronautical Research Council Reports and Memoranda*. H.M. Stationery Office.

[26] Whitehead, D., 1982. “The calculation of steady and unsteady transonic flow in cascades”. *University of Cambridge Engineering Department, Cambridge, UK*. CUED/A-Turbo/TR.

[27] Verdon, J., and Caspar, J., 1984. “A linear aerodynamic analysis for unsteady transonic cascades”. *National Aeronautics and Space Administration, Scientific and Technical Information Branch*. NASA contractor report.

[28] Ni, R., 1974. “Nonstationary aerodynamics of arbitrary cascades in compressible flow”. PhD Thesis, Stevens Institute of Technology, Hoboken, NJ, USA.

[29] Hall, K., 1987. “A linearized Euler analysis of unsteady flows in turbomachinery”. PhD Thesis, Massachusetts Institute of Technology, Cambridge, MA, USA.

[30] Holmes, D. G., and Chuang, H. A., 1993. “2D Linearized Harmonic Euler Flow Analysis for Flutter and Forced Response”. In Unsteady Aerodynamics, Aeroacoustics, and Aeroelasticity of Turbomachines and Propellers, H. M. Atassi, ed., Springer New York, pp. 213–230.

[31] Kahl, G., and Klose, A., 1993. “Computation of Time Linearized Transonic Flow in Oscillating Cascades”. In Proceedings of ASME Turbo Expo 1993. 93-GT-269.

[32] Holmes, D., and Lorence, C., 1998. “Three Dimensional Linearized Navier-Stokes Calculations for Flutter and Forced Response”. In Unsteady Aerodynamics and Aeroelasticity of Turbomachines, T. H. Fransson, ed., Springer Netherlands, pp. 211–224.

[33] Hall, K., and Lorence, C., 1993. “Calculation of Three-Dimensional Unsteady Flows in Turbomachinery Using the Linearized Harmonic

Euler Equations". *ASME Journal of Turbomachinery,* ***115***(4), pp. 800–809.

[34] Giles, M., 1988. "Calculation of unsteady wake/rotor interactions". *Journal of Propulsion and Power,* ***4***(4), pp. 356–362.

[35] He, L., 1990. "An Euler Solution for Unsteady Flows Around Oscillating Blades". *ASME Journal of Turbomachinery,* ***112***(4), pp. 714–722.

[36] Ott, P., 1991. "Oszillierender senkrechter Verdichtungsstoss in einer ebenen Düse". PhD Thesis, Ecole Polytechnique Federale de Lausanne, Lausanne, Switzerland.

[37] Vahdati, M., Zhao, F., and Sureshkumar, P., 2020. "An Overview of Time-Domain Computational Methods for Aeroelastic Instabilities of Multi-Stage Compressors". *Journal of the Global Power and Propulsion Society,* ***4***, pp. 114–127.

[38] He, L., and Ning, W., 1998. "Efficient Approach for Analysis of Unsteady Viscous Flows in Turbomachines". *AIAA Journal,* ***36***(11), pp. 2005–2012.

[39] Hall, K., Thomas, J., and Clark, W., 2002. "Computation of Unsteady Nonlinear Flows in Cascades Using a Harmonic Balance Technique". *AIAA Journal,* ***40***(5), pp. 879–886.

[40] McMullen, M., 2003. "The Application of Non-Linear Frequency Domain Methods to the Euler and Navier-Stokes Equations". PhD Thesis, Stanford University, Stanford, USA.

[41] Frey, C., Ashcroft, G., Kersken, H., and Voigt, C., 2014. "A Harmonic Balance Technique for Multistage Turbomachinery Applications". In Proceedings of ASME Turbo Expo 2014. GT2014-25230.

[42] Vasanthakumar, P., 2003. "Three dimensional frequency-domain solution method for unsteady turbomachinery flows". PhD Thesis, Durham University, Durham, UK.

[43] Gopinath, A., and Jameson, A., 2005. "Time spectral method for periodic unsteady computations over two- and three- dimensional bodies". In Proceedings of 43rd AIAA Aerospace Sciences Meeting and Exhibit.

[44] Ekici, K., and Hall, K. C., 2008. "Nonlinear frequency-domain analysis of unsteady flows in turbomachinery with multiple excitation frequencies". *AIAA Journal,* ***46***(8), pp. 1912–1920.

[45] He, L., 2008. "Harmonic solution of unsteady flow around blades with separation". *AIAA Journal,* ***46***(6), pp. 1299–1307.

[46] Sicot, F., Puigt, G., and Montagnac, M., 2008. "Block-Jacobi Implicit Algorithms for the Time Spectral Method". *AIAA Journal,* ***46***(12), pp. 3080–3089.

[47] Subramanian, V., Custer, C., Weiss, J., and Hall, K., 2011. "Simulation of Unsteady Turbomachinery Flows Using an Implicitly Coupled Nonlinear Harmonic Balance Method". In Proceedings of ASME Turbo Expo 2011. GT2011-46367.

[48] McMullen, M., Jameson, A., and Alonso, J., 2006. "Demonstration of Nonlinear Frequency Domain Methods". *AIAA Journal,* ***44***(7), pp. 1428–1435.

[49] Ekici, K., and Hall, K., 2007. "Nonlinear analysis of unsteady flows in multistage turbomachines using the harmonic balance technique". *AIAA Journal,* ***45***(5), pp. 1047–1057.

[50] Gopinath, A., van der Weide, E., Alonso, J., Jameson, A., Ekici, K., and Hall, K., 2007. "Three-dimensional unsteady multi-stage turbomachinery simulations using the harmonic balance technique". In Proceedings of 45th AIAA Aerospace Sciences Meeting and Exhibit.

[51] Sicot, F., Dufour, G., and Gourdain, N., 2011. "A Time-Domain Harmonic Balance Method for Rotor/Stator Interactions". *ASME Journal of Turbomachinery,* ***134***(1).

[52] Subramanian, V., Custer, C., Weiss, J., and Hall, K., 2013. "Unsteady Simulation of a Two-Stage Cooled High Pressure Turbine Using an Efficient Non-Linear Harmonic Balance Method". In Proceedings of ASME Turbo Expo 2013. GT2013-94574.

[53] Junge, L., Ashcroft, G., Jeschke, P., and Frey, C., 2015. "On the application of frequency-domain methods to multistage turbomachinery". In Proceedings of ASME Turbo Expo 2015. GT2015-42936.

[54] Heners, J., Müller-Schindewolffs, C., Vogt, D., and Blum, F., 2020. "Prediction of the Unsteady Transition Behavior in Low Pressure Turbine Flows Using Time and Frequency Domain Methods". In Proceedings of ASME Turbo Expo 2020. GT2020-14257.

[55] Heners, J. P., Stotz, S., Krosse, A., Korte, D., Beck, M., and Vogt, D., 2021. "Prediction of transient pressure fluctuations within a low-pressure turbine cascade using a lanczos-filtered harmonic balance method". *International Journal of Turbomachinery, Propulsion and Power,* ***6***(3).

[56] Guedenuy, T., Gomar, A., Gallard, F., Sicot, F., Dufour, G., and Puigt, G., 2013. "Non-Uniform Time Sampling for Multiple-Frequency Harmonic Balance Computations". *Jour. Comp. Physics,* ***236***, pp. 317–345.

[57] Junge, L., Frey, C., Ashcroft, G., and Kügeler, E., 2020. "A New Harmonic Balance Approach Using Multidimensional Time". In Proceedings of ASME Turbo Expo 2020. GT2020-16224.

[58] Kielb, R., Hall, K. C., Spiker, M. A., and Thomas, J., 2006. "Non-Synchronous Vibration of Turbomachinery Airfoils". Technical Report, Duke University: Department of Mechanical Engineering and Materials Science, Durham, NC, USA.

[59] Clark, S., 2013. "Design for Coupled-Mode Flutter and Non-Synchronous Vibration in Turbomachinery". PhD Thesis, Duke University, Durham, NC, USA.

[60] Ashcroft, G., Frey, C., and Kersken, H., 2014. “On the Development of a Harmonic Balance Method for Aeroelastic Analysis”. In Proceedings of Sixth European Conference on Computational Fluid Dynamics (ECCOMAS CFD).

[61] Frey, C., Ashcroft, G., and Kersken, H., 2015. “Simulations of Unsteady Blade Row Interactions Using Linear and Non-Linear Frequency Domain Methods”. In Proceedings of ASME Turbo Expo 2015. GT2015-43453.

[62] Kersken, H., Frey, C., and Ashcroft, G., 2017. “Flutter Analysis of an Embedded Blade Row with a Harmonic Balance Solver”. In Proceedings of 12th Europ. Conf. Turbomach. Fluid. Dyn. ETC2017-238.

[63] Heners, J., Vogt, D., Frey, C., and Ashcroft, G., 2019. “Investigation of the Impact of Unsteady Turbulence Effects on the Aeroelastic Analysis of a Low-Pressure Turbine Rotor Blade”. *ASME J. Turbomach.,* ***141***(10), p. 100801.

[64] Sanders, C., Terstegen, M., Jeschke, P., Schoenenborn, H., and Heners, J., 2019. “Rotor–Stator Interactions in a 2.5-Stage Axial Compressor—Part II: Impact of Aerodynamic Modeling on Forced Response”. *ASME J. Turbomach.,* ***141***(10), p. 101008.

[65] Frey, C., Ashcroft, G., and Kersken, H., 2015. “Simulations of Unsteady Blade Row Interactions Using Linear and Non-Linear Frequency Domain Methods”. In Proceedings of ASME Turbo Expo 2015. GT2015-43453.

[66] Geiser, G., Wellner, J., Kügeler, E., Weber, A., and Moors, A., 2019. “On the Simulation and Spectral Analysis of Unsteady Turbulence and Transition Effects in a Multistage Low Pressure Turbine”. *ASME J. Turbomach.,* ***141***(5), p. 051012.

[67] Kügeler, E., Geiser, G., Wellner, J., Weber, A., and Moors, A., 2018. “On the Simulation of Unsteady Turbulence and Transition Effects in

a Multistage Low Pressure Turbine, Part III: Comparison of Harmonic Balance and Full Wheel Simulation". In Proceedings of ASME Turbo Expo 2018. GT2018-76749.

[68] Wilcox, D., 1988. "Reassessment of the Scale-Determining Equation for Advanced Turbulence Models". *AIAA Journal,* ***26***(11), pp. 1299–1310.

[69] Becker, K., Heitkamp, K., and Kügeler, E., 2010. "Recent Progress in a Hybrid-Grid CFD Solver for Turbomachinery Flows". In Proceedings of Fifth European Conference on Computational Fluid Dynamics (ECCOMAS CFD). 01609.

[70] Kügeler, E., Weber, A., Nürnberger, D., and Engel, K., 2008. "Influence of Blade Fillets on the Performance of a 15 Stage Gas Turbine Compressor". In Proceedings of ASME Turbo Expo 2008. GT2008-50784.

[71] Geiser, G., Wellner, J., Kügeler, E., Weber, A., and Moors, A., 2018. "On the Simulation of Unsteady Turbulence and Transition Effects in Multistage Low Pressure Turbine, Part II: Full-Wheel Simulation". In Proceedings of ASME Turbo Expo 2018. GT2018-76764.

[72] van Leer, B., 1979. "Towards the ultimate conservative difference scheme. V-A second-order sequel to Godunov's method". *J. of Comp. Physics,* ***32***(1), pp. 101–136.

[73] van Albada, G., van Leer, B., and Roberts Jr., W., 1982. "A comparative study of computational methods in cosmic gas dynamics". *Astronomy and Astrophysics,* ***28***(12), pp. 2050–2058.

[74] Franke, M., Röber, T., Kügeler, E., and Ashcroft, G., 2010. "Turbulence Treatment in Steady and Unsteady Turbomachinery Flows". In Proceedings of Fifth European Conference on Computational Fluid Dynamics (ECCOMAS CFD). 01628.

[75] Giles, M., 1990. "Nonreflecting boundary conditions for Euler equation calculations". *AIAA Journal,* ***28***(12), pp. 2050–2058.

[76] Schlüß, D., Frey, C., and Ashcroft, G., 2016. "Consistent non-reflecting boundary conditions for both steady and unsteady flow simulations in turbomachinery applications". In Proceedings of Seventh European Conference on Computational Fluid Dynamics (ECCOMAS CFD).

[77] Kersken, H., Ashcroft, G., Frey, C., Wolfrum, N., and Korte, D., 2014. "Non-reflecting boundary conditions for aeroelastic analysis in time and frequency domain 3D RANS solvers". In Proceedings of ASME Turbo Expo 2014. GT2014-25499.

[78] Papoulis, A., 2018. *Signal Analysis*, Reprint ed. Dover Books on Electrical Engineering. Dover Publications, Inc., New York, USA.

[79] Lanczos, C., 1988. *Applied Analysis*, Reprint ed. Dover Publications Inc., New York, USA, ch. 4, pp. 219–229.

[80] Duchon, C. E., 1979. "Lanczos Filtering in One and Two Dimensions". *J. Appl. Meteorol.,* ***18***(8), pp. 1016–1022.

[81] Djeddi, R., and Ekici, K., 2016. "Resolution of Gibbs phenomenon using a modified pseudo-spectral operator in harmonic balance CFD solvers". *Int. Jou. Comput. Fluid Dynamics,* ***30***(7), pp. 495–515.

[82] Djeddi, R., and Ekici, K., 2016. "Modified Spectral Operators for Time-Collocation and Time-Spectral Solvers". In Proceedings of 54th AIAA Aerospace Sciences Meeting.

[83] Kuerner, M., Reichstein, G., Schrack, D., Rose, M., Staudacher, S., Gier, J., and Engel, K., 2012. "Low Pressure Turbine Secondary Vortices: Reynolds Lapse". *ASME J. Turbomach.,* ***134***(6), p. 061022.

[84] Kuerner, M., Rose, M., Staudacher, S., Gier, J., Fiala, A., and Patzer, B., 2012. "Surface thin film gauge measurements in a two-stage low pressure turbine at low Reynolds number". In Proceedings of ASME Turbo Expo 2012. GT2012-68906.

[85] Yang, H., Nürnberger, D., and Weber, A., 2002. “A Conservative Zonal Approach With Application to Unsteady Turbomachinery Flows”. In DGLR Jahrestagung. DGLR-2002-073.

[86] Ashcroft, G., Frey, C., Heitkamp, K., and Weckmüller, C., 2013. “Advanced Numerical Methods for the Prediction of Tonal Noise in Turbomachinery-Part I: Implicit Runge-Kutta Schemes”. *ASME J. Turbomach.,* ***136***(2), p. 021002.

[87] Clark, J., and Grover, E., 2006. “Assessing Convergence in Predictions of Periodic-Unsteady Flowfields”. In Proceedings of ASME Turbo Expo 2006. GT2006-90735.

[88] Bitter, M., Stotz, S., and Niehuis, R., 2020. “On High-Resolution Pressure Amplitude and Phase Measurements Comparing Fast-Respons Pressure Transducers and Unsteady Pressure-Sensitive Paint”. In Proceedings of ASME Turbo Expo 2020. GT2020-14744.

[89] Acton, P., and Fottner, L., 1996. “The generation of instationary flow conditions in the high-speed cascade wind tunnel”. In 13th Symp. on Meas. Techn. in Transsonic & Supersonic Flows in Casc. & Turbomach.

[90] Stieger, R., and Hodson, H., 2005. “The Unsteady Development of a Turbulent Wake Through a Downstream Low-Pressure Turbine Blade Passage”. *ASME J. Turbomach.,* ***127***(2), pp. 388–394.

[91] Bitter, M., and Niehuis, R., 2019. “Effects of Periodic Inflow Turbulence on the Statistics in the Wake of Linear LPT Cascade at Jet-Engine relevant Test Conditions”. In 13th Int. Symp. on Particle Imag. Velocimetry (ISPIV) 2019.

[92] Brunner, S., and Fottner, L., 1999. “Untersuchungen zum Einfluss der Rotor-Stator Interaktion auf die saugseitige Transition eines hochbelasteten ungekühlten Niederdruck-Turbinengitters”. In DGLR Annual Meeting. DGLRJT99-078.

[93] Kulite Semiconductor Product Inc., 2014. "Data Sheet LQ-062". In http://www.kulitesensors.com.cn/pdf_Data_Sheets/LQ.LE-062.pdf. visited 2020.03.29.

[94] Schlüß, D., and Frey, C., 2018. "Time Domain Flutter Simulations of a Steam Turbine Stage using Spectral 2D Non-Reflecting Boundary Conditions". In Proceedings of ISUAAAT15. ISUAAAT15-065.

[95] Hoyniak, D., and Clark, W., 1999. "Aerodynamic Damping Predictions Using a Linearized Navier-Stokes Analysis". In Proceedings of ASME Turbo Expo 1999. 99-GT-207.

[96] Clark, W., and Hall, K. C., 2000. "A Time-Linearized Analysis of Stall Flutter". *ASME J. Turbomach.,* ***122***(3), pp. 467–476.

[97] Ning, W., Li, Y., and Wells, R., 2003. "Predicting Bladerow Interactions Using a Multistage Time-Linearized Navier–Stokes Solver". *ASME J. Turbomach.,* ***125***(1), pp. 25–32.

[98] Petrie-Repar, P., 2006. "Development of an Efficient and Robust Linearised Navier–Stokes Flow Solver". Vol. 6 of *Graduate Studies in Mathematics*, Springer, ed. by Hall, K.C., Kielb, R.E. and Thomas, J.P., pp. 437–448.

[99] Thormann, R., and Widhalm, M., 2013. "Linear-Frequency-Domain Predictions of Dynamic-Response Data for Viscous Transonic Flows". *AIAA Journal,* ***51***(11), pp. 2540–2557.

[100] Kersken, H., Ashcroft, G., Frey, C., Wolfrum, N., and Pütz, O., 2018. "Comparison of Linear and Nonlinear Frequency Domain Methods for Flutter Analysis". In Proceedings of ASME Turbo Expo 2018. GT2018-75626.

[101] Weis, N., 2019. "Numerische Simulation instationärer, abgelöster Strömungen im Zeit- und Frequenzbereich". M.Sc. Thesis, German Aerospace Center DLR, Cologne, Germany.

[102] Erengil, M., 1993. “Physical causes of separation shock unsteadiness in shock wave/turbulent boundary layer interactions”. PhD Thesis, University of Texas at Austin, Austin, TX, USA.

[103] Sartor, F., Clement, M., Sipp, D., and Bur, R., 2013. “Dynamics of a shock-induced separation in a transonic flow: A linearized approach”. In Proceedings of 43rd AIAA Fluid Dynamics Conference and Exhibit.

[104] Agostini, L., Larchevêque, L., and Dupont, P., 2015. “Mechanism of shock unsteadiness in separated shock/boundary-layer interactions”. *Physics of Fluids,* ***27***(12), p. 126103.

[105] Dupont, P., Haddad, C., and Debiève, J. F., 2006. “Space and time organization in a shock-induced separated boundary layer”. *Journal of Fluid Mechanics,* ***559***, pp. 255–277.

[106] Shiratori, T., Matsushita, M., and Noguchi, Y., 1998. “Periodic Fluctuation of Shock Waves in Transonic Cascade Flows”. In Unsteady Aerodynamics and Aeroelasticity of Turbomachines, T. H. Fransson, ed., Springer Netherlands, pp. 693–704.

[107] Börner, M., and Niehuis, R., 2020. “Dynamics of Shock Waves Interacting with Laminar Separated Transsonic Turbine Flow Investigated by High-Speed Schlieren and Surface Hot-Film Sensors”. In Proceedings of ASME Turbo Expo 2020. GT2020-14386.

[108] Frazza, L., Hay, A., and Pelletier, D., 2015. “A logarithmic formulation for low-reynolds number turbulence models with adaptive wall-functions”. In Proceedings of 22nd AIAA Computational Fluid Dynamics Conference. AIAA 2015-2464.

[109] Da Già, R., Cerroni, D., Menghini, F., and Sandro, M., 2016. “Numerical validation of a four parameter logarithmic turbulence model”. In Proceedings of Seventh European Conference on Computational Fluid Dynamics (ECCOMAS CFD).

[110] Brandstetter, C., and Stapelfeldt, S., 2021. "Analysis of a linear model for non-synchronous vibrations near stall". *International Journal of Turbomachinery, Propulsion and Power,* ***6***(3).

Appendix A

Appendix

A.1. Governing Equations for Unsteady Aerodynamics

In the context of this research, the flow field is described completely by a set of partial differential equations known as the compressible Navier-Stokes equations. Since the main case of application are internal flows within turbomachinery, the problem is formulated in general in a rotating frame of reference. The compressible Navier-Stokes equations are defined in their differential formulation by

$$\frac{\partial \hat{\mathbf{Q}}}{\partial t} + \frac{\partial \hat{\mathbf{F}}}{\partial \xi} + \frac{\partial \hat{\mathbf{G}}}{\partial \eta} + \frac{\partial \hat{\mathbf{H}}}{\partial \zeta} = \left[\frac{\partial \hat{\mathbf{F}}_v}{\partial \xi} + \frac{\partial \hat{\mathbf{G}}_v}{\partial \eta} + \frac{\partial \hat{\mathbf{H}}_v}{\partial \zeta} \right] + \hat{\mathbf{S}} \quad . \tag{A.1}$$

Here, $\hat{\mathbf{Q}} = (1/J)[\rho, \rho u, \rho v, \rho w, \rho E]^T$ denotes the solution vector and $J = \partial(\xi, \eta, \zeta, t)/\partial(x, y, z, t)$ defines the Jacobian of the transform between the rotating frame of reference and its associated absolute system of inertia.

As it is common standard in turbomachinery aerodynamics, the rotational axis is chosen in accordance with the x-axis of the reference system of inertia. Therefore, the angular velocity is given by the rotational vector of $\mathbf{\Omega} = [\omega, 0, 0]^T$. Consequently, the resulting Coriolis and centrifugal forces linked to the formulation in the rotating frame of reference require the

consideration of an additional source term $\hat{\mathbf{S}}$ defined as

$$\hat{\mathbf{S}} = \frac{1}{J}\begin{bmatrix} 0 \\ 0 \\ \rho\omega(y\omega + 2w) \\ \rho\omega(z\omega - 2v) \\ 0 \end{bmatrix} . \tag{A.2}$$

The fluxes provided by either the viscid components $\hat{\mathbf{F}}_v$, $\hat{\mathbf{G}}_v$, $\hat{\mathbf{H}}_v$ or the inviscid components $\hat{\mathbf{F}}$, $\hat{\mathbf{G}}$, $\hat{\mathbf{H}}$ are given by

$$\hat{\mathbf{F}} = \frac{1}{J}\begin{bmatrix} \rho U \\ \rho U u + \xi_x p \\ \rho U v + \xi_y p \\ \rho U w + \xi_z p \\ (\rho E + p)U - \xi_t p \end{bmatrix} \quad , \quad \hat{\mathbf{F}}_v = \frac{1}{J}\begin{bmatrix} 0 \\ \xi_x \tau_{xx} + \xi_y \tau_{xy} + \xi_z \tau_{xz} \\ \xi_x \tau_{xy} + \xi_y \tau_{yy} + \xi_z \tau_{yz} \\ \xi_x \tau_{xz} + \xi_y \tau_{yz} + \xi_z \tau_{zz} \\ \xi_x b_x + \xi_y b_y + \xi_z b_z \end{bmatrix} \tag{A.3}$$

$$\hat{\mathbf{G}} = \frac{1}{J}\begin{bmatrix} \rho V \\ \rho V u + \eta_x p \\ \rho V v + \eta_y p \\ \rho V w + \eta_z p \\ (\rho E + p)V - \eta_t p \end{bmatrix} \quad , \quad \hat{\mathbf{G}}_v = \frac{1}{J}\begin{bmatrix} 0 \\ \eta_x \tau_{xx} + \eta_y \tau_{xy} + \eta_z \tau_{xz} \\ \eta_x \tau_{xy} + \eta_y \tau_{yy} + \eta_z \tau_{yz} \\ \eta_x \tau_{xz} + \eta_y \tau_{yz} + \eta_z \tau_{zz} \\ \eta_x b_x + \eta_y b_y + \eta_z b_z \end{bmatrix} \tag{A.4}$$

$$\hat{\mathbf{H}} = \frac{1}{J}\begin{bmatrix} \rho W \\ \rho W u + \zeta_x p \\ \rho W v + \zeta_y p \\ \rho W w + \zeta_z p \\ (\rho E + p) W - \zeta_t p \end{bmatrix} \quad , \quad \hat{\mathbf{H}}_v = \frac{1}{J}\begin{bmatrix} 0 \\ \zeta_x \tau_{xx} + \zeta_y \tau_{xy} + \zeta_z \tau_{xz} \\ \zeta_x \tau_{xy} + \zeta_y \tau_{yy} + \zeta_z \tau_{yz} \\ \zeta_x \tau_{xz} + \zeta_y \tau_{yz} + \zeta_z \tau_{zz} \\ \zeta_x b_x + \zeta_y b_y + \zeta_z b_z \end{bmatrix} \tag{A.5}$$

ρ denotes the fluid's density, u, v and w denote the fluid velocity in the absolute frame of reference and p and E denote the fluid's stati pressure and the total energy, respectively. The latter is determined by

$$E = \varepsilon + \frac{1}{2}\left(u^2 + v^2 + w^2\right) - \frac{1}{2}\omega_1^2 r^2 \tag{A.6}$$

where ε represents the specific internal energy density and the radial direction is expressed in terms of a cylindrical coordinate system by $r := \sqrt{y^2 + z^2}$. The fluid's static pressure is determined by the application of the ideal gas relation and therefore linked to the fluid temperature T and density ρ. Furthermore, the components U, V and W referred to in the inviscid fluxes represent the contravariant velocity components defined via

$$\begin{aligned} U &= \xi_x u + \xi_y v + \xi_z w + \xi_t \\ V &= \eta_x u + \eta_y v + \eta_z w + \eta_t \\ W &= \zeta_x u + \zeta_y v + \zeta_z w + \zeta_t \end{aligned} \tag{A.7}$$

As usually done in continuum mechanics, the tensor of the viscous stresses is abbreviated by τ_{ij} which are linked to the fluid velocity by

$$\tau_{ij} = \mu\left[\left(\frac{\partial u_j}{\partial x_i} + \frac{\partial u_i}{\partial x_j}\right) - \frac{2}{3}\frac{\partial u_k}{\partial x_k}\delta_{ij}\right] \quad . \tag{A.8}$$

The fluid's dynamic molecular viscosity μ is again related to the fluids temperature which is considered during the solution process by relying on Sutherland's Law.

Finally, the term flux terms are completed by the missing b_j given by

$$b_j = u_i \tau_{ij} + \frac{1}{(\gamma - 1)} \mu \frac{\partial T}{\partial x_j} \quad . \tag{A.9}$$

laws of Newton and thermodynamics - the flow state is described completely by the conservation of mass (A.10), momentum (A.11) and energy (A.12).

$$0 = \frac{\partial \rho}{\partial t} + \frac{\partial}{\partial x_i} (\rho u_i) \tag{A.10}$$

$$0 = \frac{\partial}{\partial t} (\rho u_i) + \frac{\partial}{\partial x_j} \left(\rho u_j u_i \right) + \frac{\partial p}{\partial x_i} - \frac{\partial \tau_{ij}}{\partial x_j} \tag{A.11}$$

$$0 = \frac{\partial}{\partial t} \left[\rho \left(\epsilon + \frac{u_i u_j}{2} \right) \right] + \frac{\partial}{\partial x_j} \left[u_j \rho \left(h + \frac{u_i u_j}{2} \right) \right] + \frac{\partial}{\partial x_j} \left[q_j - u_i \tau_{ij} \right] \tag{A.12}$$

If required, the missing heat flux vector q_j can be obtained, for instance, by exploiting Fourier's law or any other more sophisticated model of the underlying heat transfer.

A.2. Fourier Analysis

The following hints can prove to be helpful to the reader while recapitulating the statements made in section 2.4 in the context of Fourier analysis. First, a rather trivial though not necessarily always present relationship is exploited for the analysis of the alternative differential operator $\mathcal{D}_M$ in eq. (2.13).

$$
\begin{aligned}
e^{\mathrm{i}(M+1)(\Omega t+\frac{\pi}{M+1})} &= e^{\mathrm{i}(M+1)\Omega t+\mathrm{i}\pi} &= -e^{\mathrm{i}(M+1)\Omega t} \\
e^{\mathrm{i}(M+1)(\Omega t-\frac{\pi}{M+1})} &= e^{\mathrm{i}(M+1)\Omega t-\mathrm{i}\pi} &= -e^{\mathrm{i}(M+1)\Omega t}
\end{aligned}
\tag{A.13}
$$

Furthermore, the definition of the sinus cardinalis, denoted frequently by its abbreviation sinc(·), is introduced in eq. (2.14)

$$
\mathrm{sinc}(\omega) \;:=\; \frac{\sin(\pi\omega)}{\pi\omega} \quad . \tag{A.14}
$$

The sinc(·)-function is one of the important fundamental functions in the field of signal analysis in general since it provides the fourier transform of the rect(·)-function which yields in particular

$$
\mathrm{rect}(kt) \circ\!\!-\!\!\bullet\, \mathrm{sinc}(k\omega) \quad . \tag{A.15}
$$

Recalling the convolution theorem [78] stating the equivalence of multiplication in the frequency domain and convolution in the time domain and vice versa, respectively, the multiplication of a quantity in its frequency domain formulation with the sinc(·)-based Lanczos-σ_m factors as proposed by eq. (2.14) is equivalent to a convolution of a rect(·)-based window function of the underlying time domain signal. In addition to that, the following properties are worth noticing for a deeper understanding of the proposed Lanczos-filter application:

1. $\sigma_0 = \frac{\sin(\pi\frac{0}{M+1})}{\pi\frac{0}{M+1})} = 1$
2. $\sigma_{M+1} = \frac{\sin(\pi)}{\pi} = 0$
3. $\underline{k < m:} \quad 0 < \sigma_k < 1$

The first aspect underlines the invariance of the temporal average - the zero

harmonic or DC component, that is - if the proposed Lanczos-filter method is applied. The second aspect highlights the low-pass properties of the filter since any component beyond the truncation order vanishes due to a multiplication by the zero element. The latter aspect closes with the statement, that the Lanczos-σ_m factors corresponding to a non-truncated harmonic are in the range between 0 and 1 which is equivalent to an increasing impact of the filter method on high-frequent content.

A.3. Statistic Moments of a Data Set

In the theory of statistics and probability, a central moment provides information about the probability distribution of a real-valued, arbitrary quantity ϕ about its mean value or the expected value, that is. The n-th central moment of the quantity ϕ is defined as

$$\mu_n \;=\; \mathbf{E}\Big[\big(\phi - \mathbf{E}[\phi]\big)^n\Big] = \int_{-\infty}^{\infty} \big(\phi - \mu\big)^n \cdot f(\phi)\,\mathbf{d}\phi \tag{A.16}$$

with μ denoting the quantity's mean value and $f(\phi)$ the underlying probability density function.

The second central moment μ_2 is called the variance of a data set and often denoted σ^2 with σ representing the standard deviation. The variance μ_2 is equivalent to the expected squared deviation of the quantity ϕ about its mean value μ. Accordingly, it provides an indicator of how far a quantity spreads about its mean value. Following eq. (A.16), it is defined via

$$\mu_2 \;=\; \sigma^2 = \int_{-\infty}^{\infty} \big(\phi - \mu\big)^2 \cdot f(\phi)\,\mathbf{d}\phi \quad . \tag{A.17}$$

If, for instance, the statistic deviation about the mean μ is described by a

Gaussian Normal Distribution, decreasing the variance σ^2 leads obviously to a progressively constricted shape of the bump due to the decreasing spreading of the values about its mean.

However, considering a data set being not normally distributed about the underlying mean μ, the question arises of how to provide information which side of the mean is outnumbered. This information is given by the third central moment μ_3, usually called the skewness of a data set and defined as

$$\mu_3 = \int_{-\infty}^{\infty} \left(\phi - \mu\right)^3 \cdot f(\phi)\, \mathbf{d}\phi \quad . \tag{A.18}$$

In contrast to the second central moment, the integrand $(\phi - \mu)^3$ can be either positive or negative depending on ϕ being higher or smaller of the associated mean value ϕ. Therefore, it is easy to see that negative values of the skewness as defined via eq. (A.18) indicate a higher number of elements within the evaluated data set to be smaller than the mean value μ whereas positive values of μ_3 hint at the opposite. If, and only if, the negative contributions balance the positive, the skewness is zero which is always the case for a symmetric or even normally distributed deviation of the considered elements about their mean value μ.

A.4. Imperfect Sampling of Harmonic Content

Starting from eq. (2.4), the unsteady flow problem can be formulated exactly in the frequency domain under the assumption, that both the frequency Ω^* and the solution state $\widehat{q}^*$ are the exact solution of the problem

$$\mathrm{i}\Omega^* \widehat{q}^* + \widehat{R}(\widehat{q}^*) = 0 \quad . \tag{A.19}$$

Inserting an imperfect frequency Ω in eq. (A.19) whose deviation from the exact frequency Ω^* is small enough that $\widehat{q}^*$ still maintains to provide the

exact solution of the problem yields

$$\mathrm{i}\Omega\,\widehat{q}^{*} + \widehat{R}(\widehat{q}^{*}) = \mathrm{i}\Omega\,\widehat{q}^{*} - \mathrm{i}\Omega^{*}\,\widehat{q}^{*} = \mathrm{i}\left(\Omega-\Omega^{*}\right)\widehat{q}^{*} \approx 0 \quad . \tag{A.20}$$

Obviously, the consideration of a slightly differing frequency Ω does not allow to solve the unsteady flow problem exactly anymore as the error can be determined via eq. (A.20). Solution of eq. (A.20) by relying on the principle of a pseudo time-stepping algorithm - as it is done during the solution process of the investigated Harmonic Balance method - leads accordingly the following ODE

$$\frac{\partial\widehat{q}^{*}}{\partial\tau} + \mathrm{i}\left(\Omega-\Omega^{*}\right)\widehat{q}^{*} \;\rightarrow\; 0 \quad . \tag{A.21}$$

The analytical solution of the ODE described by eq. (A.21) is obviously given by

$$\widehat{q}^{*}(\tau) \;=\; \widehat{q}^{*}|_{\tau=0}\cdot e^{-\mathrm{i}\,(\Omega-\Omega^{*})\,\tau} \quad . \tag{A.22}$$

The initial value $\widehat{q}^{*}|_{\tau=0}$ of eq. (A.22) is equivalent to the converged state of the unsteady flow problem since only for the converged state the pseudo time-step is driven to zero and finally vanishes. Hence, solving for a beat frequency Ω even slightly differing from the exact frequency Ω^{*} associated to the exact solution of the flow state ends in an oscillation around the converged state $\widehat{q}^{*}|_{\tau=0}$ with a constant phase shift of $(\Omega-\Omega^{*})$. If, and only if, the solved beat frequency coincides with the solution frequency of the problem exactly, the pseudo time-stepping algorithm will drive the solution to a non-oscillating convergent state.

However, since in general the deviations of the relied base frequencies are of small order, the above stressed oscillation will not exceed the global noise level and therefore not affect the global convergence behaviour in a noticeable fashion. If the described behaviour of an oscillating convergence

history can be observed during the Harmonic Balance solution process, this can be considered as a clear indicator of either solving for an erroneous base frequency or an unfavourable interference with additional frequency content appearing at a frequency close to the beat frequency of interest.

In practice, this can be observed in the presence of unexpected non-synchronous frequency content induced by vortex shedding, SWBLI or the presence of an open separation bubble affecting the mass flow through the narrowest section of the passage.